POLARIZATION-SENSITIVE MUELLER-MATRIX OPTICAL COHERENCE TOMOGRAPHY

A Dissertation

by

SHULIANG JIAO

Submitted to the Office of Graduate Studies of
Texas A&M University
in partial fulfillment of the requirements for the degree of

DOCTOR OF PHILOSOPHY

December 2003

Major Subject: Biomedical Engineering

POLARIZATION-SENSITIVE MUELLER-MATRIX OPTICAL COHERENCE TOMOGRAPHY

A Dissertation

by

SHULIANG JIAO

Submitted to Texas A&M University
in partial fulfillment of the requirements
for the degree of

DOCTOR OF PHILOSOPHY

Approved as to style and content by:

Lihong V. Wang
(Chair of Committee)

Gerard L. Coté
(Member)

Jay D. Humphrey
(Member)

Henry F. Taylor
(Member)

William Hyman
(Head of Department)

December 2003

Major Subject: Biomedical Engineering

ABSTRACT

Polarization-sensitive Mueller-Matrix Optical Coherence Tomography. (December 2003)

Shuliang Jiao, Ph. D, Huazhong University of Science and Technology, China

Chair of Advisory Committee: Dr. Lihong V. Wang

Measuring the Mueller matrix with optical coherence tomography (OCT) makes it possible to acquire the complete polarization properties of scattering media with three-dimensional spatial resolution. We first proved that the measured degree-of-polarization (DOP) of the backscattered light by OCT remains unity—a conclusion that validated the use of Jones calculus in OCT. A multi-channel Mueller-matrix OCT system was then built to measure the Jones-matrix, which can be transformed into a Mueller matrix, images of scattering biological tissues accurately with single depth scan. We showed that when diattenuation is negligible, the round-trip Jones matrix represents a linear retarder, which is the foundation of conventional PS-OCT, and can be calculated with a single incident polarization state although the one-way Jones matrix generally represents an elliptical retarder; otherwise, two incident polarization states are needed. We discovered the transpose symmetry in the roundtrip Jones matrix, which is critical for eliminating the arbitrary phase difference between the two measured Jones vectors corresponding to the two incident polarization states to yield the correct Jones matrix.

We investigated the various contrast mechanisms provided by Mueller-matrix OCT. Our OCT system for the first time offers simultaneously comprehensive polarization contrast mechanisms including the amplitude of birefringence, the orientation of birefringence, and the diattenuation in addition to the polarization-independent intensity contrast, all of which can be extracted from the measured Jones or the equivalent Mueller matrix. The experimental results obtained from rat skin samples, show that Mueller OCT provides complementary structural and functional information on biological samples and reveal that polarization contrast is more sensitive to thermal degeneration of biological tissues than amplitude-based contrast.

Finally, an optical-fiber-based multi-channel Mueller-matrix OCT was built and a new rigorous algorithm was developed to retrieve the calibrated polarization properties of a sample. For the first time to our knowledge, fiber-based polarization-sensitive OCT was dynamically calibrated to eliminate the polarization distortion caused by the single-mode optical fiber in the sample arm, thereby overcoming a key technical impediment to the application of optical fibers in this technology.

DEDICATION

This dissertation is dedicated to my parents, my wife, and my daughter. Without their support I could have never finished this dissertation.

ACKNOWLEDGMENTS

I would like to express my appreciation to Dr. Lihong V. Wang for his help and guidance throughout all these years of research and life as a graduate student.

I would like to express my gratitude also to my advisory committee: Dr. Jay D. Humphrey, Dr. Gerard L. Coté, and Dr. Henry F. Taylor.

Thanks to Geng Ku, Gang Yao, Wurong Yu, Hao Zhang, Milos Todorovic, Sava Sakadzic, Minghua Xu, and Yuan Xu, all members of Dr. Wang's Optical Imaging Laboratory, for their help.

This project was sponsored in part by National Institutes of Health grants R21 EB00319-02 and R01 EB000712, by National Science Foundation grant BES-9734491, and by Texas Higher Education Coordinating Board grant 000512-0063-2001.

TABLE OF CONTENTS

Page

ABSTRACT iii

DEDICATION v

ACKNOWLEDGMENTS vi

TABLE OF CONTENTS vii

LIST OF FIGURES ix

LIST OF TABLES xii

1 INTRODUCTION 1

- 1.1 Overview 1
- 1.2 Conventional Optical Coherence Tomography 3
- 1.3 Polarization-sensitive Optical Coherence Tomography 5

2 POLARIZATION IN BIOLOGICAL TISSUES 9

- 2.1 Birefringence in Collagen 9
- 2.2 Types of Birefringence 11
- 2.3 Polarization in Biological Tissues 12
- 2.4 Factors Affecting Birefringence in Collagen 13

3 MUELLER MATRIX AND JONES MATRIX 15

- 3.1 Stokes Vector and Mueller Matrix 15
- 3.2 Jones Vector and Jones Matrix 19
- 3.3 Jones and Mueller Matrices of Standard Elements 21

4 SINGLE-CHANNEL MUELLER-MATRIX OCT 23

- 4.1 Experimental System 23

Page

4.2 Measuring the Stokes Vectors and Mueller Matrix of Biological Samples.....25
4.3 Measuring the Degree of Polarization.....32

5 MULTI-CHANNEL MUELLER-MATRIX OCT.....39

5.1 Introduction.....39
5.2 Experimental System.....40
5.3 Acquisition of the Jones Matrix.....43
5.4 Experimental Results and Analysis.....59
5.5 Conclusion.....66

6 CONTRAST MECHANISMS IN MUELLER-MATRIX OCT.....67

6.1 Introduction.....67
6.2 Polarization-based Contrast.....68
6.3 Calculation of the Roundtrip Jones Matrix.....70
6.4 Experiment.....73
6.5 Discussion.....78
6.6 Conclusion.....98

7 FIBER-BASED MULTI-CHANNEL MUELLER-MATRIX OCT.....83

7.1 Introduction.....83
7.2 Calibration Algorithm.....84
7.3 Comparison of the Algorithm with Conventional PS-OCT.....90
7.4 Experimental System.....93
7.5 Experimental Results and Discussion.....95
7.6 Conclusion.....98

8 CONCLUSION.....99

REFERENCES.....101

VITA.....115

LIST OF FIGURES

Page

Fig. 1.1 Illustration of the principle of optical coherence tomography…..........................3

Fig. 1.2 Schematic of the conventional PS-OCT system. LP: linear polarizer, NBS: non-polarizing beam splitter, QW1: $\lambda/4$ plate oriented at 22.5º, QW2: $\lambda/4$ plate oriented at 45º, PBS: polarizing beam splitter...7

Fig. 2.1. Structure of collagen fiber 10

Fig. 4.1 Schematic of the single-channel Mueller-matrix OCT system: SLD, superluminescent diode; LP: linear polarizer; HW: zero-order half-wave plate; QW: zero-order quarter-wave plate; NBS: non-polarization beam splitter; VW: variable-wave plate; M: mirror; PD: photodiode. 24

Fig. 4.2 (a) Raw 2D OCT images. (b) Stokes images...27

Fig. 4.3 (a) Raw OCT images. (b) Normalized Mueller-matrix images. 29

Fig. 4.4 The raw 2-D images and the 2-D images of the corresponding Mueller matrix of a piece of fish bone...31

Fig. 4.5 (a) S_{H0} and DOP for 5% *Intralipid* solution. (b) DOLP and DOCP for 5% *Intralipid* solution. (c) DOP for 1%, 2% and 5% *Intralipid* solution......................33

Fig. 4.6 (a) S_{H0} and DOP for a bone tissue from the head of a yellow croaker fish. (b) DOLP, and DOCP for the same region of the sample......................................34

Fig 5.1 Schematic of the multi-channel Mueller OCT system…....................................42

Fig 5.2 (a) Normalized amplitude of the vertical components of the measured Jones vectors of a quarter-wave plate versus the orientation of the fast axis. (b) Phase differences between the vertical and the horizontal components of the Jones vectors of the same quarter-wave plate.. 55

Fig 5.3 Measured vertical component of the OCT signal of the calibrating variable wave plate for the light source with a vertical polarization state. The inset is the plot of 300 data points of the interference signal around the peak....................57

Fig 5.4 2D Mueller-matrix images of a piece of porcine tendon. Each image except M_{00} is pixel-wise normalized with the M_{00} element and shares the same color table.. 60

Fig 5.5 (a) M_{00} and 2D Jones-matrix images of a piece of normal porcine tendon. (b) M_{00} and 2D Jones-matrix images of the piece of porcine tendon heated for 20 seconds at 90°. 61

Fig 5.6 The averaged raw data of M_{31} (“*”) and M_{32} (“o”), as in Eq. (12), of a piece of porcine tendon versus penetration depth and the fitted curve (“—”) for different orientations. From the top to the bottom the interval of variation of the orientation is –10°..64

Fig 5.7 The calculated angle and the standard error of the fast axis for different orientations of the sample in Fig 5.5. 65

Fig. 6.1 (a) Conventional OCT image (in logarithmic scale), (b) intensity image (M_{00}, in logarithmic scale), (c) retardation image, (d) differential retardation image, (e) image of the orientation of the fast axis, and (f) polarization histologic image of an *in situ* rat tail. The height of each image is 750 μm. The gray scales are for the orientation (θ_2) and retardation (φ_2) images, respectively. The conventional OCT image was obtained with vertical linear polarization states for both the incident and reference beams. *F*: fat; *K*: keratin; *DP*: dermal papilla. 74

Fig. 6.2 (a) Intensity image (M_{00}, in logarithmic scale), (b) retardation image, (c) diattenuation image, and (d) polarization histologic image of a piece of *ex vivo* rat skin with a burn lesion. The height of each image is 750 μm. The gray scales are for the retardation (φ_2) and diattenuation (D_2) images, respectively. *B*: burn region...76

Fig. 6.3 Average of 10 depth profiles of the retardation around the center of the burn area and the normal region to the right of the burn area.................................77

Fig. 6.4 Averaged depth profiles of the intensity (in logarithmic scale) and retardation over the region marked with a horizontal white bar in Fig. 6.1(b). Labels (1), (2), and (3): layers revealed 81

Fig. 7.1 Illustration of the polarization transformation in the sample arm. $\mathbf{E}_{i1}$ and $\mathbf{E}_{i2}$: incident Jones vectors for the sampling fiber and the sample; $\mathbf{E}_{o1}$: the measured output roundtrip Jones vector from the sample surface; $\mathbf{E}_{o2}$: the roundtrip Jones vector representing the transformation result of both the fiber and the tissue layer; $\mathbf{J}_{f1}$ and $\mathbf{J}_{s1}$: the one-way Jones matrix of the sampling fiber and the sample………………………………………………………….. 85

Fig. 7.2 The calibration results for a simulated sample with $\varphi_{s2} = 36^\circ$ and sampling-fiber parameters: (a) $\varphi_{f1} = 46^\circ; 0 \le \theta_{f1} < \pi;\ 0 \le \delta_{f1} < \pi$ and (b) $\delta_{f1} = 50^\circ; 0 \le \theta_{f1} < \pi;\ 0 \le \varphi_{f1} < \pi$ 89

Fig. 7.3 The calculated orientation of the fast axis with the two different algorithms for a fiber-based PS-OCT system..92

Fig. 7.4 Schematic of the fiber-based Mueller OCT system. SLDH and SLDV: superluminescent diodes, horizontally polarized (*H*) and vertically polarized (*V*), respectively; PBS1 and PBS2: polarizing beam splitters; SF: spatial filter assembly; NBS: non-polarizing beam splitter; M: mirror; SMF: single-mode optical fiber; PDH and PDV: photodiodes for the *H* and *V* polarization components, respectively. 94

Fig. 7.5 Phase retardation of a λ/4 plate calculated from the measured Jones matrix before and after cancellation of the polarization distortion caused by the sampling optical fiber. The phase retardation of the sampling fiber is shown as well, which is zero after cancellation by definition. 95

Fig. 7.6 The M_{00} image of the Mueller matrix, the retardation images before and after cancellation of the polarization effect of the sampling fiber φ_{sf2} and φ_{s2} of the skin of a rat tail measured with the fiber-based Mueller OCT system. An *HE* stained histological image is also shown for comparison. The M_{00} image is on a logarithmic scale while the retardation images are on a linear scale. The height of each image is 1 mm. *EP*: epidermis; *DP*: dermal papilla; and *DJ*: dermal-epidermal junction...97

Fig. 7.7 The M_{00} image of the Mueller matrix, the calculated retardation image φ_{s2}, and the image of the orientation of the fast axis of the skin of a rat tail measured *in vivo* with the fiber-based Mueller OCT system. The M_{00} image is in logarithmic scale while the retardation image is in linear scale. The height of the images is 1mm. *EP*: Epidermis; *DP*: dermal papilla; *HS*: hair shaft. 98

LIST OF TABLES

Page

Table 2.1 Four major types of collagen and their properties 11

1 INTRODUCTION

1.1 Overview

Optical coherence tomography[1] is a non-invasive, non-contact imaging technique that can provide high-resolution (micron scale) cross-sectional images of biological tissues. OCT is the two dimensional extension of optical coherence domain reflectometry, an interferometric ranging technique originally developed for finding faults in fiber optic cables and network components.[2, 3] Since it was first developed at M.I.T in 1991, OCT has become a major area of research in the field of biomedical optics with applications in ophthalmology,[4] cardiology,[5] neurology,[6] gynecology, dermatology,[7] dentistry,[8] developmental biology,[9] urology,[10] and gastroenterology.[11]

Analogous to B-mode ultrasound imaging, where the depth information of a structure is revealed by the time-of-flight of a sound echo, OCT detects the back-reflected probe light where the depth information of a structure is revealed by coherence gating. OCT detects the interference signal between the reflected sample beam and reference beam in an interferometer (usually Michelson interferometer) illuminated by a broadband light source, where interference occurs only when the optical path-length difference between the sample beam and reference beam is within the coherence length of the light source. The depth of a structure can be determined by the position of the reference mirror when interference occurs with a resolution determined by the coherence length, which is inversely proportional to the bandwidth of the broadband light source.

This dissertation follows the style of *Applied Optics*.

In addition to the rapid development of research on clinical applications of OCT and on the various fiber-based imaging probes,[12–14] active new branches of the technology have being added based on different contrast mechanisms. Optical Doppler tomography (ODT) for measuring the blood flow was developed first in 1997.[15,16] Polarization-sensitive OCT (PS-OCT)[17–22] for measuring the polarization properties of biological samples was first demonstrated in 1992 [23] and has being rapidly developed since 1997. As a branch of PS-OCT and aiming at acquiring a complete characterization of the polarization properties of biological tissues, Mueller-matrix OCT was first developed in our laboratory in 1999. Spectroscopic OCT adds spectroscopic information on the conventional OCT image.[24]

In the meantime, tremendous focuses have been placed on increasing the depth resolution and imaging frame rate. By exploiting the broadband light sources of combined femtosecond laser and photonic crystal fiber, OCT has achieved axial resolution as high as submicrometer.[25] The development of rapid scanning optical delay line, has enabled OCT to acquire images at video rate.[26,27]

The idea of coherence gating has also generated several variations from the conventional OCT configuration, including full-field OCT, which combines a microscope with coherence gating to acquire en face microscopic images of a sample with depth resolution.[28] Spectral interferometric OCT (or Fourier-domain OCT) achieves depth scan by using frequency-domain technique, which eliminates the use of mechanical delay line.[29,30]

1.2 Conventional Optical Coherence Tomography

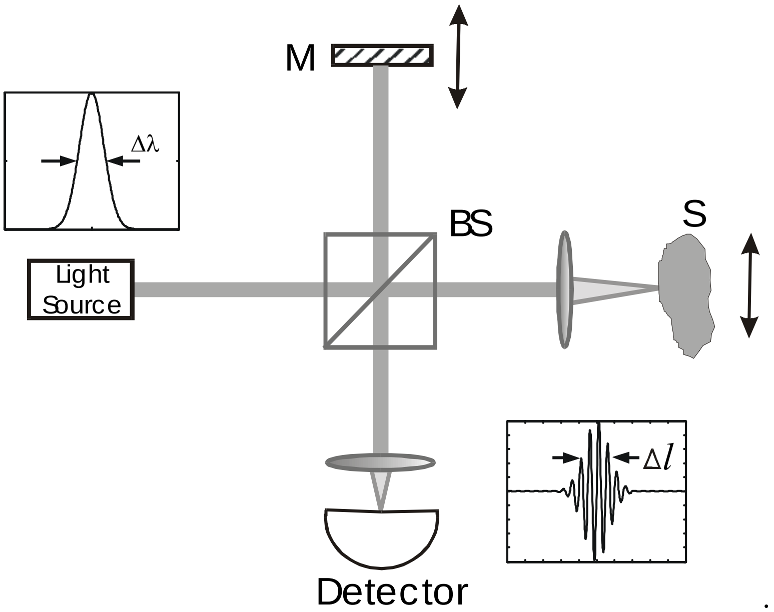

Fig. 1.1 Illustration of the principle of optical coherence tomography. M: mirror; BS: beam splitter; S: sample; $\Delta\lambda$: the FWHM bandwidth of the source; Δl: resolution of the OCT system.

We regard the OCT system that is dedicated to imaging only the back-reflected intensity of the sample light as conventional OCT. Shown in Fig. 1.1 is an illustration of the basic configuration of conventional OCT. A broadband light source, either a superluminescent diode (SLD) or a femtosecond laser is used in the interferometer, whose power spectrum can be expressed approximately in a Gaussian form:[31]

$$P(k') = \frac{P_0}{2\Delta k\sqrt{\pi}} \exp[-(\frac{k'}{\Delta k})^2], \qquad 1.1$$

where P_0 is the total source power, $k' = k - \bar{k}$, k is the free space wavenumber, $\bar{k}$ is the center free space wavenumber, and Δk is the wavenumber bandwidth. The incoming source beam is split into the reference arm and sample arm by a beam splitter. After reflected back by the reference mirror and the sample, the reference and sample beams are recombined by the beam splitter. The detected intensity $[I(k)]$ for each spectroscopic component of the light source can be expressed as:

$$\begin{aligned} I(k) &= [E_s(k)+E_r(k)][E_s(k)+E_r(k)]^* \\ &= E_s(k)E_s^*(k)+E_r(k)E_r^*(k)+E_s(k)E_r^*(k)+E_r(k)E_s^*(k) \\ &= I_s(k)+I_r(k)+2\left|E_s(k)E_r^*(k)\right|\cos[k(l_r-l_s)] \\ &= \frac{1}{2}I_0(k)(R_s+R_r)+\frac{1}{2}I_0(k)\sqrt{R_sR_r}\cos[k(l_r-l_s)] \end{aligned} \quad , \qquad 1.2$$

where $E_s(k)$ and $I_s(k)$ are the magnitude and intensity of the electric field at the detector reflected from the sample arm; $E_r(k)$ and $I_r(k)$ are the magnitude and intensity of the electric field at the detector reflected from the reference arm; R_s and R_r are the intensity reflectivity of the sample and reference arms, respectively; l_s and l_r are the path length of the sample and reference arms, respectively. The detected phase-dependent term of the interference signal can be expressed as:

$$\begin{aligned} S(\Delta l_0,\Delta l_g) &= \frac{\sqrt{R_sR_r}P_0}{4\Delta k\sqrt{\pi}}\int_{-\infty}^{\infty}\exp[-(\frac{k'}{\Delta k})^2]\cos(2\Delta l_0\bar{k}+2\Delta l_g k')dk' \\ &= \frac{1}{2}\sqrt{R_sR_r}P_0\exp[-(\frac{2\Delta l_g}{l_c})^2]\cos(2\bar{k}\Delta l_0) \end{aligned} \quad , \qquad 1.3$$

where $l_c = 2/\Delta k$ is the coherence length of the light source; $\bar{k}\Delta l_0$ is the phase delay mismatch at the center wavenumber; Δl_g is the group delay mismatch. The group delay is defined as $l_g = \left.\frac{d\phi}{dk}\right|_{\bar{k}}$, where ϕ is the phase of light.

OCT is designed to measure Δl_g. In the case when there is no mismatch of the group velocity dispersion between the reference arm and the sample arm, the free space depth resolution (Δl_{FWHM}) of an OCT system can be derived as:

$$\Delta l_{FWHM} = \frac{2\ln 2}{\pi}\frac{\bar{\lambda}^2}{\Delta\lambda_{FWHP}}, \qquad 1.4$$

where Δl_{FWHM} is the full width half magnitude of the interference profile when the sample is a mirror; $\bar{\lambda}$ and $\Delta\lambda_{FWHP}$ are the central wavelength and the full width half power bandwidth of the light source, respectively. The imaging depth of OCT is limited to the quasi-ballistic regime (1–2 mm) in scattering biological tissues. As in confocal microscopy, the lateral resolution is determined by the diameter of the focused probe beam in the sample. By using Gaussian optics, the lateral resolution (Δx) can be derived as:

$$\Delta x = \frac{4\bar{\lambda}}{\pi}\frac{f}{D}, \qquad 1.5$$

where f is focal length of the lens and D is the diameter of the sample beam incident on the lens.

1.3 Polarization-sensitive Optical Coherence Tomography

Polarization-sensitive OCT (PS-OCT) is designed to image the polarization properties of biological tissues. Upon interaction with the sample, the polarization state of the incident sample light is transformed into the polarization state of the backscattered sample light. The basic idea of PS-OCT is to measure the polarization variation induced by the sample in order to determine the polarization properties of the sample. The polarization state of the incident sample light and the polarization state of the reference light are known parameters and can be set with standard optical polarization elements such as polarizer and retarder. The polarization state of the backscattered sample light can be determined from the measured interference signals in the two detection channels as shown in Fig. 1.2. The two detection channels detect the horizontal and vertical components of the interference signals between the reference and backscattered sample light, respectively.

In conventional PS-OCT, a sample is treated as a pure retarder, a polarization element with only birefringence. By assuming a fixed orientation of the fast axis of the assumed retarder, the following formula was derived to calculate the amplitude of the accumulated retardation:

$$\varphi = \arctan\sqrt{I_H(z)/I_V(z)}\,, \qquad 1.6$$

where, φ is the amplitude of phase retardation, I_H and I_V are the measured intensities of the signals in the horizontal and vertical channels, respectively, z is the depth of the sample.

This is a simplified model and can give meaningful information only when the other polarization properties of the sample can be neglected and the orientation of the fast axis of the sample is constant. The derivation of Eq. 1.6 is based on the Jones calculus although there had been no theoretical and experimental verification of the suitability of Jones calculus for OCT.

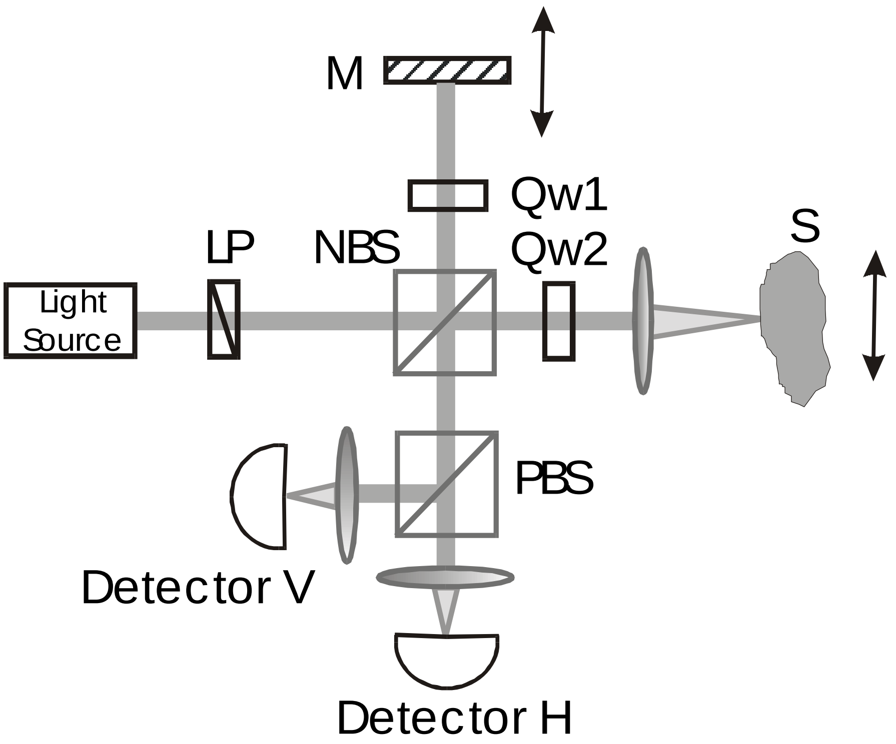

Fig. 1.2 Schematic of the conventional PS-OCT system; LP: linear polarizer, NBS: non-polarizing beam splitter, QW1: $\lambda/4$ plate oriented at 22.5º, QW2: $\lambda/4$ plate oriented at 45º, PBS: polarizing beam splitter.

We define Mueller-matrix OCT as PS-OCT that can measure the Mueller or Jones matrix of a sample. Although Mueller-matrix OCT is a branch of PS-OCT, it does not treat the polarization properties of a sample with the simplified model. The objective of Mueller-matrix OCT is to acquire a complete characterization of the polarization properties of a sample. To achieve this goal, the Jones or Mueller matrix of the sample was calculated from the detected interference signals together with the known polarization parameters of the incident sample light. The Jones or Mueller matrix is then used to calculate the various polarization parameters of the sample. From this point of view, Mueller-matrix OCT is the most general form of PS-OCT.

2 POLARIZATION IN BIOLOGICAL TISSUES

2.1 Birefringence in Collagen

Optical polarization exists in many types of biological tissues and is found to be an important parameter for the characterization of biological tissues.[32–36] Collagen is a predominant structural component in most biological tissues and is known to be birefringent. The collagens are a family of highly characteristic fibrous proteins found in all multi-cellular animals. They are secreted mainly by connective tissue cells and are the most abundant proteins in mammals, constituting 25% of their total protein. The characteristic feature of collagen molecules is their stiff, triple-stranded helical structure. Three collagen polypeptide chains, called α chains, are wound around one another in a regular superhelix to generate a ropelike collagen molecule about 300 nm long and 1.5 nm in diameter.[37]

Although in principle more than 1000 types of triple-stranded collagen molecules could be assembled from various combinations of the 20 or so α chains, only about 10 types of collagen molecules have been found. The best defined are types I, II, III, and IV. Types I, II, and III are the fibrillar collagens. They are the main types of collagen found in connective tissues, type I being by far the most common. After being secreted into the extracellular space, these three types of collagen molecules assemble into ordered polymers called collagen fibrils, which are thin (10–300 nm in diameter) cablelike structures, many micrometers long and clearly visible in electron micrographs.

The collagen fibrils often aggregate into larger bundles, which can be seen in the light microscope as collagen fibers several micrometers in diameter (Fig. 2.1).

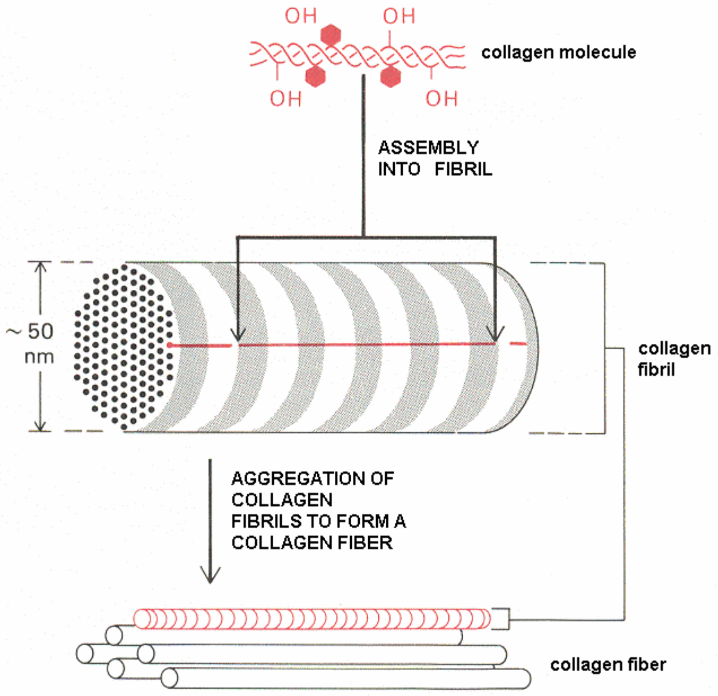

Fig. 2.1. Structure of collagen fiber.

As shown in Table 2.1, collagen I is strongly positively birefringent with respect to length of the fibers—light with electric vector parallel to the fiber length travels more slowly than light with electric vector in a plane perpendicular to the fiber. On the other hand, collagen III is weakly negatively birefringent due to large side chains and the presence of different and greater amounts of interstitial proteoglycans and other molecules.[38]

Table 2.1 Four major types of collagen and their properties

Type	Polymerized Form	Intrinsic birefringence	Tissue distribution
I	Fibril	Positive, intense	Skin, tendon, bone, ligaments, cornea, internal organs (accounts for 90% of body collagen)
II	Fibril		Cartilage, intervertebral disc, notochord, vitreous body of eye
III	Fibril	Negative, weak	Skin, blood vessels, internal organs
IV	Basal lamina		Basal laminae

2.2 Types of Birefringence

There are two types of birefringence: intrinsic and form birefringence.[39] Intrinsic birefringence is related to the spatial arrangement of atomic groups and molecules. For example, the positive birefringence in type I collagen results from the quasi-crystalline alignment parallel to the fiber and molecule axis of the amino acid residues of the polypeptide chains. The intensity of intrinsic birefringence is mainly a function of the alignment or order of the molecular packing, but also of the nature of the chemical groups encountered.[38] Form birefringence occurs in rod-like or plate-like bodies immersed in a medium having a different refractive index. The observed birefringence is the overall effect of these two types of birefringence.

2.3 Polarization in Biological Tissues

The orientation of collagen fibers in a tendon specimen or other collagen-containing tissue can be determined using polarimetry.[33–41] The optical properties of articular cartilage are related to the degree of order in the spatial arrangement of its collagen fibers.[42] Pathogenetic factors can be studied by mapping the pathways of fibers and blood vessels in the region of the rotator cuff with polarization microscopy.[43] Histochemical evaluation of the collagen content and its state of aggregation in fibrotic lesions can be provided with polarized light.[44–46] Polarization has been used to study mechanisms involved in coronary artery spasm[47] and in progressive systemic sclerosis.[48] The layered structure in aneurysms can also be analyzed by collagen birefringence.[49, 50]

Skin structures contain birefringent materials that can be detected by polarization microscopy. The epidermis of humans and many animal species contains a number of birefringent structures, the most conspicuous of which are the tonofilaments, keratin and hair. The subcutaneous, dermal tissue is rich in collagen type I and III as well as vascular channels and adnexal structures with sebaceous cells containing cholesterol, all of which are amenable to polarization imaging.[51]

Muscle fibers manifest birefringence as well. Skeletal muscle has been studied using polarization microscopy due to its birefringence.[52–55] Cardiac muscle disarray in hypertrophic cardiomyopathy can be quantified.[56] Patterns of myocardial fibrosis in idiopathic cardiomyopathies and chronic Chagasic cardiopathy can also be measured using polarization microscopy.[57] Polarization states of diffracted light from muscle fibers change with fiber activation.[58]

Polarization microscopy is a powerful tool for the investigation of cell membranes, microtubules, and filamentous actins.[59–63] It is able to reveal the organizational features of biological structures and the regularity of macromolecule building cells and tissues—properties that cannot be directly studied by other approaches in complex biological systems. Cell size can be measured from a polarized light scattering function.[64] Polymerized sickle cell hemoglobin (hemoglobin S) in erythrocytes can be visualized with a microscope that produces an image proportional to linear dichroism.[65, 66] Scanning laser polarimetry can be used to measure the retinal nerve fiber layer,[67–69] which contributes to the diagnosis of retinal diseases such as demyelinating optic neuritis and glaucoma.

2.4 Factors Affecting Birefringence in Collagen

M. Wolman analyzed the effects of stretching, wetting, aging, and thermal treatment on the birefringence in collagen.[38] The intensity of birefringence of collagen depends on a number of factors which are of considerable importance in diagnostic pathology. Young collagen, the fibrils of which are more hydrated and less perfectly aligned than those of mature collagen, is also less or not at all anisotropic. Cross-links between fibrils determine the intensity of birefringence.[39] Polarization reveals that the morphology and cross-link composition of collagen fibrils in tendons vary with age.[70] Stretching of tendons and other collagenous structures increases the intensity of their positive birefringence, which indicates that in stretched collagen the molecules are aligned more parallel to the fibril axis than without stretching.

After thermal contraction (obtained by immersing tendons in boiling water or by heating them rapidly to 67º C), some regions exhibit weaker positive birefringence while others become negative and the fibrils are aligned at right angles to each other. These findings indicate that the drastic treatment affects both intra- and intermolecular organization, probably by changing also the intramolecular cross links.

According to S. Thomsen,[71] the form birefringence of types I, II, and III collagen is a result of the longitudinal arrangement of the molecules and microfibrils stabilized by molecular cross links forming the collagen fiber. Thermally induced changes of birefringence probably result from disruption of these cross links.

3 MUELLER MATRIX AND JONES MATRIX

3.1 Stokes Vector and Mueller Matrix

In polarimetry, the polarization state of light can be completely characterized by either a Stokes vector or a Jones vector depending on whether the light is partially polarized or completely polarized. A Stokes vector **S** is constructed based on six flux measurements with different polarization analyzers in front of the detector:

$$\mathbf{S} = \begin{pmatrix} S_0 \\ S_1 \\ S_2 \\ S_3 \end{pmatrix} = \begin{pmatrix} I_H + I_V \\ I_H - I_V \\ I_P - I_M \\ I_R - I_L \end{pmatrix}, \qquad 3.1$$

where S_0, S_1, S_2, S_3 are the elements of the Stokes vector; I_H, I_V, I_P, I_M, I_R, and I_L are the light intensities measured with a horizontal linear polarizer, a vertical linear polarizer, a +45° linear polarizer, a −45° linear polarizer, a right circular analyzer, and a left circular analyzer in front of the detector, respectively. Because of the relationships $I_H + I_V = I_P + I_M = I_R + I_L = I$, where I is the intensity of the light beam measured without any analyzer in front of the detector, a Stokes vector can be determined by four independent measurements, for example, I_H, I_V, I_P, and I_R:

$$\mathbf{S} = \begin{pmatrix} I_H + I_V \\ I_H - I_V \\ 2I_P - I_H - I_V \\ 2I_R - I_H - I_V \end{pmatrix}. \qquad 3.2$$

From the Stokes vector, the degree of polarization (DOP), the degree of linear polarization (DOLP), and the degree of circular polarization (DOCP) are derived as:

$$\begin{cases} \mathrm{DOP} = \dfrac{\sqrt{S_1^2 + S_2^2 + S_3^2}}{S_0} \\ \mathrm{DOLP} = \dfrac{\sqrt{S_1^2 + S_2^2}}{S_0} \\ \mathrm{DOCP} = \dfrac{S_3}{S_0} \end{cases} . \qquad 3.3$$

DOP is a measure of the polarization purity of light. DOP = 1 means the light is completely polarized; DOP = 0 means the light is completely depolarized; DOP < 1 means the light is partially polarized. When DOP = 1, we have

$$\begin{cases} S_0 = E_{0H}^2 + E_{0V}^2 \\ S_1 = E_{0H}^2 - E_{0V}^2 \\ S_2 = 2E_{0H}E_{0V}\cos\delta \\ S_2 = 2E_{0H}E_{0V}\sin\delta \end{cases}, \qquad 3.4$$

where E_{0H} and E_{0V} are the amplitudes of the horizontal and vertical components of the electric vector of the light, respectively; δ is the phase difference between the vertical and horizontal components of the electric vector; and the Stokes vector can be expressed as:

$$\mathbf{S} = \begin{bmatrix} 1 \\ \cos 2\varepsilon \cos 2\theta \\ \cos 2\varepsilon \sin 2\theta \\ \sin 2\varepsilon \end{bmatrix}. \qquad 3.5$$

The parameters are defined and correlated with each other as follows:[72]

$$\begin{cases} \tan 2\theta = \tan 2v \cos\delta \\ \tan 2\varepsilon = \pm \sin 2\theta \tan\delta \\ \tan v = \dfrac{E_{0V}}{E_{0H}} \end{cases} . \qquad 3.6$$

The Mueller matrix (**M**) of a sample transforms an incident Stokes vector into the corresponding output Stokes vector:

$$\mathbf{S}_{out} = \begin{bmatrix} S_0 \\ S_1 \\ S_2 \\ S_3 \end{bmatrix} = \mathbf{MS}_{in} = \begin{bmatrix} M_{00} & M_{01} & M_{02} & M_{03} \\ M_{10} & M_{11} & M_{12} & M_{13} \\ M_{20} & M_{21} & M_{22} & M_{23} \\ M_{30} & M_{31} & M_{32} & M_{33} \end{bmatrix} \cdot \begin{bmatrix} S_{i0} \\ S_{i1} \\ S_{i2} \\ S_{i3} \end{bmatrix}, \qquad 3.7$$

where $\mathbf{S}_{in}$ and $\mathbf{S}_{out}$ are the incident and output Stokes vectors of the light field, respectively; S_{i0}, S_{i1}, S_{i2} and S_{i3} are the elements of the Stokes vector of the input light. S_0 and S_{i0} are the intensity of the output and input light, respectively. In Eq. 3.7, we can clearly see that M_{00} represents the intensity transformation property of the sample and contains no polarization information. Obviously, the output Stokes vector varies with the state of the incident light, but the Mueller matrix is determined only by the sample and the optical path. Correspondingly, the Mueller matrix can fully characterize the optical polarization properties of a sample. The Mueller matrix can be experimentally obtained by measurements with different combinations of source polarizers and detection analyzers. Because a general 4×4 Mueller matrix has 16 independent elements, at least 16 independent measurements must be acquired to determine a full Mueller matrix.

The Stokes vectors for the four incident polarization states, *H*, *V*, *P*, and *R*, are respectively:

$$\mathbf{S}_{Hi} = \begin{pmatrix} 1 \\ 1 \\ 0 \\ 0 \end{pmatrix}, \mathbf{S}_{Vi} = \begin{pmatrix} 1 \\ -1 \\ 0 \\ 0 \end{pmatrix}, \mathbf{S}_{Pi} = \begin{pmatrix} 1 \\ 0 \\ 1 \\ 0 \end{pmatrix}, \mathbf{S}_{Ri} = \begin{pmatrix} 1 \\ 0 \\ 0 \\ 1 \end{pmatrix}, \qquad 3.8$$

where H, V, P, and R, represent horizontal linear polarization, vertical linear polarization, +45° linear polarization, and right circular polarization, respectively. We may express the 4×4 Mueller matrix as:

$$\mathbf{M} = \lfloor \mathbf{M}_0 \quad \mathbf{M}_1 \quad \mathbf{M}_2 \quad \mathbf{M}_3 \rfloor, \qquad 3.9$$

where $\mathbf{M}_0$, $\mathbf{M}_1$, $\mathbf{M}_2$, and $\mathbf{M}_3$ are four column vectors of four elements each. The four output Stokes vectors corresponding to the four incident polarization states H, V, P, and R are denoted respectively by $\mathbf{S}_H$, $\mathbf{S}_V$, $\mathbf{S}_P$, and $\mathbf{S}_R$. These four output Stokes vectors are experimentally measured based on Eq. 3.2 and can be expressed as:

$$\begin{cases} \mathbf{S}_H = \mathbf{M}\mathbf{S}_{H_i} = \mathbf{M}_0 + \mathbf{M}_1 \\ \mathbf{S}_V = \mathbf{M}\mathbf{S}_{Vi} = \mathbf{M}_0 - \mathbf{M}_1 \\ \mathbf{S}_P = \mathbf{M}\mathbf{S}_{Pi} = \mathbf{M}_0 + \mathbf{M}_2 \\ \mathbf{S}_R = \mathbf{M}\mathbf{S}_{Ri} = \mathbf{M}_0 + \mathbf{M}_3 \end{cases}. \qquad 3.10$$

The Mueller matrix can then be calculated from the output Stokes vectors:

$$\mathbf{M} = \frac{1}{2}\left[\mathbf{S}_H + \mathbf{S}_V \quad \mathbf{S}_H - \mathbf{S}_V \quad 2\mathbf{S}_P - \mathbf{S}_H \quad 2\mathbf{S}_R - \mathbf{S}_H - \mathbf{S}_V\right]. \qquad 3.11$$

In other words, at least four independent Stokes vectors for different source polarization states must be measured to determine a full Mueller matrix, where each Stokes vector requires four independent intensity measurements with different analyzers

3.2 Jones Vector and Jones Matrix

A 2×1 complex Jones vector is composed of the horizontal and vertical components of the electric vector and is used to characterize the polarization state of a completely polarized light (DOP = 1). A Jones matrix (**J**) transforms an input Jones vector ($\mathbf{E}_{in}$) into an output Jones vector ($\mathbf{E}_{out}$):

$$\mathbf{E}_{OUT} = \begin{bmatrix} E_{OH} \\ E_{OV} \end{bmatrix} = \mathbf{J}\mathbf{E}_{IN} = \begin{bmatrix} J_{11} & J_{12} \\ J_{21} & J_{22} \end{bmatrix} \cdot \begin{bmatrix} E_{iH} \\ E_{iV} \end{bmatrix}, \qquad 3.12$$

where E_{OH} and E_{OV} are the horizontal and vertical components of the electric vector of the output light field; E_{iH} and E_{iV} are the horizontal and vertical components of the electric vector of the input light field.

An optical polarization element is called homogeneous when the two eigenvectors of its Jones matrix are orthogonal.[73,74] A retarder or a polarizer (diattenuator) is called elliptical when its eigen-polarizations are elliptical polarization states. The Jones matrix of a homogenous partial polarizer ($\mathbf{J}_P$) can be expressed as:

$$\mathbf{J}_P = \begin{bmatrix} P_q \cos^2\theta_d + P_r \sin^2\theta_d & (P_q - P_r)\sin\theta_d \cos\theta_d \exp(-i\Delta) \\ (P_q - P_r)\sin\theta_d \cos\theta_d \exp(i\Delta) & P_q \sin^2\theta_d + P_r \cos^2\theta_d \end{bmatrix}, \qquad 3.13$$

where θ_d is an auxiliary angle; P_q, P_r are the principal coefficients of the amplitude transmission, or eigenvalues, for the two orthogonal polarization eigen-states:

$$\begin{bmatrix} \cos\theta_d \\ \sin\theta_d \exp(i\Delta) \end{bmatrix} \text{ and } \begin{bmatrix} -\sin\theta_d \exp(-i\Delta) \\ \cos\theta_d \end{bmatrix}.$$

The Jones matrix of a homogenous elliptical retarder can be expressed as:

$$\mathbf{J}_R = \begin{bmatrix} \cos^2\theta\exp(i\frac{\varphi}{2})+\sin^2\theta\exp(-i\frac{\varphi}{2}) & i\sin(\frac{\varphi}{2})\sin(2\theta)\exp(-i\delta) \\ i\sin(\frac{\varphi}{2})\sin(2\theta)\exp(i\delta) & \sin^2\theta\exp(i\frac{\varphi}{2})+\cos^2\theta\exp(-i\frac{\varphi}{2}) \end{bmatrix}, \qquad 3.14$$

where the fast and slow eigen-vectors are

$$\begin{bmatrix} \cos\theta \\ \sin\theta\exp(i\delta) \end{bmatrix} \text{ and } \begin{bmatrix} -\sin\theta\exp(-i\delta) \\ \cos\theta \end{bmatrix},$$

respectively; the angle θ is an auxiliary angle of the fast eigen-vector; δ represents the phase difference between the two components of the fast eigen-vector; and φ is the phase difference (retardation) between the two eigen-values. If $\delta = 0$, the retarder is linear and θ represents the orientation of the fast axis. Correspondingly, θ_d represents the orientation of $\mathbf{J}_P$ if $\Delta = 0$.

Linear polarizers and linear and circular retarders are typical homogeneous polarizing optical elements. A typical example of inhomogeneous polarizing elements is the circular polarizer, whose Jones matrix is $\frac{1}{2}\begin{bmatrix} 1 & 1 \\ i & i \end{bmatrix}$, which is constructed by using a linear polarizer set at 45° followed by a λ/4 plate with its fast axis set at horizontal. The eigenvectors of such a circular polarizer are $\frac{1}{\sqrt{2}}\begin{bmatrix} 1 \\ -1 \end{bmatrix}$ for a –45° linear polarization state and $\frac{1}{\sqrt{2}}\begin{bmatrix} 1 \\ i \end{bmatrix}$ for a right circular polarization state, which are not orthogonal.

The Jones matrix of a non-depolarizing optical system can be transformed into an equivalent non-depolarizing Mueller matrix by the following relationship:[72]

$$\begin{aligned}\mathbf{M} &= \mathbf{U}\left(\mathbf{J}\otimes\mathbf{J}^*\right)\mathbf{U}^{-1}\\ &= \mathbf{U}\begin{bmatrix} J_{11}\mathbf{J}^* & J_{12}\mathbf{J}^* \\ J_{21}\mathbf{J}^* & J_{22}\mathbf{J}^* \end{bmatrix}\mathbf{U}^{-1} \qquad ; \\ &= \mathbf{U}\begin{bmatrix} J_{11}J_{11}^* & J_{11}J_{12}^* & J_{12}J_{11}^* & J_{12}J_{12}^* \\ J_{11}J_{21}^* & J_{11}J_{22}^* & J_{12}J_{21}^* & J_{12}J_{22}^* \\ J_{21}J_{11}^* & J_{21}J_{12}^* & J_{22}J_{11}^* & J_{22}J_{12}^* \\ J_{21}J_{21}^* & J_{21}J_{22}^* & J_{22}J_{21}^* & J_{22}J_{22}^* \end{bmatrix}\mathbf{U}^{-1}\end{aligned} \tag{3.15}$$

and a Jones vector of a light field can be transformed into a Stokes vector by

$$\begin{aligned}\mathbf{S} &= \sqrt{2}\mathbf{U}\left(\mathbf{E}\otimes\mathbf{E}^*\right) = \sqrt{2}\mathbf{U}\begin{bmatrix} E_H\mathbf{E}^* \\ E_V\mathbf{E}^* \end{bmatrix} \\ &= \sqrt{2}\mathbf{U}\begin{bmatrix} E_H E_H^* \\ E_H E_V^* \\ E_V E_H^* \\ E_V E_V^* \end{bmatrix} \qquad ,\end{aligned} \tag{3.16}$$

where ⊗ represents the Kronecker tensor product and **U** is the 4×4 Jones–Mueller transformation matrix:

$$\mathbf{U} = \frac{\mathbf{1}}{\sqrt{\mathbf{2}}}\begin{bmatrix} \mathbf{1} & \mathbf{0} & \mathbf{0} & \mathbf{1} \\ \mathbf{1} & \mathbf{0} & \mathbf{0} & -\mathbf{1} \\ \mathbf{0} & \mathbf{1} & \mathbf{1} & \mathbf{0} \\ \mathbf{0} & \boldsymbol{i} & -\boldsymbol{i} & \mathbf{0} \end{bmatrix}.$$

3.3 Jones and Mueller Matrices of Standard Elements

(1). The Jones matrix of a linear retarder with fast axis θ and phase retardation φ:

$$\begin{bmatrix} \cos^2\theta\exp(i\frac{\varphi}{2}) + \sin^2\theta\exp(-i\frac{\varphi}{2}) & i\sin(\frac{\varphi}{2})\sin(2\theta) \\ i\sin(\frac{\varphi}{2})\sin(2\theta) & \sin^2\theta\exp(i\frac{\varphi}{2}) + \cos^2\theta\exp(-i\frac{\varphi}{2}) \end{bmatrix}.$$

(2). The Mueller matrix of a linear retarder with fast axis θ and phase retardation φ:

$$\begin{bmatrix} 1 & 0 & 0 & 0 \\ 0 & \cos^2 2\theta + \sin^2 2\theta\cos\varphi & \sin 2\theta\cos 2\theta(1-\cos\varphi) & -\sin 2\theta\sin\varphi \\ 0 & \sin 2\theta\cos 2\theta(1-\cos\varphi) & \sin^2 2\theta + \cos^2 2\theta\cos\varphi & \cos 2\theta\sin\varphi \\ 0 & \sin 2\theta\sin\varphi & \cos 2\theta\sin\varphi & \cos\varphi \end{bmatrix}.$$

(3) The Jones matrix of a circular retarder with phase retardation φ:

$$\begin{bmatrix} \cos(\frac{\varphi}{2}) & \sin(\frac{\varphi}{2}) \\ -\sin(\frac{\varphi}{2}) & \cos(\frac{\varphi}{2}) \end{bmatrix}.$$

(4). The Mueller matrix of a circular retarder with phase retardation φ:

$$\begin{bmatrix} 1 & 0 & 0 & 0 \\ 0 & \cos\varphi & \sin\varphi & 0 \\ 0 & -\sin\varphi & \cos\varphi & 0 \\ 0 & 0 & 0 & 1 \end{bmatrix}.$$

(5). The Mueller matrix of a linear diattenuator with axis θ and intensity transmittances q and r:

$$\frac{1}{2}\begin{bmatrix} q+r & (q-r)\cos 2\theta & (q-r)\sin 2\theta & 0 \\ (q-r)\cos 2\theta & (q+r)\cos^2 2\theta + 2\sqrt{qr}\sin^2 2\theta & (q+r-2\sqrt{qr})\sin 2\theta\cos 2\theta & 0 \\ (q-r)\sin 2\theta & (q+r-2\sqrt{qr})\sin 2\theta\cos 2\theta & (q+r)\sin^2 2\theta + 2\sqrt{qr}\cos^2 2\theta & 0 \\ 0 & 0 & 0 & 2\sqrt{qr} \end{bmatrix}.$$

4 SINGLE-CHANNEL MUELLER-MATRIX OCT

4.1 Experimental System

The single-channel Mueller-matrix OCT system measures the Mueller matrix of a sample by using an algorithm based on Eq. 3.11. Fig. 4.1 shows the schematic of the experimental system. A superluminescent diode with a center wavelength of 850 nm and a FWHM bandwidth of 26 nm is used as the light source. The light intensity after the linear polarizer LP is 400 μW. After passing through the polarizer, the half-wave plate HW, and the quarter-wave plate QW, the light is split by a nonpolarization beam splitter (NBS). The sample beam is focused into the sample by an objective lens with an N.A. of 0.15. The reference beam passes through a variable-wave plate and is back reflected by the reference mirror. After recombined by the NBS, the reflected beams from the reference and sample arms are coupled into a single-mode fiber and detected by a silicon photodiode. The minimal detectable signal of the system is −100 dB. The depth and lateral scans are accomplished by DC-motor driven translation stages. The speed of the depth scan is limited by the velocity of the translation stage, which is 0.5 mm/s. The back travel of the translation stage is not used due to its instability and results a duty cycle of about 50%. As a result, a single depth scan of 1.5 mm takes about 6 seconds. A depth resolution of about 10 μm can be achieved with the light source used. The step size of the lateral scan is also 10 μm. The focal spot size of the objective lens is 6.9 μm in air and is larger in tissue. The lateral resolution is expected to be also around 10 μm.

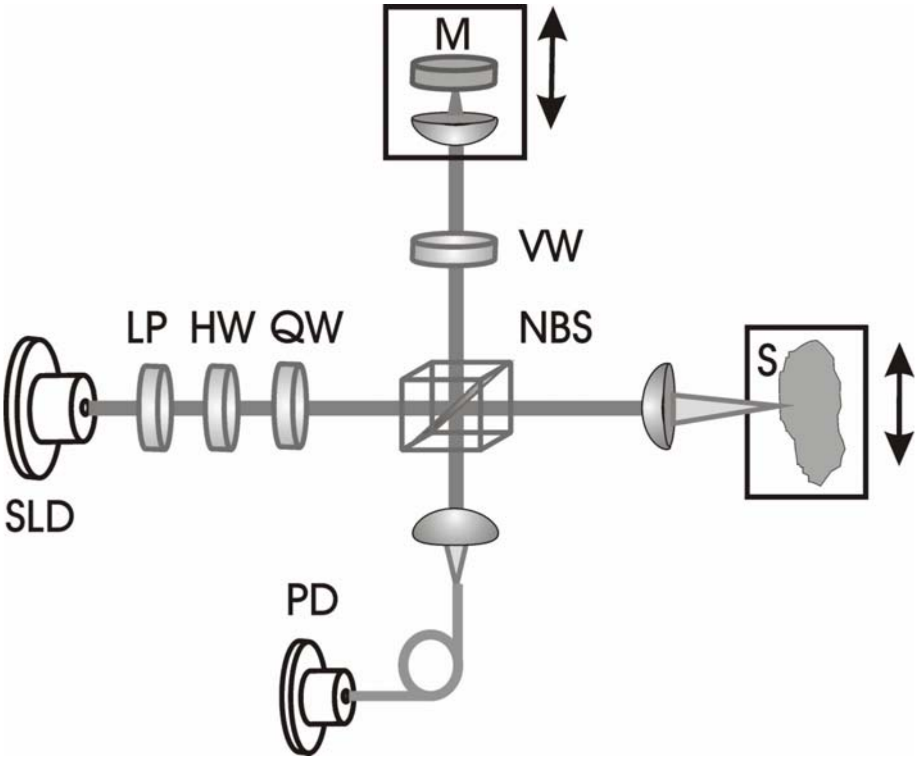

Fig. 4.1 Schematic of the single-channel Mueller-matrix OCT system: SLD, superluminescent diode; LP: linear polarizer; HW: zero-order half-wave plate; QW: zero-order quarter-wave plate; NBS: non-polarization beam splitter; VW: variable-wave plate; M: mirror; PD: photodiode.

We achieve four different incident polarization states *H*, *V*, *P*, and *R* by rotating the half-wave plate (HW) and the quarter-wave plate (QW) in the source arm. For each of these four incident polarization states, the variable-wave plate (VW) at the reference arm is adjusted to sequentially achieve the *H*, *V*, *P*, and *R* analyzing polarization states. The light intensities of both the source arm and the reference arm are measured for each of the 16 combinations of the polarization states in the source and reference arms. The source intensity is measured for calibration purpose. The reference intensities are used to convert the OCT signals for calculations of Stokes vectors and Mueller matrices.

The detected signal is amplified and then filtered with a band pass filter centered at the carrier frequency of 1.2 kHz to extract the interference signal. After rectification and envelope extraction with hardware, the signal is sampled with a data acquisition (DAQ) board (NI PCI-6032E) and processed with a personal computer.

4.2 Measuring the Stokes Vectors and Mueller Matrix of Biological Samples

A total of 16 polarization-sensitive OCT images are acquired and processed to obtain the 16 Mueller matrix images $[M_{ij}]$ according to Eq. 3.11. Alternatively, if the Stokes vector of the backscattered light is sought for a given incident polarization state, only four measurements need to be acquired by varying the reference polarization state. The Stokes vector is then calculated based on Eq. 3.2.

The OCT system was carefully calibrated and validated. The four incident polarization states, as well as the four reference polarization states associated with each incident polarization state, were examined in terms of polarization purity. The polarization purity is defined as I_{min}/I_{max}, where I_{max} is the signal intensity of the designed polarization state, and I_{min} is the intensity of the orthogonal polarization state. The measured I_{min}/I_{max} is less than 0.15% for all of the polarization states. Because the beam splitter is not an ideal polarization-independent optical element, the Mueller matrix of the beam splitter was measured for calibration. The Mueller matrices of simple optical elements measured with our setup agree with their known ideal matrices to within an error of 5% – 10% after calibration with the measured Mueller matrix of the beam splitter.

Two-dimensional images of the Stokes parameters for incident light of right circular and linear horizontal polarization states are shown in Fig. 4.2. The sample is a piece of fish bone from the head. The image size is 1.5 mm in optical depth and 0.5 mm in the lateral dimension. The 1.5 mm optical depth may be converted to approximately 1.0 mm in physical depth assuming the index of refraction of the bone sample is 1.5. The symbols consisting of double polarization states represent an OCT measurement with the source polarization state denoted by the left letter and the reference polarization state denoted by the right letter. For example, HV refers to an OCT measurement acquired with an H-polarized incident field and a V-polarized reference field. The original 2D image data were averaged over 20 measurements. In the figure we can clearly see the difference among the different elements of the Stokes vector. The four $S1$ and $S3$ images reveal some structures in the central region of about 0.2 mm×0.5 mm that are not seen in the other four Stokes images. The structures in the four $S1$ and $S3$ images of both the incident polarization states are similar in both the shape and size. However, the central region in $SR1$ has higher intensity than the surrounding region and looks solid, while the central regions in $SR3$, $SH1$, and $SH3$ have lower intensity than the surrounding regions and look like voids. The central imaged region of the sample must have different optical polarization properties from the surrounding region and must have changed the polarization state of backscattered light from this region differently. The change of polarization state may be attributed to both optical birefringence and scattering.

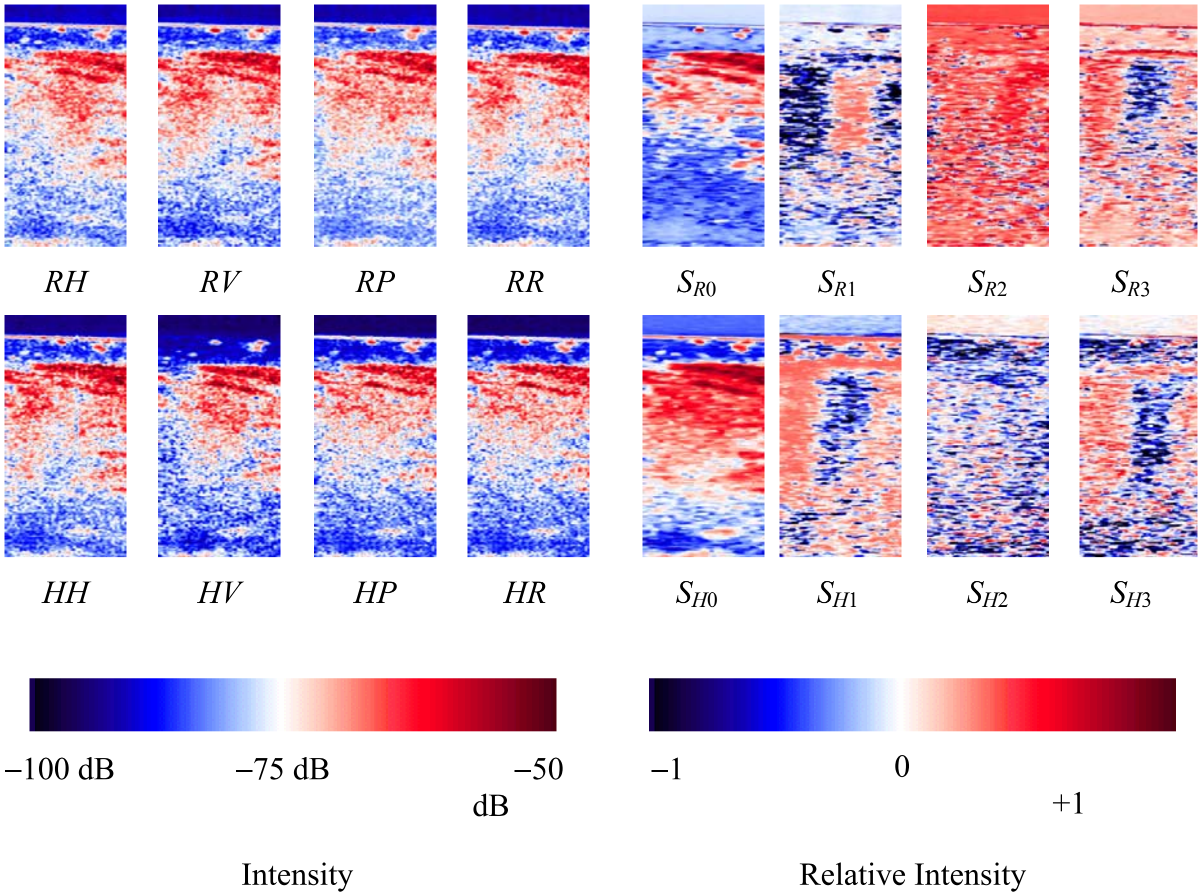

(a) (b)

Fig. 4.2 (a) Raw 2D OCT images. (b) Stokes images. All the images share the same color map. The upper boundary in each image represents the incident surface of the glass plate used for fixing the bone sample. The physical size of each image is 1.0 mm × 0.5 mm.

We measured the 2D Mueller-matrix images of another region of the fish bone sample. The raw images and the images of the corresponding 16 Mueller-matrix elements are shown in Fig. 4.3. A total of 16 measurements were acquired. The four Stokes vectors corresponding to the four incident polarization states were first calculated using Eq. 3.2 and then were used to calculate the Mueller matrix according to Eq. 3.11. The Mueller-matrix images were compensated with the Mueller matrix of a sample mirror and the beam splitter to account for the polarization effect of the beam splitter, which was measured to be:

$$\mathbf{M}_{cal} = \begin{bmatrix} 1.0000 & -0.0420 & -0.0028 & -0.0479 \\ -0.0405 & 0.9975 & -0.0591 & -0.0306 \\ -0.0095 & -0.0004 & 1.0671 & 0.2089 \\ -0.0134 & -0.0182 & 0.2008 & 1.0999 \end{bmatrix}.$$

The image size is 1.0 mm in optical depth and 0.5 mm in the lateral dimension. The 1.0 mm optical depth may be converted to approximately 0.67 mm in physical depth assuming the index of refraction of the bone sample is 1.5. From the 16 raw images [Fig. 4.3(a)], the degradation effect on the incident polarization state can be clearly seen. Some regions of the *HV* and *VH* images have strong cross-polarized signals, shown as red spots in the images, and the corresponding locations in the co-polarized *HH* and *VV* images have strong signals as well. Therefore, the incident light is partially converted to the cross-polarization state by the clusters in these regions. In most other regions, the back-scattered light still preserves most of the original polarization state because the co-polarized signals are much stronger than the cross-polarized signals.

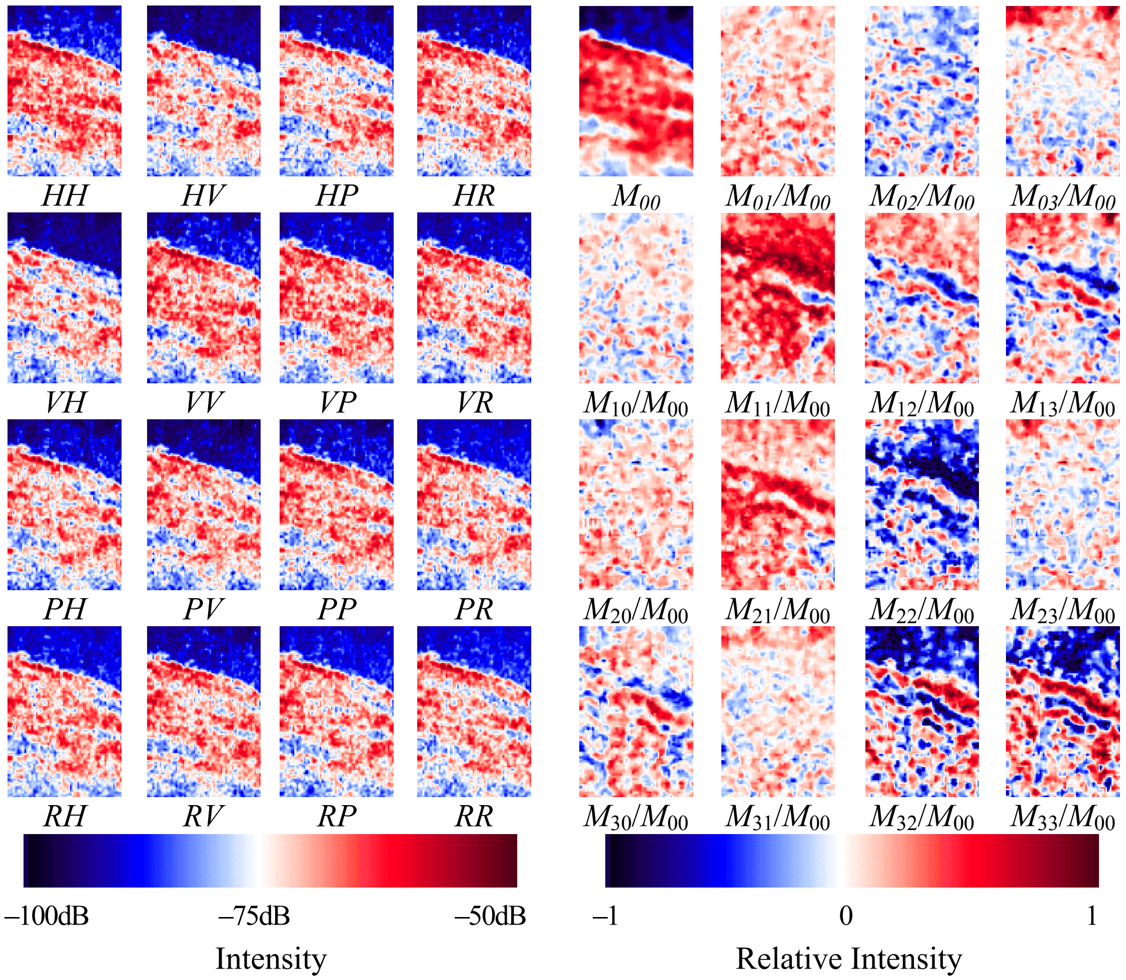

(a) Raw OCT Images

(b) Mueller Matrix Images

Fig. 4.3 (a) Raw OCT images. (b) Normalized Mueller-matrix images. All the images share the same color map. The physical size of each image is 0.67 mm × 0.5 mm.

The processed 4×4 Mueller-matrix images are shown in Fig. 4.3(b). The image of the Mueller-matrix element M_{00} corresponds to a polarization-independent image as acquired by a nonpolarization OCT system. The other Mueller-matrix elements M_{ij} are pixel-wise normalized by M_{00} image. The polarization-independent element M_{00} reveals significantly less information than the other elements as clearly shown in. Fig. 4.3(b). Strong layered structures are clearly seen in some of the images such as M_{12}, M_{13}, M_{22}, M_{32}, and M_{33}.

We also measured the 2D Mueller-matrix images of a piece of rat bone. The raw images and the images of the corresponding 16 Mueller-matrix elements are shown in Fig. 4.4. The image size is 1.0 mm in optical depth and 0.5 mm in the lateral dimension. All the Mueller-matrix elements M_{ij} except M_{00} are pixel-wise normalized by M_{00} image.

Only the Mueller matrices of solid samples were measured so far for stability consideration because soft samples would vibrate within the current acquisition time. Once the scanning speed is increased and the system is fully automated, soft tissue samples may be measured, which would greatly enhance the application of this technique. The technique can furnish depth-resolved Mueller-matrix characterization of native biological tissue either *in vivo* or *in vitro* with high spatial resolution. Analysis of the Mueller matrix can extract information of the origin of polarization effect, which is related to the local anisotropic structure within the sample. Detailed interpretation of the Mueller matrices can reveal much more information about the local structures. Further investigations should be warranted in this direction.

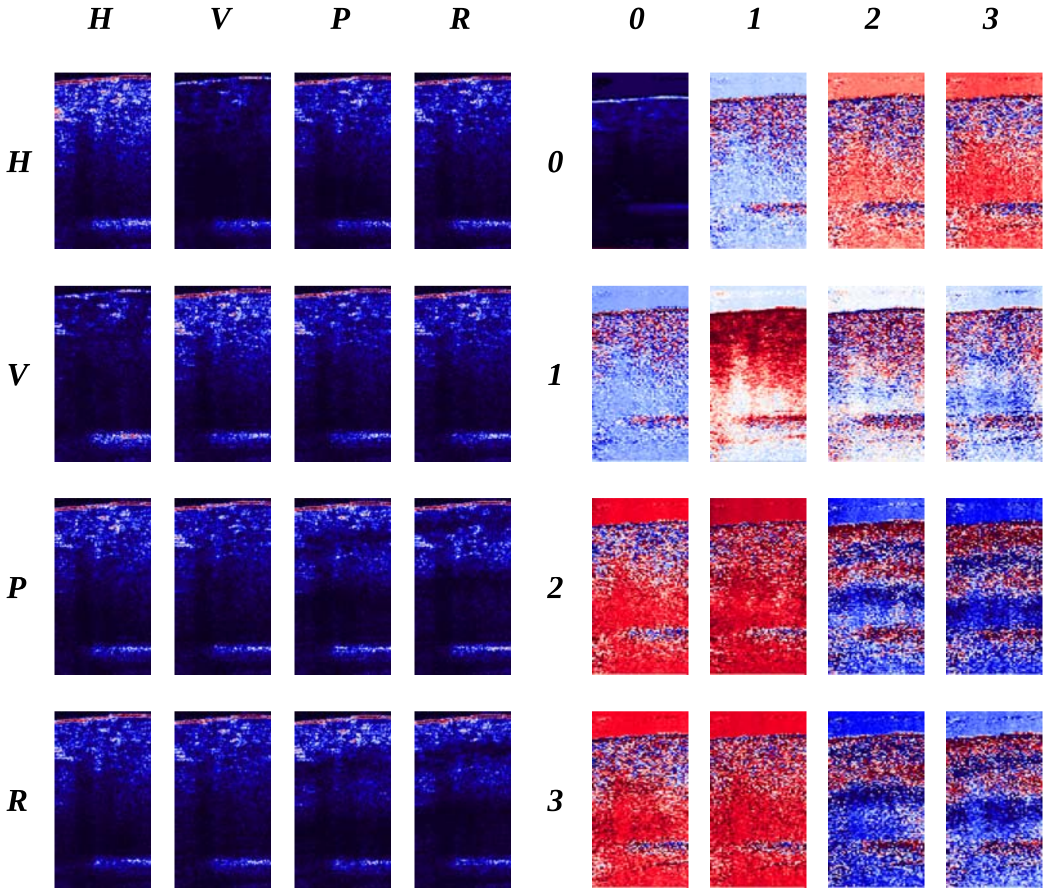

Fig. 4.4 The raw 2-D images and the 2-D images of the corresponding Mueller matrix of a piece of fish bone.

4.3 Measuring the Degree of Polarization

We measured the Stokes vector **S***H* of 1%, 2%, and 5% *Intralipid* solutions and a piece of bone tissue from the head of a yellow croaker fish, where the incident light was in the state of horizontal linear polarization (*H*). The Stokes vectors were then used to calculate the DOP, DOLP, and DOCP for each sample. The results are shown in Fig. 4.5 and Fig. 4.6, where the optical depth means the product between the physical depth and the refractive index of the sample. Fig. 4.5(a) shows the *SH*0 and DOP for the 5% *Intralipid* solution; Fig. 4.5(b) shows the DOLP and DOCP for the 5% *Intralipid* solution; Fig. 4.5 (c) shows the DOP for the 1%, 2%, and 5% *Intralipid* solutions. Fig. 4.6(a) shows the *SH*0 and DOP for the bone sample; Fig. 4.6(b) plots the corresponding DOLP and DOCP.

All the data were averaged over 20 scans. Polynomial fitting was applied to the data for the *Intralipid* solutions to reduce the fluctuation before calculating the Stokes vectors. The difference in the degree of polarization is striking between the liquid and the solid samples. For the liquid samples, the DOP and DOLP decrease as the optical depth increases as shown in Fig. 4.5. The DOCP has a small value that is most likely caused by noise, indicating negligible anisotropy or birefringence. The DOP decreases with increasing concentration of *Intralipid* and decreases with the optical depth faster for higher concentration of *Intralipid* as shown in Fig. 4.5(c).

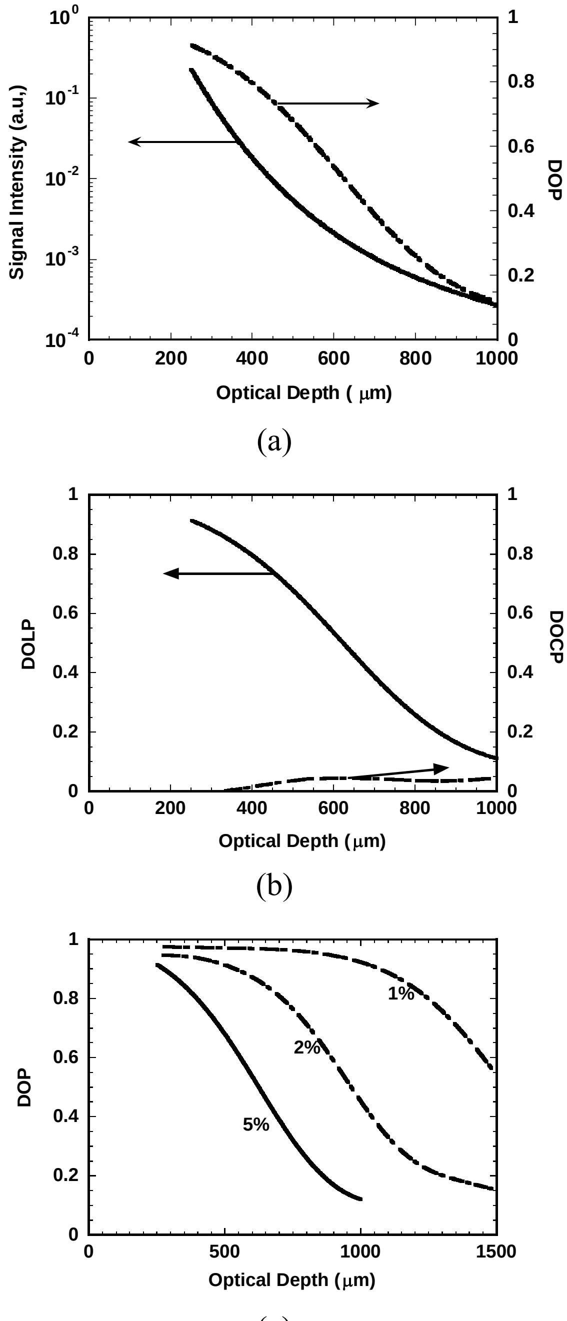

(a)

(b)

(c)

Fig. 4.5 (a) S_{H0} and DOP for 5% *Intralipid* solution. (b) DOLP and DOCP for 5% *Intralipid* solution. (c) DOP for 1%, 2% and 5% *Intralipid* solution.

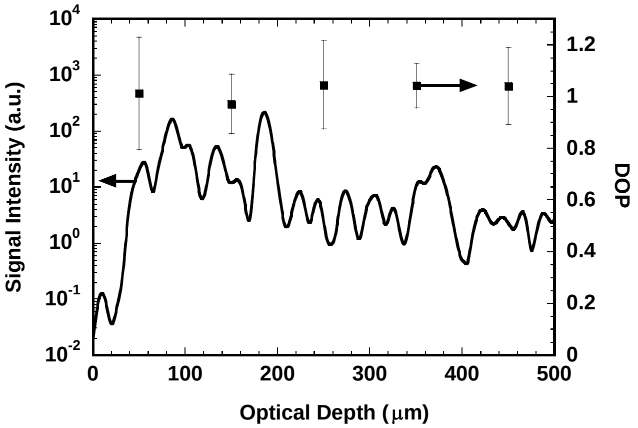

(a)

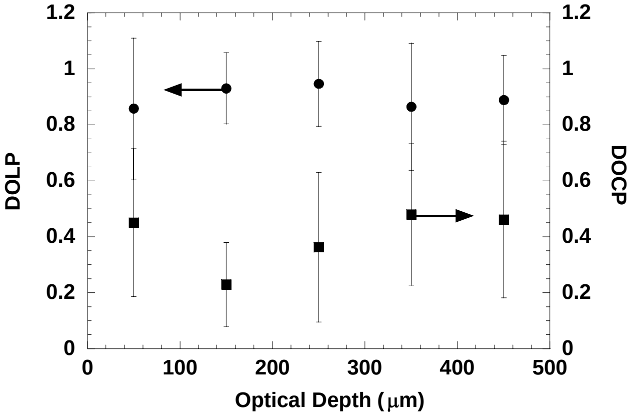

(b)

Fig. 4.6 (a) S_{H0} and DOP for a bone tissue from the head of a yellow croaker fish. (b) DOLP, and DOCP for the same region of the sample.

For the solid sample, however, the DOP is approximately unity throughout the detectable range of optical depth apart from the fluctuation as shown in Fig. 4.6(a). The fluctuation of the DOP around unity for the solid sample is likely caused by the anisotropy of optical properties of the sample, which was not observed in the isotropic liquid samples. Anisotropy such as birefringence would cause the same physical feature to appear at different optical depths when it is measured with different analyzing polarization states. Conversely, the four quantities measured with different analyzing polarization states at a given optical depth may correspond to signals from slightly different physical depths. It would be challenging to accurately align the physical features among the one-dimensional depth-scan images of different analyzing polarization states. This slight misalignment causes the fluctuation of DOP. The DOLP and the DOCP are complementary to each other as shown in Fig. 4.6(b), confirming the existence of optical birefringence in the sample.

The salient difference in degree of polarization between the liquid and solid samples indicates that a liquid medium acts upon our OCT signals differently from a solid medium. The variation of DOP with the optical depth and the solution concentration signifies that the apparent depolarization effect in liquid increases with the depth and the concentration. In principle, a DOP of less than unity means that the detected backscattered light is partially depolarized. Due to scattering, the completely polarized incident light is converted into non-uniformly polarized scattered light. If conventional intensity-based measurements were employed to detect the polarization property of this non-uniformly polarized light, the DOP would be less than unity and decrease with increasing scattering. The reduction of DOP is because that the light impinging upon different locations on the analyzers in front of the detector has different polarization states and adds in intensity after passing through the analyzers. The intensity signals of the light from different locations measured with orthogonal analyzers will partially offset each other in the calculation of the Stokes vector while the total intensity measured without analyzers is always the sum of the light from all of the locations.

However, OCT is an amplitude-based detection system by interference heterodyne. OCT detects the electric field of only the coherent part of the backscattered light. As is shown in Eq. 4.1, the electric field of the light from different locations of the detector is projected onto the analyzing polarization state $\mathbf{E_r}$, then added in amplitude. Equivalently, the electric field of the light from different locations of the detector is summed in vector, and the vector sum $\mathbf{E_s}$ is then projected onto the analyzing polarization state. Because of this coherent detection scheme in OCT, a DOP of unity is maintained despite scattering as observed in the solid sample. Therefore, the conventional depolarization process in intensity-based measurements does not account for the decrease of DOP in the liquid media.

$$\begin{aligned} \boldsymbol{I} &= \mathbf{E_r} \cdot \mathbf{E_{s1}} + \mathbf{E_r} \cdot \mathbf{E_{s2}} + \mathbf{E_r} \cdot \mathbf{E_{s3}} + \mathbf{...} \\ &= \mathbf{E_r} \cdot (\mathbf{E_{s1}} + \mathbf{E_{s2}} + \mathbf{E_{s3}} + \mathbf{...}) \\ &= \mathbf{E_r} \cdot \mathbf{E_s} \\ \mathbf{E_s} &= \mathbf{E_{s1}} + \mathbf{E_{s2}} + \mathbf{E_{s3}} + \mathbf{...} \end{aligned} \tag{4.1}$$

We conjecture that the decrease of the apparent DOP in liquid is caused by the Brownian motion of the scattering particles and the signal averaging in the data acquisition. Brownian motion causes the polarization state of the backscattered light to fluctuate around an average state. Because our OCT system converts the interference fringes into an envelope of rectified fringes, only this positive envelope is detected and averaged.

To illustrate this point, we let *IH*, *IV*, *IP*, and *IR* denote the intensities of the average polarization state analyzed by horizontal linear polarization, vertical linear polarization, +45° linear polarization, and right circular polarization state, respectively. Let *In* denote the average intensity caused by the Brownian fluctuation, which is assumed to be the same for all of the four measurements with different analyzers for simplicity. The measured Stokes vector can be expressed as:

$$\mathbf{S}'=\begin{pmatrix} I_H+I_V \\ I_H-I_V \\ 2I_P-I_H-I_V \\ 2I_R-I_H-I_V \end{pmatrix}+\begin{pmatrix} 2I_n \\ 0 \\ 0 \\ 0 \end{pmatrix}=\mathbf{S}+\mathbf{S}_n \qquad 4.2$$

The DOP of **S** is unity while the DOP of $\mathbf{S}_n$ is zero. The DOP of **S'** is

$$\mathrm{DOP}(\mathbf{S}')=\mathrm{DOP}(\mathbf{S})\frac{S_0}{S_0+2I_n}=\frac{S_0}{S_0+2I_n}\,. \qquad 4.3$$

As can be seen, the apparent DOP of the measured Stokes vector is less than unity. The increase of *Intralipid* concentration means an increase of random scattering that the light encounters per unit optical depth. An increase in optical depth means that the backscattered light encounters more scattering events. The increased scattering events would cause more fluctuation because each scattering event has Brownian motion. Therefore, the average intensity I_n would increase with both the optical depth and scatterer concentration in liquid, which would accordingly decrease the apparent DOP. This conjecture can be ultimately tested if our setup is improved such that the Stokes vector of a liquid sample can be measured in a sufficiently short time period.

5 MULTI-CHANNEL MUELLER-MATRIX OCT

5.1 Introduction

The combination between Mueller calculus and OCT offers a unique way to acquire the Mueller matrix of a scattering sample with OCT resolution. Our single-channel Mueller-matrix OCT system can acquire two-dimensional depth-resolved Mueller-matrix images of biological tissues based on 16 combinations of source and analyzing polarization states. However, the relatively time-consuming nature of the measurement process limited the application of the technique to stable samples such as bones. In section 4.3, we demonstrated that the degree of polarization (DOP) of the backscattered light measured by OCT is unity throughout the detection range, where a DOP of unity indicates that the measured Mueller matrix is non-depolarizing. This conclusion allows the use of a Jones matrix, instead of a Mueller matrix, in OCT.

To measure less stable samples such as soft tissues, a system that can determine the Jones matrix with a single depth scan (A-scan) is desired. In other words, this system should be capable of acquiring the Jones matrix as fast as its conventional OCT counterpart can acquire a regular image. The measured Jones matrix can be further transformed into an equivalent Mueller matrix if desired.

Unlike a Mueller matrix, which is suitable for all kinds of optical systems, a Jones matrix can only be applied to a non-depolarizing optical system. A Jones matrix can completely characterize the polarization properties of a non-depolarizing optical system. In other words, for a non-depolarizing optical system, a Jones matrix is equivalent to a Mueller matrix. A Jones matrix has four complex elements, in which one phase is arbitrary and consequently seven real parameters are independent. Equivalently, there are seven independent parameters in a non-depolarizing Mueller matrix.

When the two matrices are equivalent, one matrix is preferred to the other in some situations. A Jones matrix has fewer elements and the physical meanings of the matrix elements are clearer. On the other hand, a Mueller matrix uses only real numbers; and the intensity transformation property of a sample is explicitly expressed in its M_{00} element, which provides an image of the sample without the influence of its polarization property. M_{00} contains no polarization artifact such as is usually encountered in a conventional OCT image when the sample contains birefringence. Therefore, a Mueller matrix clearly separates the structural information from the polarization information of a sample.

5.2 Experimental System

The schematic of the experimental setup is shown in Fig 5.1. Two super luminescent diodes (SLD) are employed as low-coherence light sources and are amplitude modulated at 3 kHz and 3.5 kHz by modulating the injection current. The two light sources are in horizontal and vertical polarization states, respectively, and each delivers about 200 μw of power to the sample. The central wavelength, FWHM bandwidth, and the output power of the light sources are 850 nm, 26 nm, and 3 mw, respectively. The Jones vectors of the two sources are $\begin{bmatrix} 1 \\ 0 \end{bmatrix}$ and $\begin{bmatrix} 0 \\ 1 \end{bmatrix}$, respectively. The two source beams are merged by a polarizing beam splitter (PBS1), filtered by a spatial filter assembly and then split into the reference arm and the sample arm by a non-polarizing beam splitter (NBS). The sample beam passes through a quarter-wave plate (λ/4 plate), the fast axis of which is oriented at 45° and is focused into the sample by an objective lens (L1: f = 15 mm and NA = 0.25). The Jones vectors of the sample beam at the sample surface for the two sources are $\begin{bmatrix} 1 \\ i \end{bmatrix}$ and $\begin{bmatrix} 1 \\ -i \end{bmatrix}$, which are right-circularly and left-circularly polarized, respectively. The reference arm consists of a λ/4 plate, the fast axis of which is oriented at 22.5°, a lens (L2), and a mirror. After retro-reflection by the reference mirror and double passing through the λ/4 plate, the horizontal polarization (*H*) of the incident light is converted into 45° polarization, $\begin{bmatrix} 1 \\ 1 \end{bmatrix}$, while the vertical polarization (*V*) of the incident light is converted into –45° polarization, $\begin{bmatrix} 1 \\ -1 \end{bmatrix}$, and then the reference beam combines with the backscattered sample beam through the NBS. The combined light is split into two orthogonal polarization components, i.e. the horizontal and vertical components of the Jones vector, by a polarization beam splitter PBS2. The two components are coupled into two single-mode fibers with objective lenses. The two polarization components are detected by photodiodes PDH and PDV, respectively. A data-acquisition board (DAQ board) sampling at 50 kHz/channel digitizes the two signals. The scan speed of the reference arm is 0.5 mm/s generating a Doppler frequency of about 1.2 kHz. The carrier frequencies, 1.8 kHz, 2.3 kHz, 4.2 kHz and 4.7 kHz, are the beat and sum frequencies between this Doppler frequency and the modulation frequencies of the light sources.

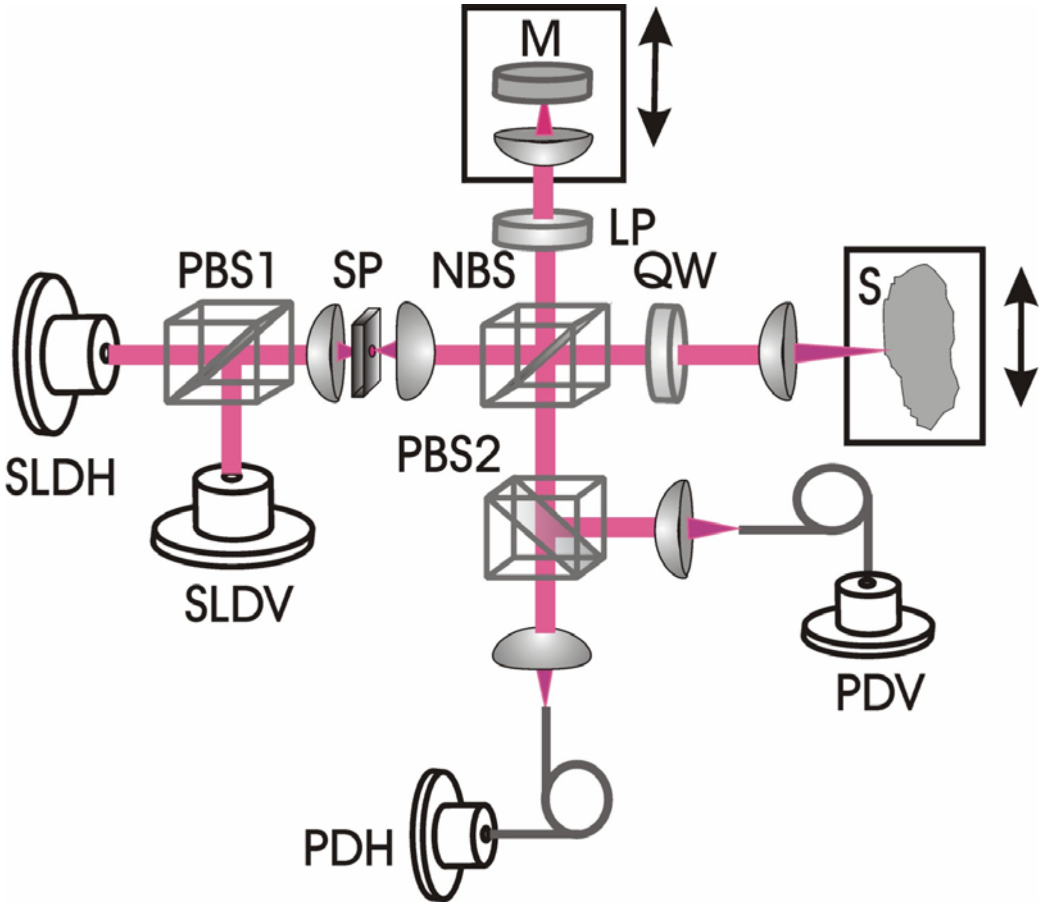

Fig 5.1 Schematic of the multi-channel Mueller OCT system. SLDH and SLDV: superluminescent diodes, horizontally polarized (*H*) and vertically polarized (*V*), respectively; PBS1 and PBS2: polarizing beam splitters; SF: spatial filter; NBS: non-polarizing beam splitter; LP: 45° linear polarizer; QW: λ/4 plate with fast axis oriented at 45°; M: mirror; PDH and PDV: photodiodes for the *H* and *V* polarization components, respectively.

The two function generators (DS345, Stanford Research Systems), which are used for the modulation of the two light sources, respectively, are synchronized and share the same time base. Burst mode was used to ensure that the initial phases of the two modulation signals are fixed for each A-scan. The time delay between the scanning of the two channels of the DAQ board is 10 μs. The phase difference between the two channels caused by this time delay for each beat and sum frequency was compensated during signal processing.

5.3 Acquisition of the Jones Matrix

In the following analysis for the interference signals, we assume:

1) The group velocity dispersion in the sample can be neglected;
2) $\Delta k / \bar{k} << 1$, i.e. the light is quasi-monochromatic, where $\bar{k}$ is the center free space wave number;
3) $\Delta n\bar{k} << n_H \bar{k}, n_V \bar{k}$, where Δn is the birefringence in the sample, n_H and n_V are the equivalent refractive index for the *H* and *V* components of the sample light.
4) The reference arm consists of a $\lambda / 4$ plate oriented at 22.5°.

Under these assumptions, the differences of the group delay among different polarization states can be neglected and there is no significant difference in the output polarization states for different spectroscopic components. We define the splitting surface of the beam splitter as the origin of the longitudinal coordinate ($z = 0$). In the following analysis, the expressions of the input and output Jones vectors ($\mathbf{E}_i$ and $\mathbf{E}_o$) do not contain the initial phase of the incident light fields. The two incident Jones vectors of the two incident polarization states for each frequency component are:

$$\begin{aligned}\mathbf{E}_{i1}(\omega_1)\exp(i\phi_{01}) &= \begin{bmatrix} E_{iH1}(\omega_1) \\ E_{iV1}(\omega_1) \end{bmatrix}\exp(i\phi_{01}) \\ &= \begin{bmatrix} A_{iH1} \\ A_{iV1} \end{bmatrix}\exp(-i\omega_1 t + i\phi_{01}) \quad , \\ &= \begin{bmatrix} |A_{iH1}| \\ |A_{iV1}|\exp(i\phi_{HV1}) \end{bmatrix}\exp(-i\omega_1 t + i\phi_{01}) \end{aligned} \tag{5.1}$$

$$\begin{aligned}\mathbf{E}_{i2}(\omega_2)\exp(i\phi_{02}) &= \begin{bmatrix} E_{iH2}(\omega_2) \\ E_{iV2}(\omega_2) \end{bmatrix}\exp(i\phi_{02}) \\ &= \begin{bmatrix} A_{iH2}(\omega_2) \\ A_{iV2}(\omega_2) \end{bmatrix}\exp(-i\omega_2 t + i\phi_{02}) \quad , \\ &= \begin{bmatrix} |A_{iH2}| \\ |A_{iV2}|\exp(i\phi_{HV2}) \end{bmatrix}\exp(-i\omega_2 t + i\phi_{02}) \end{aligned} \tag{5.2}$$

where ϕ_{01} and ϕ_{02} are the initial phases for the two incident polarization states. The roundtrip Jones matrices of the sample arm for the two incident polarization states can be expressed as

$$\begin{aligned}\mathbf{J}_{T1} &= \mathbf{J}_T \exp[i(2\bar{k}_1 l_0 + 2k_1^{'} l_g)] \\ &= \begin{bmatrix} J_{T11} & J_{T12} \\ J_{T21} & J_{T22} \end{bmatrix}\exp[i(2\bar{k}_1 l_0 + 2k_1^{'} l_g)], \end{aligned} \tag{5.3}$$

$$\begin{aligned}\mathbf{J}_{T2} &= \mathbf{J}_T \exp[i(2\bar{k}_2 l_0 + 2k_2^{'} l_g)] \\ &= \begin{bmatrix} J_{T11} & J_{T12} \\ J_{T21} & J_{T22} \end{bmatrix}\exp[i(2\bar{k}_2 l_0 + 2k_2^{'} l_g)]' \end{aligned} \tag{5.4}$$

where, J_{Tij} $(i, j = 1, 2)$ are the elements of $\mathbf{J}_T$; $k_1^{'} = k_1 - \bar{k}_1$, $k_2^{'} = k_2 - \bar{k}_2$; k_1 and $\bar{k}_1$ are the free space wave number and center wave number of source 1; k_2 and $\bar{k}_2$ are the free space wave number and center wavenumber of source 2; l_0 is the optical path length of the sample arm for the center wavelength; l_g is the group delay in the sample arm. We then have the two output Jones vectors:

$$\begin{aligned}\mathbf{E}_{o1}(\omega_1)\exp(i\phi_{01}) &= \begin{bmatrix} E_{oH1}(\omega_1) \\ E_{oV1}(\omega_1) \end{bmatrix}\exp(i\phi_{01}) \\ &= \mathbf{J}_{T1}\begin{bmatrix} |A_{iH1}| \\ |A_{iV1}|\exp(i\phi_{HV1}) \end{bmatrix}\exp(-i\omega_1 t + i\phi_{01}) \\ &= \begin{bmatrix} J_{11}|A_{iH1}| + J_{12}|A_{iV1}|\exp(i\phi_{HV1}) \\ J_{21}|A_{iH1}| + J_{22}|A_{iV1}|\exp(i\phi_{HV1}) \end{bmatrix}\exp[-i\omega_1 t + i(2\bar{k}_1 l_0 + 2k_1^{'} l_g) + i\phi_{01}]\end{aligned} \tag{5.5}$$

$$\begin{aligned}\mathbf{E}_{o2}(\omega_2)\exp(i\phi_{02}) &= \begin{bmatrix} E_{oH2}(\omega_2) \\ E_{oV2}(\omega_2) \end{bmatrix}\exp(i\phi_{02}) \\ &= \mathbf{J}_{T2}\begin{bmatrix} |A_{iH2}| \\ |A_{iV2}|\exp(i\phi_{HV2}) \end{bmatrix}\exp[-i\omega_2 t + \phi_{02}] \\ &= \begin{bmatrix} J_{11}|A_{iH2}| + J_{12}|A_{iV2}|\exp(i\phi_{HV2}) \\ J_{21}|A_{iH2}| + J_{22}|A_{iV2}|\exp(i\phi_{HV2}) \end{bmatrix}\exp[-i\omega_2 t + i(2\bar{k}_2 l_0 + 2k_2^{'} l_g) + \phi_{02}]\end{aligned} \tag{5.6}$$

The Jones matrices of the reference arm for the two polarization states are:

$$\mathbf{J}_{1r} = \frac{i\sqrt{2}}{2}\begin{bmatrix} 1 & 1 \\ 1 & -1 \end{bmatrix}\exp[i(2\bar{k}_1 l_{0r} + 2k_1^{'} l_{gr})], \tag{5.7}$$

$$\mathbf{J}_{2r} = \frac{i\sqrt{2}}{2}\begin{bmatrix} 1 & 1 \\ 1 & -1 \end{bmatrix}\exp[i(2\bar{k}_2 l_{0r} + 2k_2^{'} l_{gr})], \tag{5.8}$$

where, l_{0r} is the optical path length of the reference arm for the center wavelength; l_{gr} is the group delay in the reference arm. The two reference Jones vectors are:

$$\begin{aligned}\begin{bmatrix} E_{rH1} \\ E_{rV1} \end{bmatrix} &= \mathbf{J}_{1r}\begin{bmatrix} |A_{iH1}| \\ |A_{iV1}|\exp(i\phi_{HV1}) \end{bmatrix}\exp[-i\omega_1 t + \phi_{01}] \\ &= \frac{i\sqrt{2}}{2}\begin{bmatrix} |A_{iH1}| + |A_{iV1}|\exp(i\phi_{HV1}) \\ |A_{iH1}| - |A_{iV1}|\exp(i\phi_{HV1}) \end{bmatrix}\exp[-i\omega_1 t + i(2\bar{k}_1 l_{0r} + 2k_1^{'} l_{gr}) + \phi_{01}]\end{aligned} \tag{5.9}$$

$$\begin{bmatrix} E_{rH2} \\ E_{rV2} \end{bmatrix} = \mathbf{J}_{2r} \begin{bmatrix} |A_{iH2}| \\ |A_{iV2}|\exp(i\phi_{HV2}) \end{bmatrix} \exp[-i\omega_2 t + \phi_{02}]$$

$$= \frac{i\sqrt{2}}{2} \begin{bmatrix} |A_{iH2}| + |A_{iV2}|\exp(i\phi_{HV2}) \\ |A_{iH2}| - |A_{iV2}|\exp(i\phi_{HV2}) \end{bmatrix} \exp[-i\omega_2 t + i(2\bar{k}_2 l_{0r} + 2k_2' l_{gr}) + \phi_{02}] \qquad 5.10$$

By using the same algorithm as in Eq. 1.3, the interference signals can be expressed as:

$$I_{H1} \propto \sqrt{2}\cos\theta_1 \cos\theta_{r1}\sqrt{R_s R_r} P_0 F_1(\Delta l_{gH}) \cos[2\bar{k}_1 \Delta l_0 + \alpha_1(\Delta l_{gH}) + \Theta_{H1} - \eta_{H1} - \pi/2],$$

$$I_{V1} \propto \sqrt{2}\sin\theta_1 \sin\theta_{r1}\sqrt{R_s R_r} P_0 F_1(\Delta l_{gV}) \cos[2\bar{k}_1 \Delta l_0 + \alpha_1(\Delta l_{gV}) + \Theta_{V1} - \eta_{V1} - \pi/2],$$

$$I_{H2} \propto \sqrt{2}\cos\theta_2 \cos\theta_{r2}\sqrt{R_s R_r} P_0 F_2(\Delta l_{gH}) \cos[2\bar{k}_2 \Delta l_0 + \alpha_2(\Delta l_{gH}) + \Theta_{H2} - \eta_{H2} - \pi/2], \qquad 5.11$$

$$I_{V2} \propto \sqrt{2}\sin\theta_2 \sin\theta_{r2}\sqrt{R_s R_r} P_0 F_2(\Delta l_{gV}) \cos[2\bar{k}_2 \Delta l_0 + \alpha_2(\Delta l_{gV}) + \Theta_{V2} - \eta_{V2} - \pi/2],$$

where F_1 and F_2 are the amplitudes of the inverse Fourier transformation of the power spectra of light sources 1 and 2, respectively; θ_1 and θ_2 are the auxiliary angles for the detected output polarization states for light sources 1 and 2, respectively; θ_{r1} and θ_{r2} are the auxiliary angles for the reference polarization states for light sources 1 and 2, respectively; Θ_{H1}, Θ_{V1}, Θ_{H2}, and Θ_{V2} are the phases of

$J_{11}|A_{iH1}| + J_{12}|A_{iV1}|\exp(i\phi_{HV1})$,

$J_{21}|A_{iH1}| + J_{22}|A_{iV1}|\exp(i\phi_{HV1})$,

$J_{11}|A_{iH2}| + J_{12}|A_{iV2}|\exp(i\phi_{HV2})$, and

$J_{21}|A_{iH2}| + J_{22}|A_{iV2}|\exp(i\phi_{HV2})$,

respectively, which are the phases need to be calculated; η_{H1}, η_{V1}, η_{H2}, and η_{V2} are the phases of

$|A_{iH1}|+|A_{iV1}|\exp(i\phi_{HV1})$,

$|A_{iH1}|-|A_{iV1}|\exp(i\phi_{HV1})$,

$|A_{iH2}|+|A_{iV2}|\exp(i\phi_{HV2})$, and

$|A_{iH2}|-|A_{iV2}|\exp(i\phi_{HV2})$,

respectively, which are known parameters. The phases α_1 and α_2 depend on the power spectrum of the light source 1 and light source 2, respectively. When the power spectra of the two light sources are symmetric, we have

$$\alpha_1 = 0\text{, and } \alpha_2 = 0\,. \qquad 5.12$$

When the power spectra of the two light sources are not identical, there is an arbitrary phase difference between the two measured Jones vectors corresponding to the two incident polarization states. This arbitrary phase difference must be eliminated in order to calculate the roundtrip Jones matrix of the sample arm ($\mathbf{J}_T$).

For OCT signals based on single-backscattered photons, the incident Jones vector $\mathbf{E}_i$ to the sample arm is transformed to the detected Jones vector $\mathbf{E}_d$ by

$$\begin{aligned}\mathbf{E}_d \exp(-i\beta_j) &= \begin{bmatrix} E_{dH} \\ E_{dV} \end{bmatrix} \exp(-i\beta_j) \\ &= \mathbf{E}_o \\ &= \begin{bmatrix} E_{OH} \\ E_{OV} \end{bmatrix} \\ &= \mathbf{J}_{NBS}\mathbf{J}_{QB}\mathbf{J}_{SB}\mathbf{J}_{M}\mathbf{J}_{SI}\mathbf{J}_{QI}\mathbf{E}_i \\ &= \mathbf{J}_{NBS}\mathbf{J}_{QB}\mathbf{J}\mathbf{J}_{QI}\mathbf{E}_i = \mathbf{J}_T\mathbf{E}_i\end{aligned} \qquad 5.13$$

where $j = 1, 2$,

$$\beta_1 = 2k_1\Delta l_0 + \alpha_1,$$

$$\beta_2 = 2k_2\Delta l_0 + \alpha_2;$$

$\mathbf{J}_{QI}$ and $\mathbf{J}_{QB}$ are the Jones matrices of the λ/4 plate for the incident and the backscattered light, respectively; $\mathbf{J}_{SI}$ and $\mathbf{J}_{SB}$ are the Jones matrices of the sample for the incident and backscattered light, respectively; $\mathbf{J}_M$ is the Jones matrix of the single backscatterer—the same as the one for a mirror; $\mathbf{J}_{NBS}$ is the Jones matrix of the reflecting surface of the non-polarizing beam splitter; **J** is the combined round-trip Jones matrix of the scattering medium; $\mathbf{J}_T$ is the overall round-trip Jones matrix.

In Eq. 5.13, $\mathbf{E}_d$ is constructed for each light source from the measured horizontal and vertical components of the OCT signal. Upon acquiring the output Jones vectors and knowing the input Jones vectors, the overall round-trip Jones matrix $\mathbf{J}_T$ can be calculated. The Jones matrix **J** of the sample can be extracted from $\mathbf{J}_T$ by eliminating the effect of the Jones matrices of the quarter-wave plate, the mirror and the beam splitter. As a necessary condition, the two light sources must be independent of each other.

In the commonly used convention, $\mathbf{J}_M$ transforms the polarization state of the forward light expressed in the forward coordinate system into the polarization state expressed in the backward coordinate system. Similarly, $\mathbf{J}_{NBS}$ transforms the polarization state of the backward light into the polarization state expressed in the detection coordinate system. However, we express in this work the polarization states of both the forward and backward light in the forward coordinate system. In this convention, $\mathbf{J}_M$ and $\mathbf{J}_{NBS}$ are unitary:

$$\mathbf{J}_M = \mathbf{J}_{NBS} = \begin{bmatrix} 1 & 0 \\ 0 & 1 \end{bmatrix}$$

In each A-scan, the optical paths for the forward and backward light are the same and therefore, the Jones' reversibility theorem can be applied.[75] The Jones reversibility theorem indicates that the Jones matrices $\mathbf{J}_{BWD}$ and $\mathbf{J}_{FWD}$ of an ordinary optical element for the backward and forward light propagations have the following relationship if the same coordinate system is used for the Jones vectors:

$$\mathbf{J}_{BWD} = \mathbf{J}_{FWD}^T. \qquad 5.14$$

Therefore, we have the following relationships:

$$\mathbf{J}_{SB} = \mathbf{J}_{SI}^T, \mathbf{J}_{QB} = \mathbf{J}_{QI}^T = \frac{1}{\sqrt{2}} \begin{bmatrix} 1 & i \\ i & 1 \end{bmatrix},$$

$$\begin{aligned} \mathbf{J} = \mathbf{J}_{SB}\mathbf{J}_M\mathbf{J}_{SI} &= \mathbf{J}_{SI}^T\mathbf{J}_{SI} = \mathbf{J}^T, \\ \mathbf{J}_T = \mathbf{J}_{NBS}\mathbf{J}_{QB}\mathbf{J}\mathbf{J}_{QI} &= \mathbf{J}_{QI}^T\mathbf{J}\mathbf{J}_{QI} = \mathbf{J}_T^T. \end{aligned} \qquad 5.15$$

In other words, matrices $\mathbf{J}$ and $\mathbf{J}_T$ are transpose symmetric. This property of transpose symmetry is important for eliminating the arbitrary phase difference between the two light sources. Because of this symmetry, the number of independent parameters in the Jones matrix is further reduced from seven to five.

As presented by Yao and Wang using Monte Carlo simulation,[76] the light backscattered from the sample can be divided into two parts: Class *I* and Class *II*. Class *I* light provides a useful signal, which is scattered by the target layer in a sample and the path-length difference of which from the reference light is within the coherence length of the light source. Class *II* light is the part scattered from the rest of the medium, whose path-length difference from the reference light is also within the coherence length of the light source. Class *II* light contributes to the background noise of the OCT signal. The weight of Class *II* light in the detected OCT signal increases with depth and will exceed that of the Class *I* signal beyond some critical depth. The increase of the weight of the Class *II* light deteriorates the resolution and signal-to-noise ratio and thus limits the effective imaging depth. The Class *I* signal also contains multiply scattered photons, but owing to the requirement of matching the optical path-lengths, these multiple scattering events must be small-angle scattering.

For the multiply scattered photons, Eq. 5.13 still holds if the probabilities for photons to travel along the same round-trip path but in opposite directions are equal, which is a valid assumption when the source and detector have reciprocal characteristics. Because these photons are coherent, the round-trip Jones matrix of the sample **J** is the sum of the Jones matrices of all the possible round-trip paths; and for each possible path—for example, the *k*-th path—the round-trip Jones matrix is the sum of the Jones matrices for the two opposite directions [$\mathbf{J}i(k)$and $\mathbf{J}r(k)$]. Consequently, we have

$$\mathbf{J} = \sum_k [\mathbf{J}_i(k) + \mathbf{J}_r(k)] = \sum_k \{\mathbf{J}_i(k) + [\mathbf{J}_i(k)]^T\} = \mathbf{J}^T . \tag{5.16}$$

In other words, **J** as well as $\mathbf{J}_T$ still possesses the transpose symmetry even if multiple scattering occurs as long as the source and the detector meet the condition.

After calculation, Eq. 5.13 can be expressed as

$$\begin{aligned} \begin{bmatrix} E_{oH} \\ E_{oV} \end{bmatrix} &= \begin{bmatrix} \frac{i}{2}(J_{11} - 2iJ_{12} - J_{22}) & \frac{1}{2}(J_{11} + J_{22}) \\ \frac{1}{2}(J_{11} + J_{22}) & \frac{i}{2}(-J_{11} - 2iJ_{12} + J_{22}) \end{bmatrix} \times \begin{bmatrix} E_{iH} \\ E_{iV} \end{bmatrix} . \\ &= \begin{bmatrix} J_{T11} & J_{T12} \\ J_{T12} & J_{T22} \end{bmatrix} \times \begin{bmatrix} E_{iH} \\ E_{iV} \end{bmatrix} \end{aligned} \tag{5.17}$$

where J_{ij} (i, j = 1, 2) are the elements of **J**. For two light sources of independent polarization states, Eq. 5.17 can be rearranged as:

$$\begin{bmatrix} e^{-i\beta_1} E_{dH1} & e^{-i\beta_2} E_{dH2} \\ e^{-i\beta_1} E_{dV1} & e^{-i\beta_2} E_{dV2} \end{bmatrix} = \begin{bmatrix} J_{T11} & J_{T12} \\ J_{T12} & J_{T22} \end{bmatrix} \times \begin{bmatrix} E_{iH1} & E_{iH2} \\ E_{iV1} & E_{iV2} \end{bmatrix} . \tag{5.18}$$

where E_{dH1} and E_{dH2}, E_{dV1} and E_{dV2} are the measured elements of the Jones vectors of source 1 and source 2, respectively. $\mathbf{J}_T$ can be calculated from Eq. 5.18 as

$$\begin{aligned} \begin{bmatrix} J_{T11} & J_{T12} \\ J_{T12} & J_{T22} \end{bmatrix} &= \begin{bmatrix} e^{-i\beta_1} E_{dH1} & e^{-i\beta_2} E_{dH2} \\ e^{-i\beta_1} E_{dV1} & e^{-i\beta_2} E_{dV2} \end{bmatrix} \times \begin{bmatrix} E_{iH1} & E_{iH2} \\ E_{iV1} & E_{iV2} \end{bmatrix}^{-1} \\ &= \frac{1}{D} \begin{bmatrix} e^{-i\beta_1} E_{oH1} & e^{-i\beta_2} E_{oH2} \\ e^{-i\beta_1} E_{oV1} & e^{-i\beta_2} E_{oV2} \end{bmatrix} \times \begin{bmatrix} E_{iV2} & -E_{iH2} \\ -E_{iV1} & E_{iH1} \end{bmatrix} \end{aligned} , \tag{5.19}$$

as long as the determinant

$$D = \begin{vmatrix} E_{iH1} & E_{iH2} \\ E_{iV1} & E_{iV2} \end{vmatrix} \neq 0$$

i.e. the two light sources are not in the same polarization state. The arbitrary phase difference β_j can be eliminated with the transpose symmetry of $\mathbf{J}_T$:

$$e^{i\beta_2}\left(E_{oH1}E_{iH2}+E_{oV1}E_{iV2}\right)=e^{i\beta_1}\left(E_{oV2}E_{iV1}+E_{oH2}E_{iH1}\right). \qquad 5.20$$

Equation 5.20 can be solved when $\left(E_{oH1}E_{iH2}+E_{oV1}E_{iV2}\right)\neq 0$. Once $\mathbf{J}_T$ is found, **J** can then be determined from $\mathbf{J}_T$. Six real parameters of **J** can be calculated, in which one phase is arbitrary and can be subtracted from each element, and eventually five independent parameters are retained.

When $\left(E_{oH1}E_{iH2}+E_{oV1}E_{iV2}\right)=0$, it is impossible to eliminate the arbitrary phase difference by using the transpose symmetry. This situation happens if the sample arm does not alter the polarization states of the two incident beams besides producing a mirror reflection. For example, this situation occurs if (1) a horizontal or vertical incident beam is used, (2) a λ/4 plate is not inserted in the sample arm, and (3) the fast axis of a birefringent sample is horizontal or vertical. The use of the λ/4 plate at a 45° orientation in the sample arm can ameliorate the situation. However, there are still some drawbacks with this configuration. For example, when the round-trip Jones matrix **J** is equivalent to one of a half-wave plate with its fast axis oriented at 45° and thus $\mathbf{J}_T$ is equivalent to a unitary matrix, we will have $\left(E_{oH1}E_{iH2}+E_{oV1}E_{iV2}\right)=0$. To overcome this drawback, we can employ two non-orthogonal incident polarization states: for example, one source is in a horizontal polarization state and the other source is in a 45° polarization state.

The interference signals are band-pass filtered with central frequencies of 4.2 kHz and 4.7 kHz and a bandwidth of 10 Hz—the sum frequencies of the interference signals of source *H* and source *V*, respectively—to extract the interference components of each light source. After eliminating the parameters of the reference beams, the interference components form the imaginary parts of $E_{x,y}(t)$ — the elements of the detected output Jones vectors, whose real parts are obtained through inverse Hilbert transformation:[77,78]

$$\mathrm{Re}\{E_{x,y}(t)\} = \frac{1}{\pi} P\int_{-\infty}^{\infty} \frac{\mathrm{Im}\{E_{x,y}(t)\}}{\tau - t} d\tau \,. \tag{5.21}$$

where *P* stands for the Cauchy principal value of the integral, and *x* and *y* represent the detected polarization state (*H* or *V*) and the source polarization state (*H* or *V*), respectively. Unlike other transforms, the Hilbert transformation does not change the domain. A convenient method of computing the Hilbert transform is by means of the Fourier transformation. If *u(t)* and *v(t)* are a Hilbert pair of functions, i.e.

$$u(t) \overset{H}{\Longleftrightarrow} v(t)$$

and *U(w)* and *V(w)* are the Fourier transforms of *u(t)* and *v(t)*, the following algorithm can be used to calculate the Hilbert transform:[78]

$$\begin{aligned} u(t) &\overset{F}{\Rightarrow} U(w) \Rightarrow V(w) = -i \cdot sgn(w) U(w) \overset{F^{-1}}{\Rightarrow} v(t) \\ v(t) &\overset{F}{\Rightarrow} V(w) \Rightarrow U(w) = i \cdot sgn(w) U(w) \overset{F^{-1}}{\Rightarrow} u(t) \end{aligned} \,. \tag{5.22}$$

where *F* and F^{-1} denote the Fourier and inverse Fourier transformations, respectively; *sgn(w)* is the signum function defined as

$$sgn(w) = \begin{cases} +1 & w > 0 \\ 0 & w = 0 \\ -1 & w < 0 \end{cases}.$$

The real and imaginary parts of each interference component are combined to form the complex components of the output Jones vectors. Upon determining the output Jones vector, when the input Jones vectors are known, the elements of the Jones matrix **J** of the sample can then be calculated.

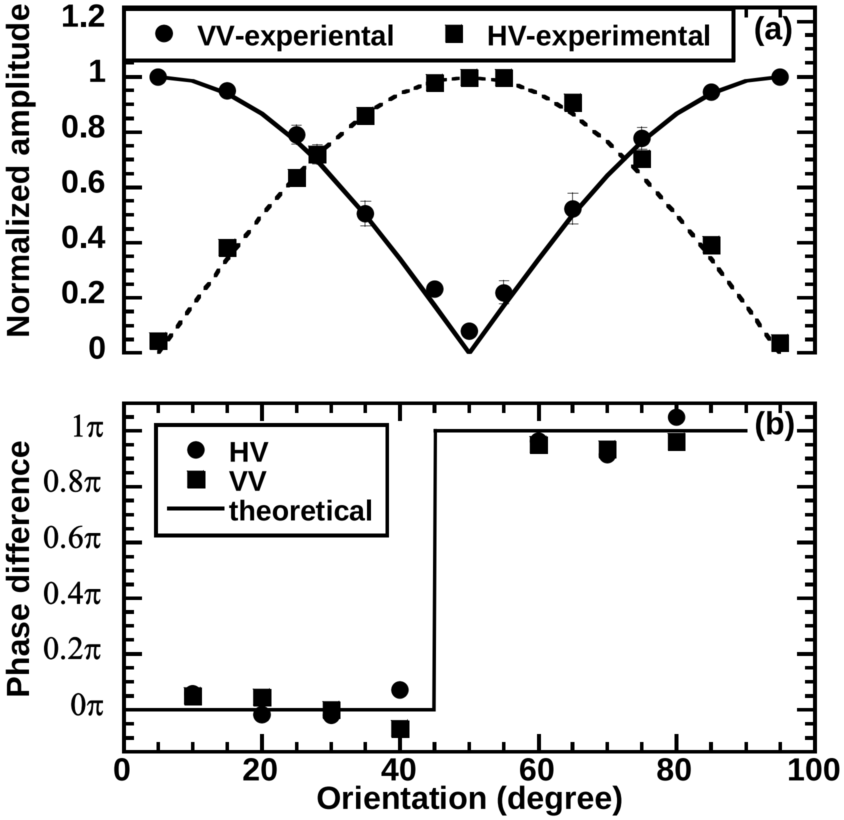

Fig 5.2 (a) Normalized amplitude of the vertical components of the measured Jones vectors of a quarter-wave plate versus the orientation of the fast axis. *HV* is for the horizontally polarized incident light, and *VV* is for the vertically polarized incident light. The lines represent the expected theoretical values. (b) Phase differences between the vertical and the horizontal components of the Jones vectors of the same quarter-wave plate. The standard deviations are smaller than the symbols.

The system was first tested by measuring the matrix of a standard sample—a λ/4 wave-plate at various orientations in combination with a mirror. Figure Fig 5.2(a) shows the amplitude of the vertical components of the measured Jones vector versus the orientation of the wave-plate, where the amplitude of each Jones vector was normalized to unity. Figure Fig 5.2(b) shows the phase differences between the vertical components and the horizontal components of the Jones vectors. The calculated results were averaged over 1000 points centered at the peak of the interference signals, where 1000 points correspond to 10 μm—the resolution of the system. The results show that the measured data agree very well with the theoretical values.

The system was then tested by measuring the Jones matrix of a variable wave plate (5540 Berek polarization compensator, New Focus). The variable wave plate was set to provide around a λ/8 retardation with the fast axis oriented at about –54°. The vertical component of the measured OCT signal for the source with a vertical polarization state is shown in Fig 5.3. The measured mean Jones matrix ($\mathbf{J}_m$) and the corresponding standard deviation matrices for the amplitude ($\mathbf{J}_{\rho\sigma}$) and phase ($\mathbf{J}_{\varphi\sigma}$) are as follows:

$$\begin{aligned}\mathbf{J}_m &= \begin{bmatrix} 1 & 0.333-0.945i \\ 0.333-0.945i & 0.739+0.595i \end{bmatrix} \\ &= \begin{bmatrix} 1 & 1.002\exp(-1.232i) \\ 1.002\exp(-1.232i) & 0.949\exp(0.6779i) \end{bmatrix},\end{aligned}$$

$$\mathbf{J}_{\rho\sigma} = \begin{bmatrix} 0 & 0.061 \\ 0.061 & 0.10 \end{bmatrix}, \ \mathbf{J}_{\varphi\sigma} = \begin{bmatrix} 0 & 0.06 \\ 0.06 & 0.10 \end{bmatrix}.$$

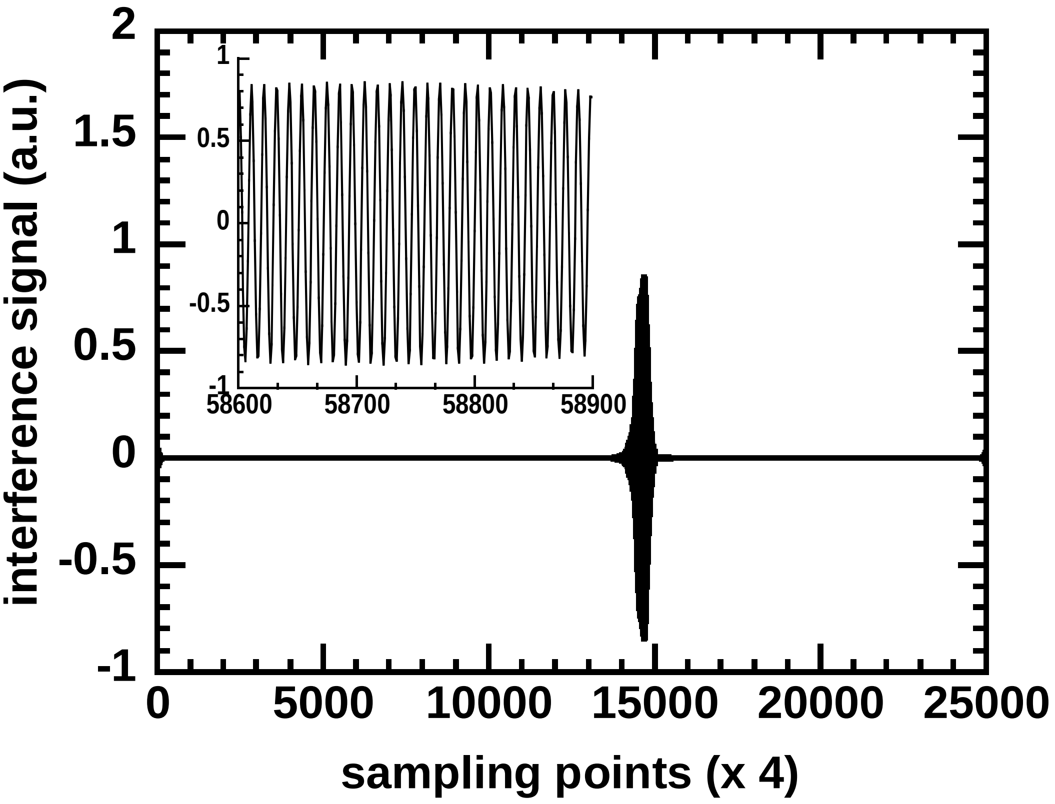

Fig 5.3 Measured vertical component of the OCT signal of the calibrating variable wave plate for the light source with a vertical polarization state. The inset is the plot of 300 data points of the interference signal around the peak.

The results were averaged over 1000 points centered at the peak of the interference signals. The mean and standard deviation were calculated from 100 measurements. The theoretically predicted round-trip Jones matrix ($\mathbf{J}_{P1}$) of a λ/8 plate with orientation of –54° and the relative amplitude and phase differences of the measured matrix from the theoretical matrix ($\mathbf{J}_{\rho d1}$ and $\mathbf{J}_{\varphi d1}$) are

$$\mathbf{J}_{P1} = \begin{bmatrix} 1 & 0.267-0.870i \\ 0.267-0.870i & 0.828+0.561i \end{bmatrix}$$
$$= \begin{bmatrix} 1 & 0.91\exp(-1.273i) \\ 0.91\exp(-1.273i) & 1.0\exp(0.5955i) \end{bmatrix},$$

$$\mathbf{J}_{\rho d1} = \begin{bmatrix} 0 & 10.1\% \\ 10.1\% & -5.1\% \end{bmatrix},$$

$$\mathbf{J}_{\varphi d1} = \begin{bmatrix} 0 & 3.2\% \\ 3.2\% & 13.8\% \end{bmatrix}.$$

The error comes mainly from the inaccurate setting of the variable wave plate. The actual parameters of the wave plate can be calculated from the measured Jones matrix. The retardation and the orientation of the wave-plate were calculated to be 48.95° and –53.93°. The theoretically fitted round-trip Jones matrix of a wave-plate with the calculated retardation and orientation values ($\mathbf{J}P2$) and the relative amplitude and phase differences of the measured matrix from this theoretically fitted matrix ($\mathbf{J}_{\rho d2}$ and $\mathbf{J}_{\varphi d2}$) are

$$\mathbf{J}_{P2} = \begin{bmatrix} 1 & 0.343-0.972i \\ 0.343-0.972i & 0.779+0.627i \end{bmatrix}$$
$$= \begin{bmatrix} 1 & 1.031\exp(-1.2316i) \\ 1.031\exp(-1.2316i) & 1.0\exp(0.6777i) \end{bmatrix},$$

$$\mathbf{J}_{\rho d2} = \begin{bmatrix} 0 & -2.8\% \\ -2.8\% & -5.1\% \end{bmatrix},$$

$$\mathbf{J}_{\varphi d2} = \begin{bmatrix} 0 & 0.03\% \\ 0.03\% & 0.03\% \end{bmatrix}.$$

5.4 Experimental Results and Analysis

The system was then applied to image soft tissue—a piece of porcine tendon. The tendon was mounted in a cuvette filled with saline solution. The sample was transversely scanned with a step size of 5 µm, and multiple A-scan images were taken. The digitized interference signals were first band-pass filtered with software and Hilbert transformed to extract the analytical signals of each polarization component. For each A scan, the pixels were formed by averaging the calculated elements of the Jones matrix over segments of 1000 points. Two-dimensional (2D) images were formed from these A-scan images and then median filtered. The final 2D Mueller-matrix images are shown in Fig 5.4.

Clear band structures can be seen in some of the images, especially in M_{13}, M_{22}, M_{23}, M_{31}, M_{32}, and M_{33}. The period of the band structure is ~0.13 mm. There is no such band structure present in the M_{00} image, which is the image based on the intensity of the back-scattered light. We believe that the band structure is generated by the birefringence of the collagen fibers in the porcine tendon. The band structure distributes quite uniformly in the measured region; therefore, the birefringence is also uniform in the measured area.

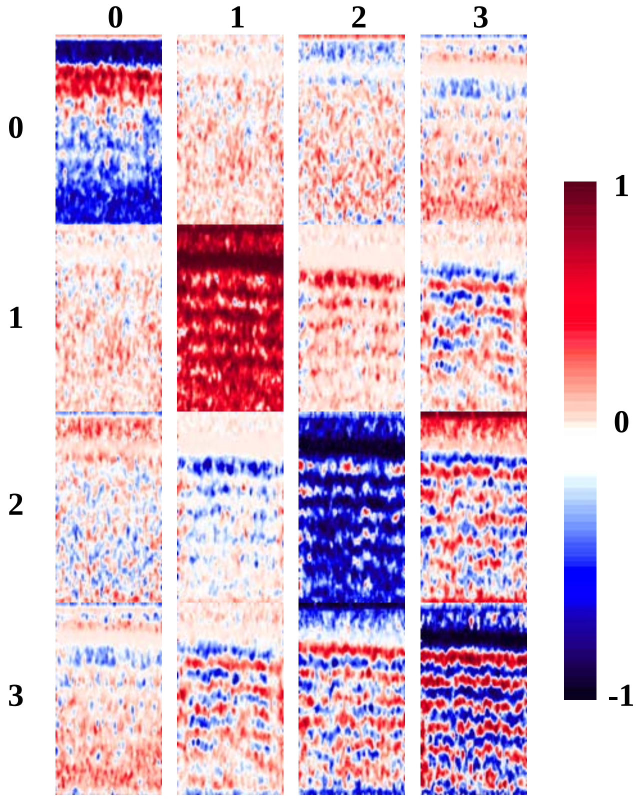

Fig 5.4 2D Mueller-matrix images of a piece of porcine tendon. Each image except M_{00} is pixel-wise normalized with the M_{00} element and shares the same color table. The size of each image is 0.5 mm × 1 mm.

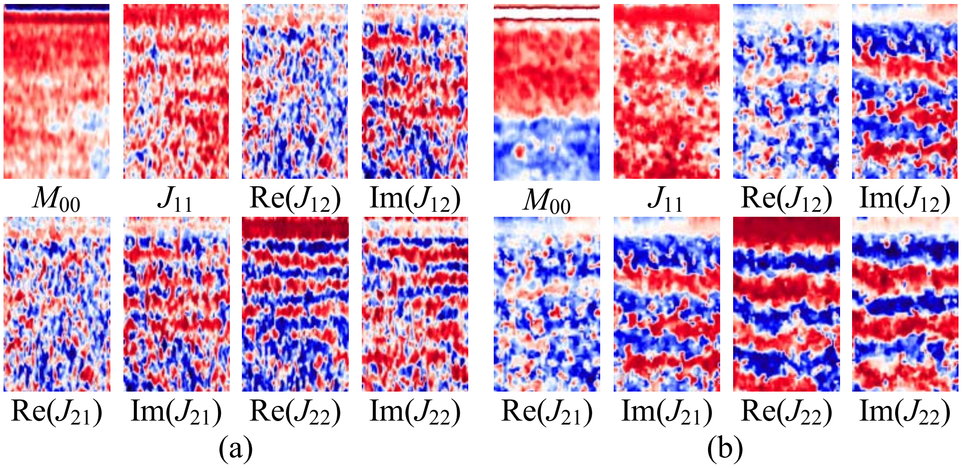

(a) (b)

Fig 5.5 (a) M_{00} and 2D Jones-matrix images of a piece of normal porcine tendon. (b) M_{00} and 2D Jones-matrix images of the piece of porcine tendon heated for 20 seconds at 90^{o}.

The 2D Jones-matrix images of another piece of porcine tendon are shown in Fig 5.5. The amplitudes of the elements of the Jones matrix were pixel-wise normalized with $\sqrt{M_{00}}$ and the phases were pixel-wise subtracted by the phases of J_{11}. M_{00} represents the intensity transformation from the input light into the output light and

$$M_{00} = \frac{1}{2}\left(\left|J_{11}\right|^2 + \left|J_{12}\right|^2 + \left|J_{21}\right|^2 + \left|J_{22}\right|^2\right). \qquad 5.23$$

After the test, the sample was thermally treated to test the change of polarization properties of biological tissue due to thermal damage. The sample was heated for about 20 seconds by touching it with a piece of metal, which was partially immersed in 90°C hot water; the piece of metal was used for the convenience of heating the sample in a specific area. The Jones-matrix images shown in Fig 5.5(b) clearly show that the period of the band structure increased with the thermal treatment, which we believe is directly caused by the reduction of birefringence in the sample. This observation, birefringence loss caused by thermal damage, is consistent with the experimental result of another group.[79]

Usually the parameters characterizing the polarization properties of a sample are contained implicitly in its Jones and Mueller matrices. Explicit polarization parameters of a sample, such as diattenuation, birefringence, and orientation of fast axis need to be extracted from the measured Jones or Mueller matrices through decomposition. For a non-depolarizing sample, the decomposition of its Jones matrix is equivalent to the decomposition of its Mueller matrix.

A Jones matrix can be decomposed by polar decomposition:[73,80]

$$\mathbf{J} = \mathbf{J}_P \mathbf{J}_R . \qquad 5.24$$

where $\mathbf{J}_P$ is the Jones matrix of a diattenuator (partial polarizer) and $\mathbf{J}_R$ is the Jones matrix of an elliptical retarder. In biological tissues, it is reasonable to believe that the orientations of the diattenuator and the retarder are the same because the orientation of both the diattenuator and the retarder are directly related to the orientation of the tissue fibers. In this case, $\mathbf{J}$ is homogenous in the polarization sense [80] and the order of $\mathbf{J}_P$ and $\mathbf{J}_R$ in Eq. 5.24 is reversible.

Because the effect of non-Faraday circular birefringence is cancelled in the round-trip OCT signals and there is no Faraday circular birefringence exists without a magnetic field applied to the sample, only linear birefringence exists in the Jones matrix $\mathbf{J}$. We extracted polarization parameters from a piece of porcine tendon set at various orientations. The rotation axis of the sample is collinear with the optical axis of the incident light. The measurements were made at five different orientations with an interval of 10°. For a Jones matrix that contains linear birefringence and linear or circular diattenuation, the following relationships can be derived:

$$\begin{aligned}&\mathrm{Re}(J_{11})\mathrm{Im}(J_{21})-\mathrm{Im}(J_{11})\mathrm{Re}(J_{21})-\mathrm{Re}(J_{12})\mathrm{Im}(J_{22})+\mathrm{Im}(J_{12})\mathrm{Re}(J_{22})\\&=P(P_q,P_r)\sin(2\theta)\sin(\varphi)\\&=M_{31}\end{aligned}$$

$$\begin{aligned}&\mathrm{Re}(J_{11})\mathrm{Im}(J_{22})-\mathrm{Im}(J_{11})\mathrm{Re}(J_{22})-\mathrm{Re}(J_{21})\mathrm{Im}(J_{12})+\mathrm{Im}(J_{21})\mathrm{Re}(J_{12})\\&=-P(P_q,P_r)\cos(2\theta)\sin(\varphi)\\&=M_{32}\end{aligned} \tag{5.25}$$

$$M_{00}=\frac{1}{2}\left(P_q^2+P_r^2\right)$$

where P is a function of P_q and P_r. To increase the signal-to-noise ratio, every 20 adjacent A-scans of M_{31} and M_{32} were averaged and the data corresponding to a physical depth of 0.4 mm from the surface (optical depth divided by the refractive index of the sample, which was assumed to be 1.4) were fitted for the polar decomposition.

The averaged raw data and the fitted curves for the different orientations are shown in Fig 5.6. In the figure the evolution of M_{31} and M_{32} with the orientations can be clearly seen. The calculated birefringence from the fitted data is $(4.2 \pm 0.3) \times 10^{-3}$, which is comparable with the previously reported value of $(3.7\pm0.4) \times 10^{-3}$ for bovine tendon.[17] The calculated birefringence of the thermally treated porcine tendon in Fig 5.5(b) is (2.24±0.07) × 10–3, which is about half of the normal value. After subtracting an offset, the calculated angles of the fast axis are shown in Fig 5.7. The small angular offset is due to the discrepancy between the actual and the visually observed fiber orientations. The results are very good considering that the tendon was slightly deformed when it was mounted in the cuvette and the rotation axis of the sample may not have been exactly collinear with the optical axis.

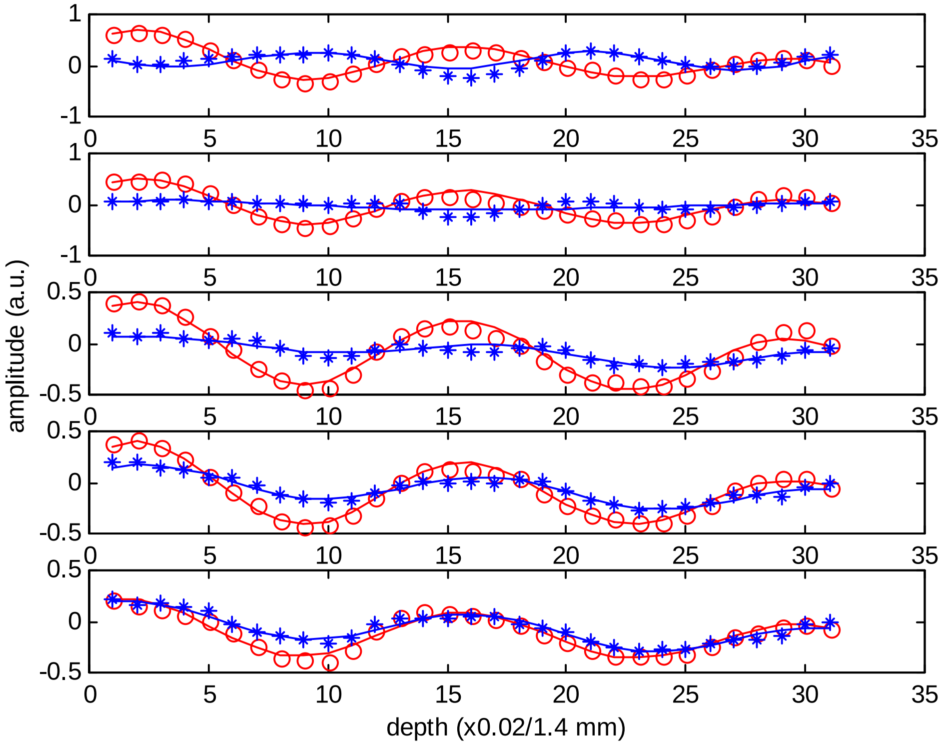

Fig 5.6 The averaged raw data of M_{31} ("*") and M_{32} ("o"), as in Eq. (12), of a piece of porcine tendon versus penetration depth and the fitted curve ("—") for different orientations. From the top to the bottom the interval of variation of the orientation is –10°.

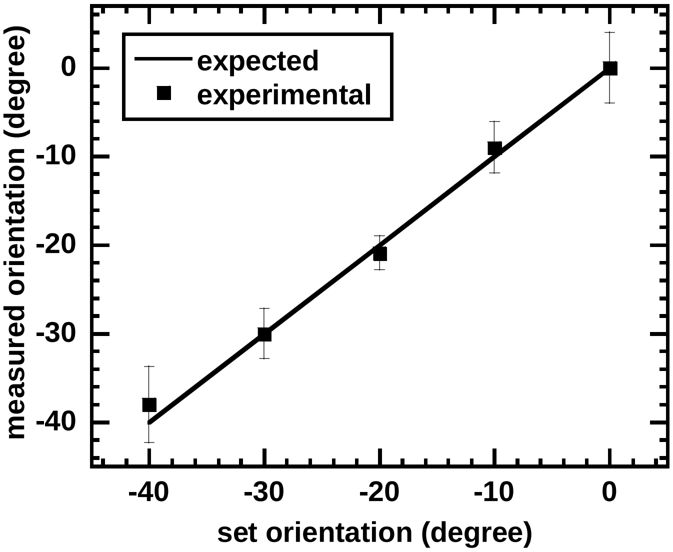

Fig 5.7 The calculated angle and the standard error of the fast axis for different orientations of the sample in Fig 5.5.

The diattenuation is defined as

$$D = \left(P_q^2 - P_r^2\right) / \left(P_q^2 + P_r^2\right) = \sqrt{M_{01}^2 + M_{02}^2 + M_{03}^2} \,/\, M_{00} \,. \qquad 5.26$$

where M_{01}, M_{02} and M_{03} are the elements of the corresponding Mueller matrix and can be calculated with Eq.3.15. The calculated D was averaged over all the orientations and linearly fitted over a depth of 0.3 mm. The fitted D versus the round-trip physical path length increases with a slope of 0.26/mm and reaches 0.075±0.024 at the depth of 0.3 mm after subtracting an offset at the surface. The magnitude of birefringence and diattenuation are related to the density and property of collagen fibers, whereas the orientation of the fast axis indicates the orientation of the collagen fibers.

5.5 Conclusion

In summary, we developed a novel double-source double-detector polarization-sensitive OCT imaging technique. This technique enables the acquisition of a 2D tomographic Jones matrix, which can be converted into a Mueller matrix. The depth-resolved Jones matrix of a sample can be determined with a single scan; as a result, this technique is capable of imaging either hard or soft biological tissues. In addition, the Jones matrix can be decomposed to extract important information on the optical polarization properties of a sample, such as birefringence, orientation of the fast axis, and diattenuation. In our study, the Jones-matrix images of the thermally treated porcine tendon clearly showed changes in birefringence due to thermal damage. This technique has the potential to provide a new contrast mechanism for imaging biological tissues.

6 CONTRAST MECHANISMS IN MUELLER-MATRIX OCT

6.1 Introduction

The contrast of an OCT image is provided by the optical properties of a sample that modify the parameters of the light field including the amplitude and the polarization state. The parameters characterizing the structurally isotropic or averaged optical properties[81] of a sample include the absorption coefficient (μ_a), scattering coefficient (μ_s), scattering anisotropy (g), and refractive index (n); and the parameters characterizing the polarization properties of a sample include birefringence (amplitude δn, orientation, and ellipticity) and diattenuation (amplitude D, orientation, and ellipticity), which provide polarization-based contrast in polarization-sensitive OCT (PS-OCT).

The polarization properties of a non-depolarizing sample can be completely characterized by either a Mueller matrix or a Jones matrix and the two matrices are equivalent.[82] Therefore, to provide comprehensive information about polarization of a sample, the most general PS-OCT should measure the Jones or Mueller matrix. Upon acquisition of the Jones or Mueller matrix, any polarization parameters can be extracted. We define Mueller-matrix OCT as PS-OCT that can measure the Mueller or Jones matrix of a sample. Therefore, Mueller-matrix OCT is the most general form of PS-OCT.

In this section we investigate the various contrast mechanisms provided by Mueller-matrix OCT. The properties of the roundtrip Jones matrix are analyzed for conditions with and without diattenuation in a sample. The analyses indicate that when diattenuation is negligible, one incident polarization state is adequate for the acquisition of the Jones matrix. When diattenuation cannot be neglected, two incident polarization states are necessary and the transpose symmetric property of the roundtrip Jones matrix (first discovered by our group [20]) offers a critical condition for the calculation of the Jones matrix correctly. Experimental results with biological samples are presented.

6.2 Polarization-based Contrast

Diattenuation is a description of the dependence of transmittance on the incident polarization states and is defined as

$$D = (P_q^2 - P_r^2)/(P_q^2 + P_r^2), \qquad 6.1$$

where P_q and P_r represent the amplitude transmittances for the two orthogonal eigen-polarizations of a polarization element. Therefore, diattenuation provides anisotropic amplitude-based contrast, as it incurs no phase retardation. Birefringence is a description of the anisotropic dependence of the phase velocity of light in a sample on the incident polarization states. The phase retardation of a light field, induced by the local birefringence between the two orthogonal eigen-polarizations, can be expressed as $d\varphi = \overline{k}\delta n(L_s^{'})dL_s^{'}$, where $\overline{k}$ is the wave vector corresponding to the central wavelength of the incident light in vacuum; $L_s^{'}$ is the physical path length that the light travels in the birefringent medium; $\delta n(L_s^{'})$ is the local birefringence; and $dL_s^{'}$ is the local physical path length. The phase retardation provides a unique phase-based polarization contrast mechanism reflecting the amplitude of birefringence, which exists in a variety of biological components such as collagen, keratin, myelin and elastic fibers. Because highly birefringent collagen is a predominant structural component in most biological tissues, this intrinsic contrast mechanism is prevalent in the biomedical applications of Mueller OCT. In addition, many degenerative processes of biological tissues alter birefringence and should, thus, be detectable by Mueller-matrix OCT.

In a PS-OCT system, the detected variation of the polarization state of the scattered light in reference to the incident light is affected by the roundtrip polarization effect of a sample, which can be characterized with a roundtrip Jones matrix ($\mathbf{J}_2$). We will use subscripts 1 and 2 to describe the one-way and round-trip parameters, respectively. Upon acquisition of the roundtrip Jones matrix, the round-trip retardation (φ_2) and diattenuation (D_2) for each pixel can be calculated with the following formulae, respectively:[83]

$$\varphi_2 = 2\cos^{-1}\left\{ \frac{1}{2} \frac{\left| \operatorname{tr} \mathbf{J}_2 + [\det \mathbf{J}_2 / |\det \mathbf{J}_2|] \operatorname{tr} \mathbf{J}_2^* \right|}{[\operatorname{tr}(\mathbf{J}_2^* \mathbf{J}_2) + 2|\det \mathbf{J}_2|]^{1/2}} \right\}, \qquad 6.2$$

$$D_2 = \left\{ 1 - \frac{4|\det \mathbf{J}_2|^2}{[\operatorname{tr}(\mathbf{J}_2^* \mathbf{J}_2)]^2} \right\}^{1/2}, \qquad 6.3$$

where $*$, tr and det represent the Hermitian (transpose conjugate), trace and determinant of the matrix, respectively. The fast eigenvector of $\mathbf{J}_2$ at each pixel of the sample, $\mathbf{E}_2 = \begin{bmatrix} E_{2h} \\ E_{2v} \end{bmatrix}$, can be calculated through standard algorithms. The orientation of the fast axis can thus be calculated as

$$\theta_2 = arc\tan[\frac{E_{2v}}{E_{2h}}], \tag{6.4}$$

6.3 Calculation of the Roundtrip Jones Matrix

The roundtrip Jones matrix $\mathbf{J}_2$ can be expressed with the one-way Jones matrix ($\mathbf{J}_1$), according to Eq. 5.14, as

$$\mathbf{J}_2 = \mathbf{J}_1^T \mathbf{J}_1 . \tag{6.5}$$

A polarization element is called homogeneous when the two eigenvectors of its Jones matrix are orthogonal. A retarder is called elliptical when its eigen-polarizations are elliptical polarization states. A linear retarder is a special case where the eigen-polarizations are linear and a Faraday rotator is another special case where the eigen-polarizations are circular. We can prove that when two or more linear retarders are cascaded, the overall retarder is generally elliptical unless their axes are aligned. Except in some special samples, the orientations of the birefringent fibers in biological samples, take skin for example, are not collinear, and as a result, $\mathbf{J}_1$ generally represents a homogeneous elliptical retarder if diattenuation is negligible in the sample.

When diattenuation is negligible in a sample, according to Eq. 3.14, $\mathbf{J}_1$ can be expressed as

$$\begin{aligned} \mathbf{J}_1(\varphi_1, \theta_1, \delta_1) &= \begin{bmatrix} \cos(\varphi_1/2) + i\sin(\varphi_1/2)\cos 2\theta_1 & i\sin(\varphi_1/2)\sin 2\theta_1 \exp(-i\delta_1) \\ i\sin(\varphi_1/2)\sin 2\theta_1 \exp(i\delta_1) & \cos(\varphi_1/2) - i\sin(\varphi_1/2)\cos 2\theta_1 \end{bmatrix} \\ &= \begin{bmatrix} J_1(1,1) & J_1(1,2) \\ -J_1(1,2)^* & J_1(1,1)^* \end{bmatrix}, \end{aligned} \tag{6.6}$$

The fast and slow eigen-vectors are $\begin{bmatrix} \cos\theta_1 \\ \sin\theta_1 \exp(i\delta_1) \end{bmatrix}$ and $\begin{bmatrix} -\sin\theta_1 \exp(-i\delta_1) \\ \cos\theta_1 \end{bmatrix}$, respectively, where θ_1 is an auxiliary angle and δ_1 represents the phase difference between the two components of the fast eigen-vector. φ_1 is the phase difference between the two eigen-values (the retardation). The azimuth (α_1) of the major axis of its fast eigen-polarization can be expressed as $\tan(2\alpha_1) = \tan(2\theta_1)\cos\delta_1$. If $\delta_1 = 0$, $\mathbf{J}_1$ is transpose symmetric, representing a linear retarder, and $\alpha_1 = \theta_1$ represents the orientation of the fast axis.

From section 5.3, we know that $\mathbf{J}_2$ is transpose symmetric. As a result, $\mathbf{J}_2$ represents a linear retarder and we can thus conclude that the roundtrip transformation effect of an elliptical retarder is equivalent to the one-way transformation of a linear retarder. This conclusion is the foundation of conventional PS-OCT, where a sample is treated as a linear retarder. Since only two parameters are needed to characterize a linear retarder, the number of parameters needed to characterize the round-trip polarization properties of a sample is reduced to two. This conclusion allows the acquisition of this type of round-trip Jones matrix with only one incident polarization state. For an incident polarization state $\mathbf{E}_i = \begin{bmatrix} E_{ih} \\ E_{iv} \end{bmatrix}$, the output polarization state $\mathbf{E}_o = \begin{bmatrix} E_{oh} \\ E_{ov} \end{bmatrix}$ detected by PS-OCT can be expressed as

$$\begin{bmatrix} E_{oh} \\ E_{ov} \end{bmatrix} = \mathbf{J}_2 \begin{bmatrix} E_{ih} \\ E_{iv} \end{bmatrix}, \qquad 6.7$$

Because of the orthonormal transformation property of $\mathbf{J}_2$, the inherent property of a retarder, we also have

$$\begin{bmatrix} E_{ov}^{*} \\ -E_{oh}^{*} \end{bmatrix} = \mathbf{J}_2 \begin{bmatrix} E_{iv}^{*} \\ -E_{ih}^{*} \end{bmatrix}, \qquad 6.8$$

The round-trip Jones matrix can thus be calculated as

$$\mathbf{J}_2 = \begin{bmatrix} E_{oh} & E_{ov}^{*} \\ E_{ov} & -E_{oh}^{*} \end{bmatrix} \begin{bmatrix} E_{ih} & E_{iv}^{*} \\ E_{iv} & -E_{ih}^{*} \end{bmatrix}^{-1}, \qquad 6.9$$

When diattenuation cannot be neglected in a sample, one incident polarization state is not sufficient to acquire its roundtrip Jones matrix because five real parameters [φ_2, θ_2, amplitude transmittances (P_{q2} and P_{r2}), and the orientation of diattenuation (θ_{d2})] are needed to characterize such a system. Therefore, at least two incident polarization states, either applied at the same time or applied sequentially, are required. The transpose symmetry in the roundtrip Jones matrix (first discovered by our group [20], see section 5.3) is critical for eliminating the arbitrary phase difference between the two measured Jones vectors corresponding to the two incident polarization states to yield the correct Jones matrix. This arbitrary phase difference can be caused either by the nonidentity of the power spectra when two light sources are used or by the imperfection of the longitudinal scanning mechanism when the two incident polarization states are applied sequentially. By ignoring the diattenuation effect completely, conventional PS-OCT is not valid for biological samples possessing diattenuation and cannot provide diattenuation contrast.

6.4 Experiment

Our multi-channel Mueller OCT system can acquire the Jones matrix of a sample with a single scan for each one-dimensional depth image (A line image). The Jones matrix can be further transformed into an equivalent Mueller matrix. The Mueller matrix is preferred because its first element, $M_{00,}$ represents the intensity transformation property of a sample and is free of both the effects of the sample polarization and the polarization state of the incident light. Therefore, a Mueller matrix reveals the real morphologic structure as well as the polarization-based features of a sample.

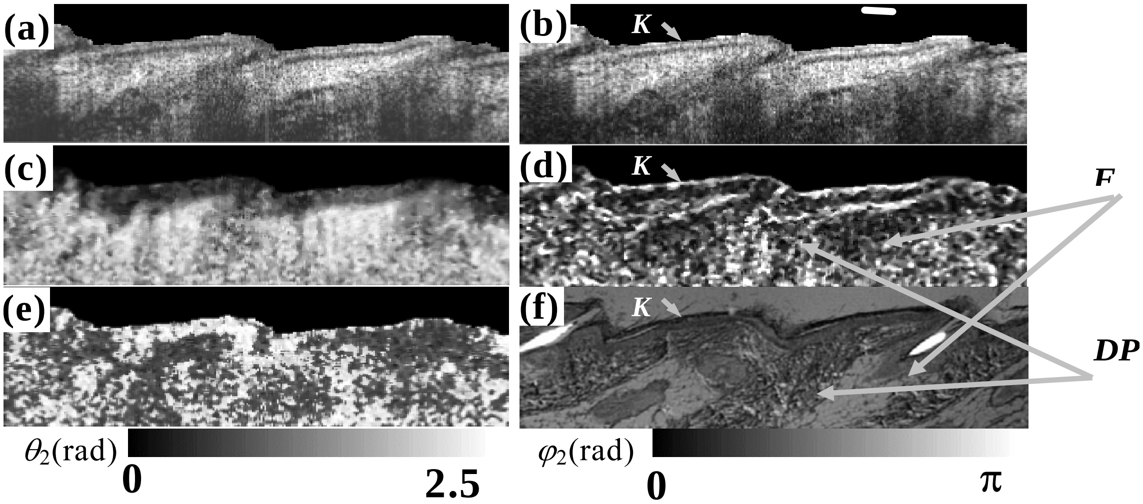

Fig. 6.1 (a) Conventional OCT image (in logarithmic scale), (b) intensity image (M_{00}, in logarithmic scale), (c) retardation image, (d) differential retardation image, (e) image of the orientation of the fast axis, and (f) polarization histologic image of an *in situ* rat tail. The height of each image is 750 μm. The gray scales are for the orientation (θ_2) and retardation (φ_2) images, respectively. The conventional OCT image was obtained with vertical linear polarization states for both the incident and reference beams. *F*: fat; *K*: keratin; *DP*: dermal papilla.

The tail of a rat was imaged *in situ* with Mueller OCT after the skin was shaved and scrubbed with glycerin. The OCT and polarization-histologic images are shown in Fig. 6.1 (a)–(f). There are no significant differences between the M_{00} image [Fig. 6.1 (b)] and the conventional OCT image for this particular sample [Fig. 6.1 (a)], both of which are amplitude-based. The effect of polarization on a conventional OCT image depends on several parameters, for example, the incident polarization state, the value and orientation of the birefringence, and the accumulated phase retardation. When fringes are present in the conventional OCT image, the difference between these two images is dramatic. The intensity and retardation images reveal different characteristics of the sample. The intensity images clearly reveal the boundaries of the structures in the epidermis and only the shallow dermal region. In contrast, the retardation image [Fig. 6.1(c)] reveals the distribution of birefringent components deeper into the dermis. The absolute value of the retardation difference between each pixel and its previous pixel in the same A line is calculated to obtain a differential retardation image [Fig. 6.1(d)]. The birefringent regions (corresponding to the superficial keratin layer and collagen-rich dermal papillae) and non-birefringent regions (corresponding to fat and the living epidermis) are shown more clearly in the differential retardation image than in the raw retardation image. The image of the orientation of the fast axis [Fig. 6.1(e)] revealed structures that we believe to be related to the distribution of the orientation of the birefringent fibers (collagen and keratin). In the figure, we can see that the orientation of the fast axis varies from region to region as also observed in the polarization histology. Although the amplitude- and phase-based polarization signals should have comparable signal-to-noise ratios because they are computed from the same measurements, the contrast-to-noise ratio can be different depending on the availability of the two contrasts in the sample; therefore, the two contrast mechanisms can provide information into different depths.

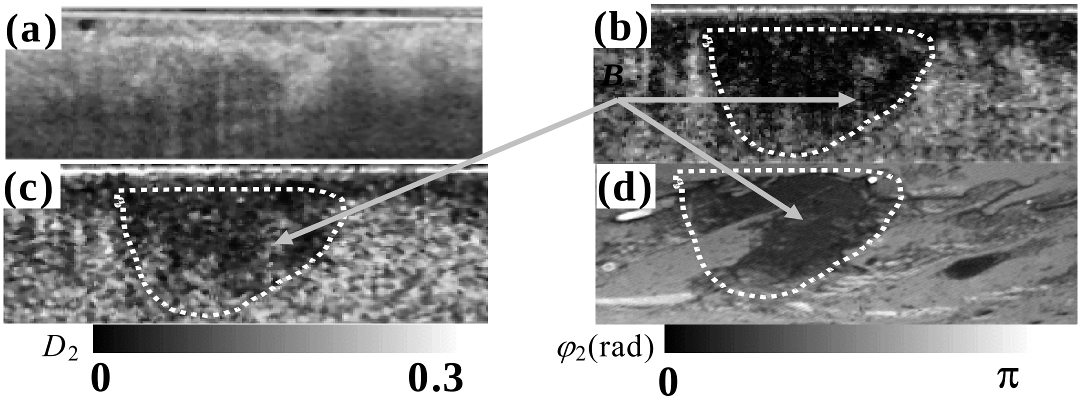

Fig. 6.2 (a) Intensity image (M_{00}, in logarithmic scale), (b) retardation image, (c) diattenuation image, and (d) polarization histologic image of a piece of *ex vivo* rat skin with a burn lesion. The height of each image is 750 μm. The gray scales are for the retardation (φ_2) and diattenuation (D_2) images, respectively. *B*: burn region.

To evaluate the sensitivity of the phase-based polarization contrast in burn-depth determination, we imaged an *ex vivo* skin sample—from a rat belly—containing a burn lesion. The burn lesion was made by touching the skin with a heated (about 100°C) electric iron for less than one second. The calculated intensity image, the retardation image, the diattenuation image and the histological image are shown in Fig. 6.2(a)–(d). The burn region cannot be identified in the intensity image; but it can be clearly seen with marked contrast in the retardation and diattenuation images as verified by the polarization histological image.

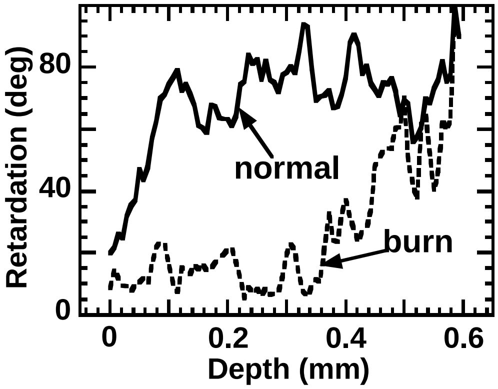

Fig. 6.3 Average of 10 depth profiles of the retardation around the center of the burn area and the normal region to the right of the burn area.

Fig. 6.3 shows the depth profiles of retardation of the burn and normal regions, respectively. Each curve is an average of 10 profiles in the central area of the burn region and in the normal region to the right side of the burn region, respectively. The loss of birefringence in the burn region compared to the normal tissue can be seen clearly. This figure further demonstrates that phase-based polarization contrast provides a sensitive mechanism for evaluating thermal degeneration of biological tissue. Because birefringence and diattenuation are related to the function of several kinds of biological component such as collagen, Mueller OCT is a type of functional imaging.

6.5 Discussion

The differences between conventional OCT and Mueller OCT in their sensitivities to different optical properties of a sample result from their different contrast mechanisms. Conventional OCT is an amplitude-based detection system, which detects the local relative variations of path-length-resolved reflectance from tissues. By modifying an existing theoretical model of OCT[84] to include the effect of polarization, we can express the signal in conventional OCT as

$$\tilde{I}_d(L_r) = 2(I_s I_r)^{1/2} \int_{-\infty}^{\infty} [R(L_s)]^{1/2} \cos[\beta(L_s)] \exp[-4(\Delta L / L_c)^2] \cos(\bar{k}\Delta L) dL_s \,, \qquad 6.10$$

where L_s and L_r are the round-trip optical path lengths of the sample and reference arms, respectively; $\Delta L = L_s - L_r$ is the round-trip optical path-length difference; L_c is the coherence length of the light source; I_r is the intensity of the reference beam; I_s is the reflected intensity of the sample arm; $R(L_s)=[dI_s(L_s)/dL_s]/I_s$ is the path-length-resolved reflectance of the sample; and $\beta(L_s)$ is an equivalent angle between the polarization states of the reference and backscattered sample beams, defined as $\cos[\beta(L_s)] = \langle \mathbf{E}_s(L_s) \cdot \mathbf{E}_r \rangle / (|\mathbf{E}_s(L_s)||\mathbf{E}_r|)$, where $\mathbf{E}_s(L_s)$ and $\mathbf{E}_r$ are the electric vectors of the sample and reference beams, respectively, and the angle brackets denote a time average. The integrand is nonzero mainly in the interval $|\Delta L| \le L_c$. The integration produces a significant value only when $R(L_s)$ varies sharply across a dimension of L_c; otherwise, the integral tends to be zero due to the cosine term in the integrand. A sharp variation of $R(L_s)$ is caused by interfaces between regions of different optical properties. Conventional OCT is, in principle, very sensitive to discontinuity of the refractive index (Δn) as a result of specular reflection. As studied by Pan et al,[84,85] conventional OCT is also sensitive to variations of the anisotropy (Δg) and the scattering coefficient ($\Delta\mu_s$), but it is insensitive to variation of the absorption coefficient ($\Delta\mu_a$). We can see in Eq. 6.10 that the polarization effect of a sample contributes to the recorded conventional OCT signal as an amplitude modulation and is superimposed on the back-reflection effect; consequently, conventional OCT has difficulty in separating the polarization effect from the real morphologic effect of the sample.

To account for the meanings of the measured retardation image, we can divide each depth scan into a number of homogenous segments, each of which has a length less than the axial resolution; each segment can be characterized by a Jones matrix $\mathbf{J}_1(i)$ (i=1, 2, …), which is a function of the equivalent local birefringence [$\delta n(i)$], orientation of the fast axis [$\theta_1(i)$], amplitude transmittances [$P_{q1}(i)$ and $P_{r1}(i)$], and orientation of the diattenuation [$\theta_{d1}(i)$], respectively. For single backscattering and even multiple small-angle scattering, the equivalent round-trip Jones matrix of contiguous m segments of the sample from the surface to the m-th segment can be expressed as

$$\mathbf{J}_{2m} = \prod_{i=1}^{m} \mathbf{J}_1^T(i) \prod_{i=m}^{1} \mathbf{J}_1(i) . \qquad 6.11$$

The equivalent round-trip parameters for the m segments, such as the retardation (φ_{2m}), orientation of the fast axis (θ_{2m}), and diattenuation, can be calculated from $\mathbf{J}_{2m}$. When

$\theta_1(1) = \theta_{d1}(1) = \theta_1(2) = \theta_{d1}(2) = \cdots = \theta_1(m) = \theta_{d1}(m)$, if $\varphi_{2m} \le \pi$, φ_{2m} in the retardation image increases with depth while θ_{2m} keeps constant; if φ_{2m} covers a range greater than π, it causes fringes in both the retardation and orientation images because a retarder $\mathbf{J}(\varphi_{2m} + \pi, \theta_{2m})$ is equivalent to a retarder $\mathbf{J}(\pi - \varphi_{2m}, \theta_{2m} \pm \pi/2)$, ($\varphi_{2m}, \theta_{2m} \in [0, \pi]$), a phenomenon observed in the retardation and orientation images of samples like porcine tendon.[20] In this case, the differential retardation image reflects a map of the local birefringence. Otherwise, φ_{2m} and θ_{2m} are also functions of both $\theta_1(i)$ and $\theta_{d1}(i)$ in the optical path, making the retardation image complex to interpret rigorously unless the local polarization properties can be calculated, which is possible only with Mueller OCT.

The Jones matrix of the first pixel of each A line represents the round-trip Jones matrix of the first segment, i.e. $\mathbf{J}_2(1) = \mathbf{J}_1^T(1)\mathbf{J}_1(1)$. If $\mathbf{J}_1(1)$ can be calculated from $\mathbf{J}_2(1)$ by developing some effective algorithms, the first segment can be peeled off to yield the round-trip Jones matrix of the second segment:

$$\mathbf{J}_1^T(2)\mathbf{J}_1(2) = [\mathbf{J}_1^T(1)]^{-1}\mathbf{J}_2(1)\mathbf{J}_1^{-1}(1). \qquad 6.12$$

By using this strategy layer by layer, the one-way Jones matrix of each segment can thus be extracted and the images of the local polarization parameters can be calculated, which should be free of fringes because the retardation of each segment should be much less than π. This algorithm is important in fiber-based PS-OCT system for eliminating the polarization distortions on the measured polarization-based images caused by the sampling fiber.[86]

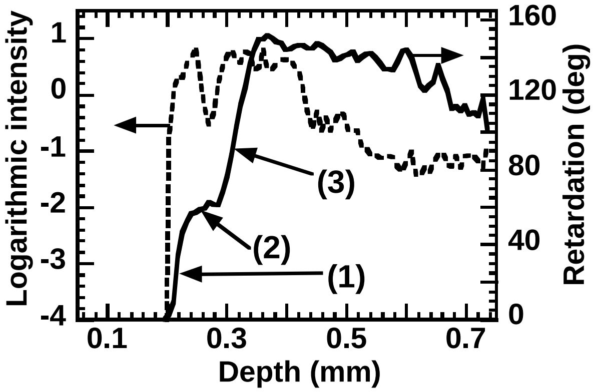

Fig. 6.4 Averaged depth profiles of the intensity (in logarithmic scale) and retardation over the region marked with a horizontal white bar in Fig. 6.1(b). Labels (1), (2), and (3): layers revealed.

Unlike amplitude-based contrast, phase-based polarization contrast is insensitive to a boundary caused by Δn, and, as a result, a boundary in the intensity image may not be reflected in the retardation image unless there is a corresponding difference of δn across the boundary, the value of which also determines the sharpness of a boundary in the retardation image. Due to the integration over depth, a boundary caused by δn in the retardation image may not be as sharp as the corresponding boundary caused by Δn in the intensity image. However, as can be seen in Fig. 6.2(b), the interface between two regions of different δn can be distinguished with sufficient accumulated contrast within a few coherence lengths. Fig. 6.4 shows the depth profiles of intensity and retardation averaged laterally over the range marked by the white bar in Fig. 6.1(b). The retardation curve revealed several layers from the surface down into the skin. Layer (1) and layer (3) are highly birefringent, indicating the keratin in the epidermis and the dermal papilla, respectively. Layer (2) has almost no birefringence, which likely corresponds to the living epidermis.

We regard the apparent phase retardation induced by mechanisms other than birefringence as the background of the phase-based polarization contrast. Besides birefringence, scattering can also alter the polarization state of light and cause phase retardation. Alteration of the polarization state of the propagating light is dependent on the geometry and the refractive index of the scattering particles.[87,88]

6.6 Conclusion

In summary, a unique feature of Mueller-matrix OCT is its capability of separating various contrast mechanisms, in which the amplitude-based contrast is sensitive to the boundaries formed primarily by regions of different indexes of refraction while the phase-based polarization contrast and the orientation-based contrast originate from the components of biological tissues with optical polarization effect. Experimental results show that phase-based polarization contrast is more sensitive to thermal degeneration of biological tissues than amplitude-based contrast. The combination of amplitude-based contrast with phase-based polarization contrast and the orientation-based contrast provides more comprehensive information about biological tissues. Phase-based polarization contrast is a promising imaging mechanism for assessing burn depth *in vivo*.

7 FIBER-BASED MULTI-CHANNEL MUELLER-MATRIX OCT

7.1 Introduction

In contrast to conventional optical coherence tomography (OCT), polarization-sensitive OCT (PS-OCT) adds the polarization properties of the sample as a contrast mechanism. However, practical applications of PS-OCT have been limited by the difficulty of its optical-fiber implementation. A single-mode optical fiber (SMF) alters the polarization state of the guided light due to its inherent birefringence. The birefringence varies with the bending and twisting of the fiber during manipulation of the imaging probes, which can result in dynamic distortion in PS-OCT images. Therefore, a dynamic calibration technique is required to eliminate this effect.

Based on previous studies, a Jones matrix can be applied in PS-OCT to completely characterize the polarization properties of a sample. If the one-way Jones or Mueller matrix of the sampling optical fiber can be determined, the polarization distortion caused by the sampling fiber can be eliminated from the PS-OCT images. Multi-channel Mueller OCT can measure the Jones and Mueller matrices of a sample with a single scan and thus offer the possibility of rigorously eliminating the polarization effect of the sampling fiber. This method allows fiber-based Mueller OCT to acquire a calibrated Mueller-matrix image as rapidly as conventional OCT acquires a regular image. In this section, we report a new rigorous calibration algorithm, which was validated with both simulated and experimental data and was also applied to imaging the skin of a rat.

7.2 Calibration Algorithm

In general, a pure retarder can be characterized by a homogeneous Jones matrix that has two orthogonal elliptical eigen-vectors, each representing an eigen-polarization. A linear retarder is a special case where the eigen-polarizations are linear; and a Faraday rotator is another special case where the eigen-polarizations are circular. When two or more linear retarders are cascaded, the overall retarder is generally elliptical unless the axes are aligned. Due to its randomly distributed birefringence along the core, a SMF should be treated as an elliptical retarder.

We first introduce the general properties of a retarder. The 2×2 Jones matrix of an elliptical retarder is expressed in Eq. 3.14 with three independent real parameters. As discussed in section 6.3, the roundtrip transformation effect of an elliptical retarder is equivalent to the one-way transformation of a linear retarder. As a result, only two independent real parameters are needed to describe the roundtrip Jones matrix ($\mathbf{J}_2$). The roundtrip Jones matrix of an optical component can be calculated from its one-way Jones matrix ($\mathbf{J}_1$) according Eq. 6.5.

As shown in Fig. 7.1, in a fiber-based Mueller OCT system, the incident sampling light undergoes transformation sequentially, first through the sampling fiber and the sample in forward propagation and then the sample and the sampling fiber in backward propagation. Therefore, the raw roundtrip Jones matrix ($\mathbf{J}_{sf2}$) can be expressed in terms of the one-way Jones matrix of the sampling fiber ($\mathbf{J}_{f1}$) and the roundtrip Jones matrix of the sample at a given imaging depth ($\mathbf{J}_{s2}$) as

$$\mathbf{J}_{sf2} = \mathbf{J}_{f1}^{T}\mathbf{J}_{s2}\mathbf{J}_{f1}. \qquad 7.1$$

The roundtrip Jones matrix of the sampling fiber ($\mathbf{J}_{f2}$) can be calculated from the OCT signal reflected from the sample surface:

$$\mathbf{J}_{f2} = \mathbf{J}_{f1}^{T}\mathbf{J}_{f1}. \qquad 7.2$$

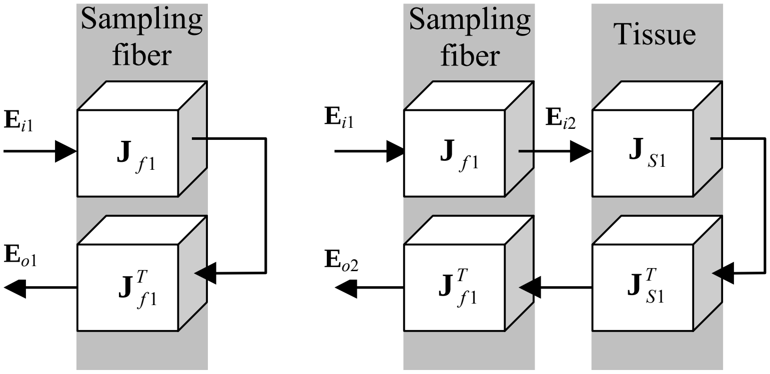

Fig. 7.1 Illustration of the polarization transformation in the sample arm. $\mathbf{E}_{i1}$ and $\mathbf{E}_{i2}$: incident Jones vectors for the sampling fiber and the sample; $\mathbf{E}_{o1}$: the measured output roundtrip Jones vector from the sample surface; $\mathbf{E}_{o2}$: the roundtrip Jones vector representing the transformation result of both the fiber and the tissue layer; $\mathbf{J}_{f1}$ and $\mathbf{J}_{s1}$: the one-way Jones matrix of the sampling fiber and the sample.

To eliminate the distortion, the best approach is to calculate $\mathbf{J}_{f1}$ from $\mathbf{J}_{f2}$ for each A scan. However, there are three real variables in $\mathbf{J}_{f1}(\varphi_{f1}, \theta_{f1}, \delta_{f1})$ but only two in $\mathbf{J}_{f2}(\varphi_{f2}, \theta_{f2})$. Consequently, Eq. 7.2 provides only two independent relationships; therefore, $\mathbf{J}_{f1}$ can only be determined from $\mathbf{J}_{f2}$ with a free parameter.

For each $\mathbf{J}_{f2}$, we can always find a unique hypothetical linear retarder $\mathbf{J}_{fl1}$ to satisfy

$$\mathbf{J}_{f2} = \mathbf{J}_{fl1}^{T}\mathbf{J}_{fl1}. \tag{7.3}$$

We introduce the following matrix to reflect the free parameter:

$$\mathbf{J}_{fc1} = \mathbf{J}_{f1}\mathbf{J}_{fl1}^{-1}. \tag{7.4}$$

Removing the round-trip effect of $\mathbf{J}_{fl1}$ from $\mathbf{J}_{sf2}$, we obtain a new matrix $\mathbf{J}_{sc2}$:

$$\mathbf{J}_{sc2} = (\mathbf{J}_{fl1}^{T})^{-1}\mathbf{J}_{sf2}\mathbf{J}_{fl1}^{-1}. \tag{7.5}$$

Based on Eqs. 7.1, 7.3–7.5, we have the following solution representing the general calibration algorithm in a matrix form:

$$\mathbf{J}_{s2} = (\mathbf{J}_{fc1}^{T})^{-1}\mathbf{J}_{sc2}\mathbf{J}_{fc1}^{-1}. \tag{7.6}$$

The round-trip retardation (φ_{s2}) of the sample can be calculated by Eq. 6.2 or, in the case of negligible diattenuation in the sample, by

$$\varphi_{s2} = 2\cos^{-1}\{[J_{s2}(1,1) + J_{s2}(2,2)]/2\}. \tag{7.7}$$

We can also prove from Eq. 7.4 that the elements of $\mathbf{J}_{fc1}$ are real numbers and that

$$J_{fc1}^{2}(1,1) + J_{fc1}^{2}(1,2) = 1. \tag{7.8}$$

Consequently, we can introduce a new parameter γ as follows:

$$\mathbf{J}_{fc1} = \begin{bmatrix} \cos\gamma & \sin\gamma \\ -\sin\gamma & \cos\gamma \end{bmatrix}. \tag{7.9}$$

$\mathbf{J}_{fc1}$ thus represents a rotation matrix. In other words, the Jones matrix of the sampling fiber is decomposed into a linear retarder and a rotator. Equation 7.6 is equivalent to rotating the fast axis of $\mathbf{J}_{s2}$ along the axis of the incident light by an angle γ. This rotation does not affect the amplitudes of either the birefringence or diattenuation. As a result, the calibrated round-trip retardation of the sample can be calculated exactly from Eq. 6.2 or 7.7. From Eqs. 7.6 and 7.9, we can calculate the calibrated orientation of birefringence as follows:

$$\theta_{s2} = \theta_{sc2} - \gamma \,. \qquad 7.10$$

where θ_{sc2} can be calculated from the fast eigenvector of $\mathbf{J}_{sc2}$.

The calibration in Eq.7.10 has an offset γ, which depends on the parameters of the sampling fiber only. This offset is a constant in a frame of image as long as the parameters of the sampling fiber are kept constant during the image acquisition of each frame, which is the case when the fast lateral scanning of OCT does not move the sampling fiber. Therefore, a relative distribution of the orientation of the birefringence can be retrieved. If the parameters of the sampling fiber are varied among the A scans, which is true when the lateral scanning in OCT does move the sampling fiber, γ will differ among the A lines. In this case, if the orientation of the birefringence of the surface layer is constant or known *a priori,* or if a known thin retarder is attached to the sample as the first layer, γ can be eliminated. In either case, φ_{s2} can be calculated exactly.

We tested the algorithm for a simulated fiber with parameters $\varphi_{f1} = 46^\circ, 0 \le \theta_{f1} < \pi,\ 0 \le \delta_{f1} < \pi$ and $0 < \varphi_{f1} < \pi,\ 0 \le \theta_{f1} < \pi,\ \delta_{f1} = 50^\circ$, respectively, together with a sample having various parameters of birefringence. The birefringent parameters of the simulated sample can be completely recovered. Fig. 7.2 shows the simulation results with $\varphi_{s2} = 36^\circ$.

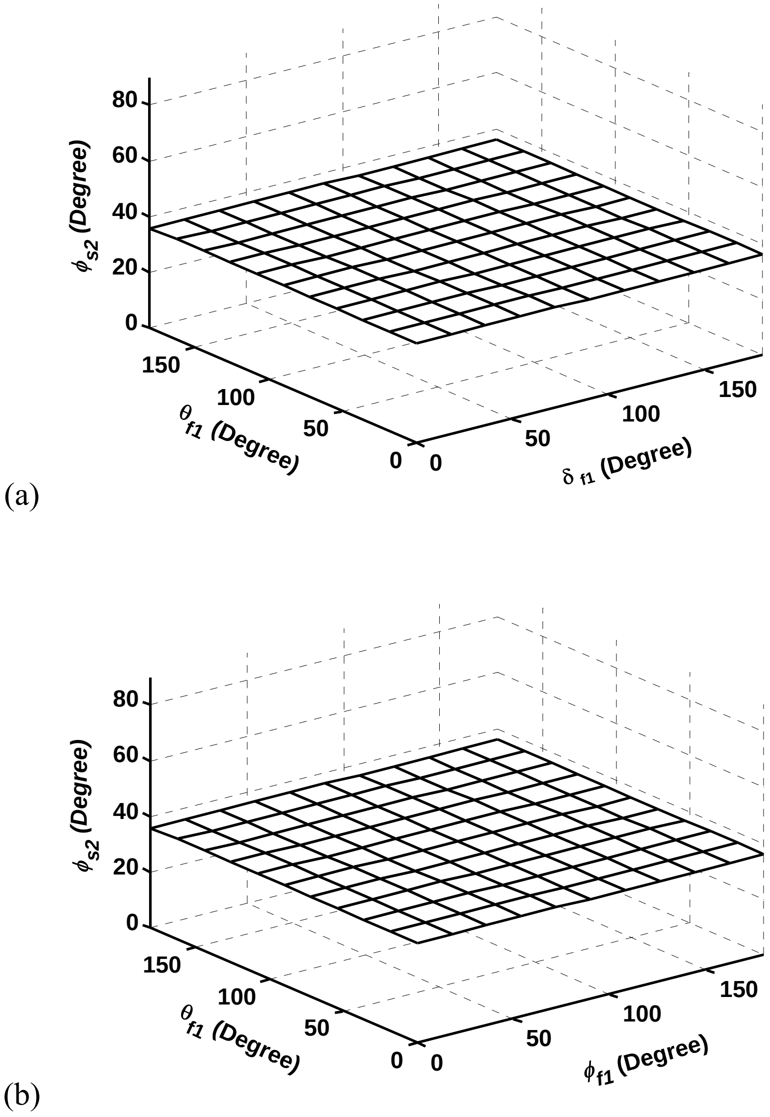

Fig. 7.2 The calibration results for a simulated sample with $\varphi_{s2} = 36^\circ$ and sampling-fiber parameters: (a) $\varphi_{f1} = 46^\circ; 0 \le \theta_{f1} < \pi;\ 0 \le \delta_{f1} < \pi$ and (b) $\delta_{f1} = 50^\circ; 0 \le \theta_{f1} < \pi;\ 0 \le \varphi_{f1} < \pi$.

7.3 Comparison of the Algorithm with Conventional PS-OCT

In this section, we compare the above algorithm for eliminating the polarization distortions of the sampling fiber with the a previous algorithm used in conventional fiber-based PS-OCT.[89] As illustrated in Fig. 7.1, we have the following relations:

$$\mathbf{E}_{i2} = \mathbf{J}_{f1}\mathbf{E}_{i1}, \qquad 7.11$$

$$\mathbf{E}_{o1} = \mathbf{J}_{f1}^{T}\mathbf{J}_{f1}\mathbf{E}_{i1}, \qquad 7.12$$

$$\mathbf{E}_{o2} = \mathbf{J}_{f1}^{T}\mathbf{J}_{s2}\mathbf{J}_{f1}\mathbf{E}_{i1}. \qquad 7.13$$

Each of the Jones vectors $\mathbf{E}_{i1}$, $\mathbf{E}_{i2}$, $\mathbf{E}_{o1}$, and $\mathbf{E}_{o2}$ has a corresponding Stokes vector $\mathbf{S}_{i1}$, $\mathbf{S}_{i2}$, $\mathbf{S}_{o1}$ and $\mathbf{S}_{o2}$, respectively. In the algorithm developed in Ref. 89, a rotation matrix was calculated to transform $\mathbf{S}_{o1}$ to $\mathbf{S}_{o2}$ in the Poincare sphere in the effort to calculate the polarization parameters of the sample. The rotation matrix is considered to represent a pure retarder. Because Jones and Mueller calculus are equivalent in PS-OCT and Poincare sphere just represents the visualization of Mueller calculus, we use Jones calculus for its simplicity to examine the effect of the algorithm in Ref. 89 on the calculated polarization parameters of the sample.

From Eq. 7.4, we can see that the one-way Jones matrix of the sampling fiber can be decomposed into the product of a linear retarder and a rotator:

$$\mathbf{J}_{f1} = \mathbf{J}_{fc1}\mathbf{J}_{fl1}. \qquad 7.14$$

Eq. 7.12 becomes

$$\mathbf{E}_{o1} = \mathbf{J}_{fl1}^{T}\mathbf{J}_{fc1}^{T}\mathbf{J}_{fc1}\mathbf{J}_{fl1}\mathbf{E}_{i1} = \mathbf{J}_{fl1}^{T}\mathbf{J}_{fl1}\mathbf{E}_{i1}, \qquad 7.15$$

and we have

$$\mathbf{J}_{fl1}\mathbf{E}_{i1} = \mathbf{J}_{fl1}^{-1}\mathbf{E}_{o1}. \qquad 7.16$$

We can then represent $\mathbf{E}_{o2}$ with $\mathbf{E}_{o1}$ by inserting Eq. 7.16 into Eq.7.13:

$$\begin{aligned}\mathbf{E}_{o2} &= \mathbf{J}_{fl1}^{T}\mathbf{J}_{fc1}^{T}\mathbf{J}_{s2}\mathbf{J}_{fc1}\mathbf{J}_{fl1}^{-1}\mathbf{E}_{o1}\\ &= (\mathbf{J}_{fl1}\mathbf{J}_{fc1}^{-1})\mathbf{J}_{s2}(\mathbf{J}_{fl1}\mathbf{J}_{fc1}^{-1})^{-1}\mathbf{E}_{o1}\,.\\ &\neq \mathbf{J}_{s2}\mathbf{J}_{f2}\mathbf{E}_{01}\end{aligned} \qquad 7.17$$

The transformation matrix $(\mathbf{J}_{fl1}\mathbf{J}_{fc1}^{-1})\mathbf{J}_{s2}(\mathbf{J}_{fl1}\mathbf{J}_{fc1}^{-1})^{-1}$ in Eq. 7.17 is the representation in the Jones calculus of the calculated rotation matrix by the algorithm in Ref. 89. This matrix is generally an elliptical retarder and is not identical to what we are after, i.e., the roundtrip Jones matrix of the tissue: $\mathbf{J}_{s2}$. We can prove that the retardation of $(\mathbf{J}_{fl1}\mathbf{J}_{fc1}^{-1})\mathbf{J}_{s2}(\mathbf{J}_{fl1}\mathbf{J}_{fc1}^{-1})^{-1}$ happens to be equal to the retardation of $\mathbf{J}_{s2}$, but the orientation has a complicated nonlinear relationship with the orientation of $\mathbf{J}_{s2}$.

When the fiber can be characterized as a linear retarder, $\mathbf{J}_{fc1}$ becomes an identity matrix and Eq. 7.17 becomes:

$$\mathbf{E}_{o2} = \mathbf{J}_{fl1}\mathbf{J}_{s2}\mathbf{J}_{fl1}^{-1}\mathbf{E}_{o1} \neq \mathbf{J}_{s2}\mathbf{E}_{o1}. \qquad 7.18$$

The transformation matrix $\mathbf{J}_{fl1}\mathbf{J}_{s2}\mathbf{J}_{fl1}^{-1}$ still represents an elliptical element and is not the desired matrix $\mathbf{J}_{s2}$.

Another aspect we must notice is that this algorithm is not valid when diattenuation exists in a sample because the rotation of the Stokes vector from $\mathbf{S}_{o1}$ to $\mathbf{S}_{o2}$ is assumed to be caused only by birefringence. As a result, we regard conventional fiber-based PS-OCT as a single-parameter PS-OCT system, which can reveal the amplitude of birefringence only.

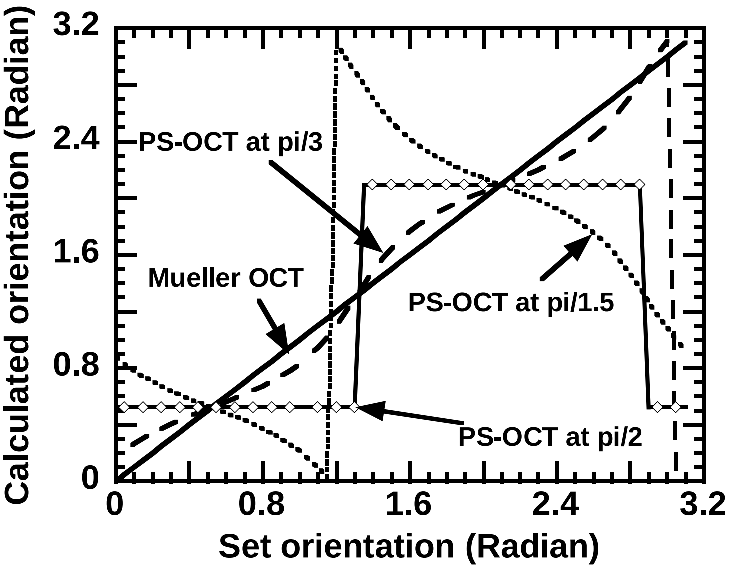

Fig. 7.3 The calculated orientation of the fast axis with the two different algorithms for a fiber-based PS-OCT system.

The orientation of the fast axis of the transformation matrix in Eq. 7.17 was calculated for a system whose sampling fiber can be considered as a linear retarder with one-way retardation $\varphi_{f1} = \pi/3, \pi/2, \pi/1.5$ and orientation $\theta_{f1} = \pi/6$. The roundtrip retardation of the sample is $\varphi_2 = \pi/3$, and its orientation changes from 0 to π. The calculation results are shown in the Fig. 7.3. For comparison, the orientation of the fast axis of the sample extracted with the algorithm of Mueller OCT is also shown in the figure. We draw the following conclusions:

1). The algorithm of the Mueller OCT is stable and yields exact orientation of the fast axis of the sample in the entire data range.

2). Without discriminating the one-way and roundtrip transformation effects, the algorithm used in conventional fiber-based PS-OCT is unable to consider the actual order of transformation. As a result, the calculated orientation of the fast axis of the sample is wrong except at two points--when the orientations of the fiber and the sample are either parallel or orthogonal. With an increase of retardation in the sampling fiber, the error becomes more severe.

7.4 Experimental System

Fig. 7.4 shows a schematic of the experimental system. The two source beams from two SLD sources (central wavelength $\overline{\lambda} = 850$ nm, FWHM bandwidth $\Delta\lambda = 26$ nm), amplitude-modulated at 3 kHz and 3.5 kHz, respectively, are merged by a polarizing beam splitter (PBS1), filtered by a spatial-filter, and then split by a non-polarizing beam splitter (NBS). Both the sample and the reference beams are coupled into a 0.5-m long SMF, respectively. A 45° linear polarizer (LP) is used to control the polarization state of the reference beam. The combined backscattered and reference light is split into the horizontally (*H*) and vertically (*V*) polarized components by a polarizing beam splitter PBS2; these are detected by photodiodes PDH and PDV, respectively. The data processing and the Jones matrix calculation have been described in section 5.

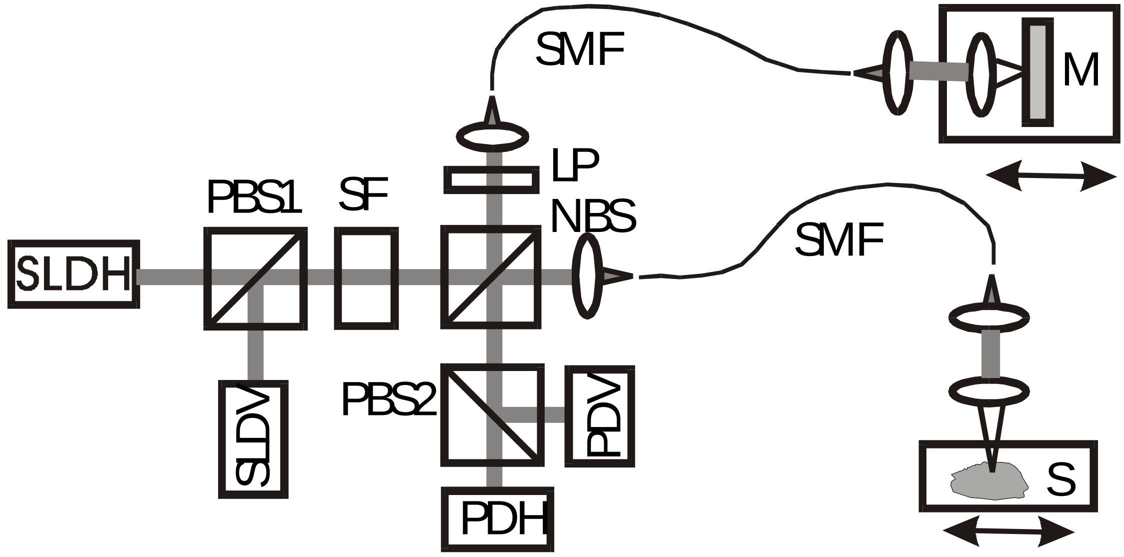

Fig. 7.4 Schematic of the fiber-based Mueller OCT system. SLDH and SLDV: superluminescent diodes, horizontally polarized (*H*) and vertically polarized (*V*), respectively; PBS1 and PBS2: polarizing beam splitters; SF: spatial filter assembly; NBS: non-polarizing beam splitter; M: mirror; SMF: single-mode optical fiber; PDH and PDV: photodiodes for the *H* and *V* polarization components, respectively.

7.5 Experimental Results and Discussion

We first tested the system by imaging a quarter-wave ($\lambda/4$) plate in combination with a mirror, for a frame consisting of 35 A scans with a lateral span of 1 mm. The sampling fiber was intentionally deformed every fifth A scan to vary its polarization property. In Fig. 7.5, we can see that the raw round-trip retardation of the $\lambda/4$ plate was severely distorted by the sampling fiber. The measured $\mathbf{J}_{f2}$ was used to cancel the distortion using the above algorithm. The calibrated φ_{s2} of the $\lambda/4$ plate shown in Fig. 7.5 accurately matches the expected value of $\lambda/2$, indicating the validity of our algorithm.

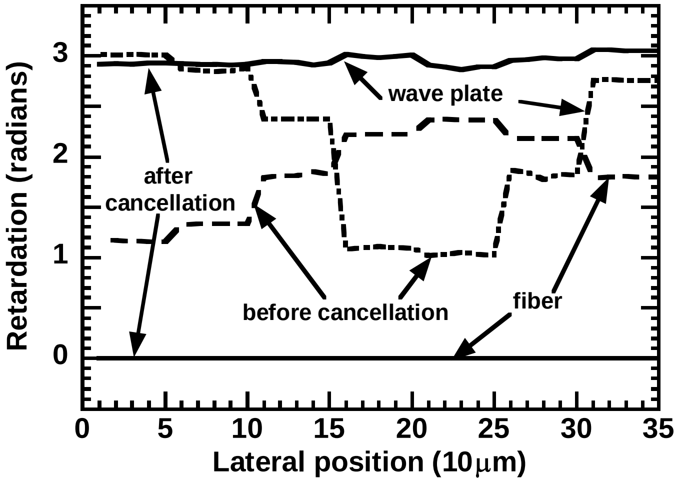

Fig. 7.5 Phase retardation of a $\lambda/4$ plate calculated from the measured Jones matrix before and after cancellation of the polarization distortion caused by the sampling optical fiber. The phase retardation of the sampling fiber is shown as well, which is zero after cancellation by definition.

We then used the fiber-based Mueller OCT system to image a biological sample—the skin of a rat tail [Berlin Drucrey (BD-IV)]. After the hair of the tail was removed with hair remover lotion, the tail was scrubbed with glycerin. Two-dimensional data of the skin were taken by laterally moving the sample between A scans. The sampling fiber was intentionally disturbed between A scans to introduce distortions. The Jones matrix was calibrated pixel-wise and then converted into its corresponding 4×4 Mueller matrix. Fig. 7.6 shows the images of the polarization-independent M_{00} element of the Mueller matrix, the retardation before calibration φ_{sf2}, and the retardation after calibration φ_{s2}. Some structures, like the dermal-epidermal junction and the collagen-rich dermal papillae, can be clearly seen in the M_{00} and φ_{s2} images while they are blurred in the φ_{sf2} image due to the distortion of the sampling fiber. Also shown in Fig. 7.6 is the haematoxylin and eosin (*HE*) histological image of the tail skin of the same breed. The calibrated OCT images conform well with the histological image.

Another skin sample from the rat tail was imaged *in vivo*. After the rat was anesthetized (ketamine 60 mg/kg, IM) and the hair of the tail was removed with hair remover lotion, the tail was scrubbed with glycerin. Two-dimensional data of the skin were taken by laterally moving the sample while the sampling fiber was kept steady during each frame of image. Fig. 7.7 shows the images of the polarization-independent M_{00} element of the Mueller matrix, the amplitude of retardation after calibration, the orientation of the fast axis, and the haematoxylin and eosin (*HE*) histological image of the tail skin of the same breed.

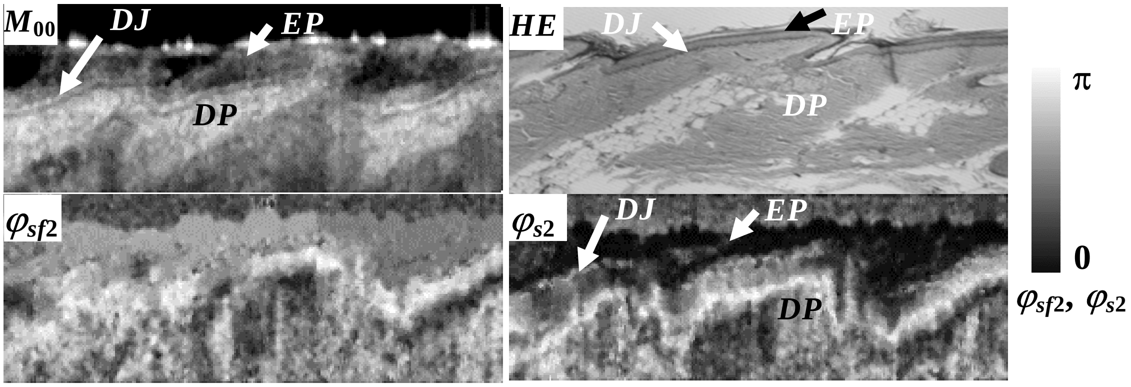

Fig. 7.6 The M_{00} image of the Mueller matrix, the retardation images before and after cancellation of the polarization effect of the sampling fiber φ_{sf2} and φ_{s2} of the skin of a rat tail measured with the fiber-based Mueller OCT system. An *HE* stained histological image is also shown for comparison. The M_{00} image is on a logarithmic scale while the retardation images are on a linear scale. The height of each image is 1 mm. *EP*: epidermis; *DP*: dermal papilla; and *DJ*: dermal-epidermal junction.

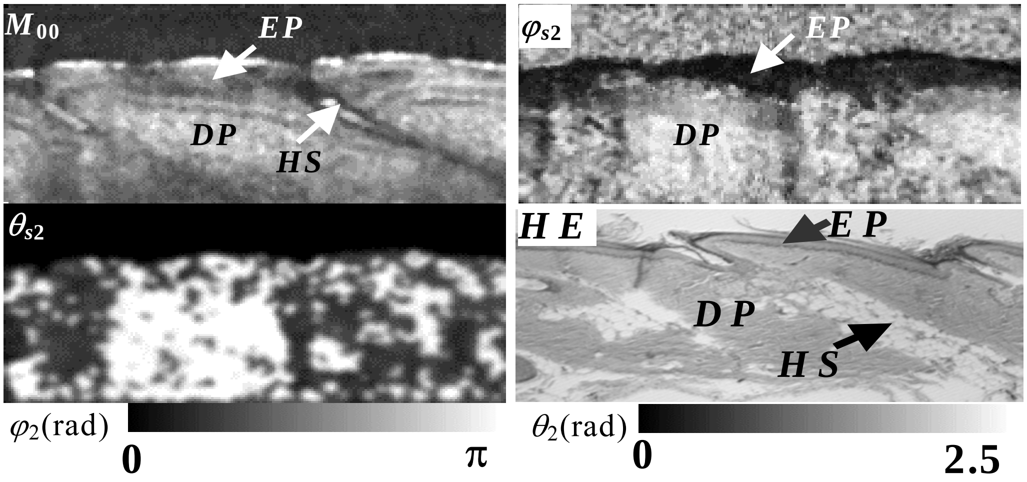

Fig. 7.7 The M_{00} image of the Mueller matrix, the calculated retardation image φ_{s2}, and the image of the orientation of the fast axis of the skin of a rat tail measured *in vivo* with the fiber-based Mueller OCT system. The M_{00} image is in logarithmic scale while the retardation image is in linear scale. The height of the images is 1mm. *EP*: Epidermis; *DP*: dermal papilla; *HS*: hair shaft.

7.6 Conclusion

In conclusion, single-mode optical fibers were successfully incorporated into our Mueller OCT system. A rigorous algorithm was invented to exactly eliminate the polarization effect of the sampling fiber on the retardation image of a sample dynamically. With this algorithm, the distribution of the orientation of the birefringence can also be extracted with only a constant offset in each pixel as long as the sampling fiber is not scanned during the acquisition of each frame of image. Our fiber-based Mueller OCT system was successfully applied to imaging biological samples.

8 CONCLUSION

Mueller-matrix OCT is the most general form of PS-OCT. Mueller-matrix OCT distinguishes itself from conventional PS-OCT by providing comprehensive polarization information of biological tissues. Due to the interference-based heterodyne detection scheme used in OCT, a sample behaves as a non-depolarizing medium. This conclusion allows the application of Jones calculus in OCT.

We developed a novel multi-channel polarization-sensitive Mueller-matrix OCT system. This technique enables the acquisition of a 2D tomographic Jones matrix, which can be converted into a Mueller matrix. The depth-resolved Jones matrix of a sample can be determined with a single scan; as a result, this technique is capable of imaging either hard or soft biological tissues. In addition, the Jones matrix can be decomposed to extract important information on the optical polarization properties of a sample, such as birefringence, orientation of the fast axis, and diattenuation. In our study, the Jones-matrix images of the thermally treated porcine tendon clearly showed changes in birefringence due to thermal damage.

A unique feature of Mueller OCT is its capability of separating various contrast mechanisms, in which the amplitude-based contrast is sensitive to the boundaries formed primarily by regions of different indexes of refraction while the phase-based polarization contrast and the orientation-based contrast originate from the components of biological tissues with optical polarization effect. Experimental results show that phase-based polarization contrast is more sensitive to thermal degeneration of biological tissues than amplitude-based contrast. The combination of amplitude-based contrast with phase-based polarization contrast and the orientation-based contrast provides more comprehensive information about biological tissues. Phase-based polarization contrast is a promising imaging mechanism for assessing burn depth *in vivo*.

Single-mode optical fibers were successfully incorporated into our Mueller OCT system. A rigorous algorithm was invented to exactly eliminate the polarization effect of the sampling fiber on the retardation image of a sample dynamically. With this algorithm, the distribution of the orientation of the birefringence can also be extracted with only a constant offset in each pixel as long as the sampling fiber is not scanned during the acquisition of each frame of image. Our fiber-based Mueller OCT system was successfully applied to imaging biological samples.

REFERENCES

1 D. Huang, E. A. Swanson, C. P. Lin, J. S. Schuman, W. G. Stinson, W. Chang, M. R. Hee, T. Flotte, K. Gregory, C. P. Puliafito, and J. G. Fujimoto, "Optical coherence tomography," Science **254**, 1178–1181 (1991).

2 . R. C. Youngquist, S. Carr, and D. E. N. Davis, “Optical coherence domain reflectometry: a new optical evaluation technique,” Opt. Lett. **12**, 158–160 (1987).

3. K. Takata, I. Yokohama, K. Chida, and J. Noda, “New measurement system for fault location in optical waveguide based on an interferometric technique,” Appl. Opt. **26**, 1603–1606 (1987).

4. V. Guedes, J. Schuman, E. Hertzmark, G. Wollstein, A. Correnti, R. Mancini, D. Lederer, S. Voskanian, L. Velazquez, H. Pakter, T. Pedut-Kloizman, J. G. Fujimoto, and C. Mattox, “Optical coherence tomography measurement of macular and nerve fiber layer thickness in normal and glaucomatous human eyes”, OPHTHALMOLOGY **110**, 177-189 (2003).

5. I. K. Jang, B. E. Bouma, D. H. Kang, S. J. Park, S. W. Park, K. B. Seung, K. B. Choi, M. Shishkov, K. Schlendorf, E. Pomerantsev, S. L. Houser, H. T. Aretz, and G. J. Tearney, “Visualization of coronary atherosclerotic plaques in patients using optical coherence tomography: comparison with intravascular ultrasound”, J. The American College of Cardiology, **39**, 604-609 (2002).

6. S. N. Roper, M. D. Moores, G. V. Gelikonov, F. I. Feldchtein, N. M. Beach, M. A. King, V. M. Gelikonov, A. M. Sergeev, and D. H. Reitze, "In vivo detection of experimentally induced cortical dysgenesis in the adult rat neocortex using optical coherence tomography," J. Neuroscience Methods, **80**, 91–98 (1998).

7. Julia Welzel, "Optical coherence tomography in dermatology: a review," Skin Research and Technology, **7**, 1–9 (2001).

8. L. L. Otis, M. J. Everett, U. S. Sathyam, and B. W. Colston, "Optical coherence tomography: a new imaging technology for dentistry", J. The American Dental Association, **131**, 511–514 (2000).

9. T. M. Yelbuz, M. A. Choma, L. Thrane, M. L. Kirby, and J. A. Izatt, "Optical coherence tomography **-** A new high-resolution imaging technology to study cardiac development in chick embryos", Circulation, **106**, 2771-2774 (2002).

10. A. V. D'Amico, M. Weinstein, X. D. Li, J. P. Richie, and J. G. Fujimoto, "Optical coherence tomography as a method for identifying benign and malignant microscopic structures in the prostate gland", Urology, **55**, 783-787 (2000).

11. S. J. Spechler, "Screening and surveillance for complications related to gastroesophageal reflux disease", American J. of Medicine, **111**, 130-136 (2001).

12. X. Li, C. Chudoba, T. Ko, C. Pitris, and J. G. Fujimoto, "Imaging needle for optical coherence tomography," Opt. Lett, **25**, 1520–1522 (2000).

13. G. J. Tearney, B. E. Bouma, and J. G. Fujimoto, "High-speed phase- and group-delay scanning with a grating-based phase control delay line," Opt. Lett. **22**, 1811–1813 (1997).

14. M. E. Brezinski, G. J. Tearney, N. J. Weissman, S. A. Boppart, B. E. Bouma, M. R. Hee, A. E. Weyman, E. A. Swanson, J. F. Southern, and J. G. Fujimoto, "Assessing atherosclerotic plaque morphology—comparison of optical coherence tomography and high frequency intravascular ultrasound," Heart **77**, 397–403 (1997).

15. Z. Chen, T. E. Milner, D. Dave, and J. S. Nelson, "Optical Doppler tomography imaging of fluid flow velocity in highly scattering media," Opt. Lett. **22**, 64–66 (1997).

16. J. A. Izatt, M. D. Kulkarni, S. Yazdanfar, J. K. Barton, and A. J. Welsh, "In vivo bidirectional color Doppler flow imaging of picoliter blood volumes using optical coherence tomography," Opt. Lett. **22**, 1439–1441 (1997).

17. J. F. de Boer, T. E. Milner, M. J. C. van Gemert and J. S. Nelson, "Two-dimensional birefringence imaging in biological tissue by polarization-sensitive optical coherence tomography," Opt. Lett. **22**, 934–936 (1997).

18. G. Yao and L.-H. V. Wang, "Two-dimensional depth-resolved Mueller matrix characterization of biological tissue by optical coherence tomography," Opt. Lett. **24**, 537–539 (1999).

19. S. Jiao, G. Yao and L.-H. V. Wang, “Depth-resolved two-dimensional Stokes vectors of backscattered light and Mueller matrices of biological tissue measured with optical coherence tomography,” Appl. Opt. **39**, 6318–6324 (2000).

20. S. Jiao and L.-H. V. Wang, “Two-dimensional depth-resolved Mueller matrix of biological tissue measured with double-beam polarization-sensitive optical coherence tomography,” Opt. Lett. **27**, 101–103 (2002).

21. S. Jiao and L.-H. V. Wang, “Jones-matrix imaging of biological tissues with quadruple-channel optical coherence tomography,” J. Biomed. Opt. **7**, 350–358 (2002).

22 Y. Yasuno, S. Makita, Y. Suto, M. Itoh, and T. Yatagai, “Birefringence imaging of human skin by polarization-sensitive spectral interferometric optical coherence tomography”, Opt. Lett. **27**, 1803–1805 (2002).

23. M. R. Hee, D. Huang, E. A. Swanson and J. G. Fujimoto, “Polarization-sensitive low-coherence reflectometer for birefringence characterization and ranging,” J. Opt. Soc. Am. **B 9**, 903–908 (1992).

24. U. Morgner, W. Drexler, F. X. K¨artner, X. D. Li, C. Pitris, E. P. Ippen, and J. G. Fujimoto, “Spectroscopic optical coherence tomography”, Opt. Lett. **25**, 111-113 (2000).

25 . B. Povazay, K. Bizheva, A. Unterhuber, B. Hermann, H. Sattmann, A. F. Fercher, W. Drexler, A. Apolonski, W. J. Wadsworth, J. C. Knight, P. St. J.

Russell, M. Vetterlein, and E. Scherzer, “Submicrometer axial resolution optical coherence tomography,” Opt. Lett. **27**, 1800-1802 (2002).

26. A. Rollins, S. Yazdanfar, M. Kulkarni, R. Ung-arunyawee, and J. A. Izatt, "*In vivo* video rate optical coherence tomography," Optics Express **3**, 219–229 (1998).

27. G. J. Tearney, B. E. Bouma, and J. G. Fujimoto, "High-speed phase- and group-delay scanning with a grating-based phase control delay line," Opt. Lett. **22**, 1811–1813 (1997).

28. A. Dubois, L. Vabre, A. C. Boccara, and E. Beaurepaire, “High-resolution full-field optical coherence tomography with a Linnik microscope”, Appl. Opt. **41**, 805–812 (2002).

29. Y. Yasuno, Y. Sutoh, M. Nakama, S. Makita, M. Itoh, and T. Yatagai, “Spectral interferometric optical coherence tomography with nonlinear b-barium borate time gating”, Opt. Lett. **27**, 403–405 (2002).

30. M. Wojtkowski, A. Kowalczyk, R. Leitgeb, and A. F. Fercher, “Full range complex spectral optical coherence tomography technique in eye imaging”, Opt. Lett. **27**, 1415–1417 (2002).

31. D. Huang, Ph.D. dissertation, *Optical coherence tomography*, Massachusetts Institute of Technology (Cambridge, 1992).

32. H. M. Jones, R. J. Baskin, and Y. Yeh, "The molecular origin of birefringence in skeletal muscle. Contribution of myosin subfragment S-1," Biophysical Journal **60**, 1217–1228 (1991).

33. P. Whittaker and P. B. Canham, "Demonstration of quantitative fabric analysis of tendon collagen using two-dimensional polarized light microscopy," Matrix **11**, 56–62 (1991).

34. A. Boyde, P. Bianco, M. Portigliatti Barbos, and A. Ascenzi, "Collagen orientation in compact bone: I. A new method for the determination of the proportion of collagen parallel to the plane of compact bone sections," Metabolic Bone Disease & Related Research **5**, 299–307 (1984).

35. Y. E. Yarker, R. M. Aspden, and D. W. Hukins, "Birefringence of articular cartilage and the distribution on collagen fibril orientations," Connective Tissue Research **11**, 207–213 (1983).

36. R. Ortmann, "Use of polarized light for quantitative determination of the adjustment of the tangential fibres in articular cartilage," Anatomy & Embryology **148**, 109–120 (1975).

37 . B. Alberts, D. Bray, J. Lewis, M. Raff, K. Roberts, and J. D. Waltson, *Molecular Biology of the Cell*, Second Edition, (Garland Publishing, New York, 1989).

38. M. Wolman and F. H. Kasten, "Polarized light microscopy in the study of the molecular structure of collagen and reticulin," Histochemistry **85**, 41–49 (1986).

39. M. Wolman, “Polarized light microscopy as a tool of diagnostic pathology A review”, The Journal of Histochemistry and Cytochemistry **23**, 21-50 (1975).

40. J. P. Dickey, B. R. Hewlett, G. A. Dumas, and D. A. Bednar, "Measuring collagen fiber orientation: a two-dimensional quantitative macroscopic technique," Journal of Biomechanical Engineering **120**, 537–540 (1998).

41. A. Boyde, P. Bianco, M. Portigliatti Barbos, and A. Ascenzi, "Collagen orientation in compact bone: I. A new method for the determination of the proportion of collagen parallel to the plane of compact bone sections," Metabolic Bone Disease & Related Research **5**, 299–307 (1984).

42. I. S. Kovach and K. A. Athanasiou, "Small-angle HeNe laser light scatter and the compressive modulus of articular cartilage," Journal of Orthopaedic Research **15**, 437–441 (1997).

43. A. Katzer, J. V. Wening, H. U. Becker-Mannich, D. E. Lorke, and K. H. Jungbluth, "Rotator cuff rupture. Vascular supply and collagen fiber processes as pathogenetic factors (see comments)," Unfallchirurgie **23**, 52–59 (1997).

44. G. B. Andrade, F. Riet-Correa, G. S. Montes, C. N. Battlehner, and P. H. Saldiva, "Dating of fibrotic lesions by the Picrosirius-polarization method. An application using the lesions of Lechiguana (bovine focal proliferative fibrogranulomatous panniculitis)," European Journal of Histochemistry **41**, 203–209 (1997).

45. M. A. Rossi, "Patterns of myocardial fibrosis in idiopathic cardiomyopathies and chronic Chagasic cardiopathy," Canadian Journal of Cardiology **7**, 287–294 (1991).

46. S. Yamazaki, "Fibrous structure of the joint capsule in the human shoulder," Okajimas Folia Anatomica Japonica **67**, 127–139 (1990).

47. P. B. Canham, H. M. Finlay, J. G. Dixon, D. R. Boughner, and A. Chen, "Measurements from light and polarised light microscopy of human coronary arteries fixed at distending pressure," Cardiovascular Research **23**, 973–982 (1989).

48. N. Yamamoto, S. Nishioka, and Y. Sasai, "Polarization microscopic investigation of collagen and acid glycosaminoglycans in the skin of progressive systemic sclerosis (PSS)," Acta Histochemica **97**, 195–202 (1995).

49. P. B. Canham, H. M. Finlay, J. A. Kiernan, and G. G. Ferguson, "Layered structure of saccular aneurysms assessed by collagen birefringence," Neurological Research **21**, 618–626 (1999).

50. P. B. Canham, H. M. Finlay, J. G. Dixon, and S. E. Ferguson, "Layered collagen fabric of cerebral aneurysms quantitatively assessed by the universal stage and polarized light microscopy," Anatomical Record **231**, 579–592 (1991).

51 M. Wolman, “Polarized light microscopy as a tool of diagnostic pathology–review”, The Journal of Histochemistry and Cytochemistry **23**, 21-50 (1975).

52. H. M. Jones, R. J. Baskin, and Y. Yeh, "The molecular origin of birefringence in skeletal muscle. Contribution of myosin subfragment S-1," Biophysical Journal **60**, 1217–1228 (1991).

53. A. Periasamy, D. H. Burns, D. N. Holdren, G. H. Pollack, and K. Trombitas, "A-band shortening in single fibers of frog skeletal muscle," Biophysical Journal **57**, 815–828 (1990).

54. T. P. Burghardt and N. L. Thompson, "Motion of myosin cross-bridges in skeletal muscle fibers studied by time-resolved fluorescence anisotropy decay," Biochemistry **24**, 3731–3735 (1985).

55. Y. Yeh and B. G. Pinsky, "Optical polarization properties of the diffraction spectra from single fibers of skeletal muscle," Biophysical Journal **42**, 83–90 (1983).

56. P. Whittaker, T. Romano, M. D. Silver, and D. R. Boughner, "An improved method for detecting and quantifying cardiac muscle disarray in hypertrophic cardiomyopathy," American Heart Journal **118**, 341–346 (1989).

57. M. A. Rossi, "Patterns of myocardial fibrosis in idiopathic cardiomyopathies and chronic Chagasic cardiopathy," Canadian Journal of Cardiology **7**, 287–294 (1991).

58. J. S. Chen, R. J. Baskin, K. Burton, S. Shen, and Y. Yeh, "Polarization states of diffracted light. Changes accompanying fiber activation," Biophysical Journal **56**, 595–605 (1989).

59. J. Makovitzky, "Polarization optical analysis of blood cell membranes," Progress in Histochemistry & Cytochemistry **15**, 1–100 (1984).

60. R. Oldenbourg, "Polarized light microscopy of spindles," Methods in Cell Biology **61**, 175–208 (1999).

61. R. E. Stephens, "A thermodynamic analysis of mitotic spindle equilibrium at active metaphase," Journal of Cell Biology **57**, 133–147 (1973).

62. S. Inoue and R. Oldenbourg, "Microtubule dynamics in mitotic spindle displayed by polarized light microscopy," Molecular Biology of the Cell **9**, 1603–1607 (1998).

63. K. Katoh, K. Hammar, P. J. S. Smith, and R. Oldenbourg, "Birefringence imaging directly reveals architectural dynamics of filamentous actin in living growth cones," Molecular Biology of the Cell **10**, 197–210 (1999).

64. B. V. Bronk, W. P. Van de Merwe, and M. Stanley, "*In vivo* measure of average bacterial cell size from a polarized light scattering function," Cytometry **13**, 155–162 (1992).

65. W. Mickols, M. F. Maestre, I. Tinoco, Jr., and S. H. Embury, "Visualization of oriented hemoglobin S in individual erythrocytes by differential extinction of polarized light," Proceedings of the National Academy of Sciences of the United States of America **82**, 6527–6531 (1985).

66. D. A. Beach, C. Bustamante, K. S. Wells, and K. M. Foucar, "Differential polarization imaging. III. Theory confirmation. Patterns of polymerization of hemoglobin S in red blood sickle cells," Biophysical Journal **53**, 449–456 (1988).

67. D. H. Steel and A. Waldock, "Measurement of the retinal nerve fibre layer with scanning laser polarimetry in patients with previous demyelinating optic neuritis," Journal of Neurology, Neurosurgery & Psychiatry **64**, 505–509 (1998).

68. A. Waldock, M. J. Potts, J. M. Sparrow, and W. S. Karwatowski, "Clinical evaluation of scanning laser polarimetry: I. Intraoperator reproducibility and design of a blood vessel removal algorithm," British Journal of Ophthalmology **82**, 252–259 (1998).

69. A. Waldock, M. J. Potts, J. M. Sparrow, and W. S. Karwatowski, "Clinical evaluation of scanning laser polarimetry: II. Polar profile shape analysis," British Journal of Ophthalmology **82**, 260–266 (1998).

70. J. C. Patterson-Kane, D. A. Parry, H. L. Birch, A. E. Goodship, and E. C. Firth, "An age-related study of morphology and cross-link composition of collagen fibrils in the digital flexor tendons of young thoroughbred horses," Connective Tissue Research **36**, 253–260 (1997).

71. S. Thomsen, J. A. Pearce, and W. Cheong, “Changes of birefringence as markers of thermal damage in tissues”, IEEE T. on Biomed. Eng. **12**, 1174–1179 (1989).

72. F. Le Roy-Brehonnet and B. Le Jeune, “Utilization of Mueller matrix formalism to obtain optical targets depolarization and polarization properties,” Prog. Quant. Electr. **21**, 109-151 (1997).

73. J. J. Gil and E. Bernabeu, “Obtainment of the polarizing and retardation parameters of a non-depolarizing optical system from the polar decomposition of its Mueller matrix”, Optik **76**, 67-71 (1987).

74. E. Collett, Chap. 10 in *Polarized Light Fundamentals and Applications*, (Marcel Dekker, New York, 1993).

75. N. Vansteenkiste, P. Vignolo and A. Aspect, “Optical reversibility theorems for polarization: application to remote control of polarization”, J. Opt. Soc. Am. A **10**, 2240-2245 (1993).

76. G. Yao and L. V. Wang, “Monte Carlo simulation of an optical coherence tomography signal in homogenous turbid media”, Phys. Med. Biol. **44**, 2307-2320 (1999).

77. Y. Zhao, Z. Chen, C. Saxer, S. Xiang, J. F. de Boer and J. S. Nelson, “Phase-resolved optical coherence tomography and optical Doppler tomography for imaging blood flow in human skin with fast scanning speed and high velocity sensitivity”, Opt. Lett. **25**, 114-116 (2000).

78. Alexander D. Poularikas, Chap.7 in *The Transforms and Applications Handbook* (CRC Press, Boca Raton, 1996).

79. J. F. de Boer, S. M. Srinivas, A. Malekafzali, Z. Chen, and J. S. Nelson, "Imaging thermally damaged tissue by polarization sensitive optical coherence tomography", Opt. Express, **3**, 212-218 (1998). http://epubs.osa.org/oearchive/source/5895.htm.

80. R. A. Chipman, "Polarimetry", Chap. 22 in the *Handbook of Optics*, Vol. II, (McGraw-Hill, New York, 1995).

81. G. Marquez, L.-H. Wang, S.-P. Lin, J. A. Schwartz, and S. L. Thomsen, "Anisotropy in the absorption and scattering spectra of chicken breast tissue," Appl. Opt. **37**, 798–804 (1998).

82. C. Brosseau, *Fundamentals of Polarized Light: A Statistical Optics Approach*, (John Wiley & Sons, New York, 1998).

83. S. Y. Lu and R. A. Chipman, "Homogenous and inhomogenous Jones matrix," J. Opt. Soc. Am. A **11**, 766–772 (1994).

84. Y. Pan, R. Birngruber, J. Rosperich, and R. Engelhardt, "Low-coherence optical tomography in turbid tissue: theoretical analysis," Appl. Opt. **34**, 6564–6574 (1995).

85. Y. Pan, R. Birngruber, and R. Engelhardt, "Contrast limits of coherence-gated imaging in scattering media," Appl. Opt. **36**, 2979–2983 (1997).

86. S. Jiao, W. Yu, G. Stoica, and L.-H. V. Wang, "Optical-fiber-based Mueller optical coherence tomography", Opt. Lett. in press (2003).

87. J. M. Schmitt and S. H. Xiang, “Cross-polarized backscatter in optical coherence tomography of biological tissue,” Opt. Lett. **23**, 1060–1062 (1998).

88. M. I. Mishchenko and J. W. Hovenier, “Depolarization of light scattered by randomly oriented nonspherical particles,” Opt. Lett. **20**, 1356–1358 (1995).

89. C. E. Saxer, J. F. de Boer, B. H. Park, Y. Zhao, Z. Chen, and J. S. Nelson, “High-speed fiber-based polarization-sensitive optical coherence tomography of *in vivo* human skin”, *Opt. Lett*. **25**, 1355–1357 (2000).

VITA

Shuliang Jiao received his Ph.D. in electronic physics and devices from Huazhong University of Science and Technology (China) in May 1992. He later researched under Dr. Lihong V. Wang of Texas A&M University in the fall of 1999. The research focused on the development of polarization-sensitive Mueller-matrix optical coherence tomography (OCT)—a technology for the acquisition of the depth-resolved polarization properties of biological samples. He received his Ph.D. in biomedical engineering in December 2003.

C/O Shuliang Jiao
38051 Edward Ave.
Fremont, CA 94536
Tel. (510) 797-7595